Experimental and Theoretical Design and Study of Advanced Precipitation-Strengthened High-Entropy Alloys

A Dissertation Presented for the
Doctor of Philosophy
Degree
The University of Tennessee, Knoxville

Rui Feng
December 2019

Copyright © 2019 by Rui Feng
All rights reserved.

DEDICATION

The dissertation is dedicated to my beloved family, my parents, Wenjun Feng and Shufeng Cai, and my sister, Yuanyuan Feng, who are always inspiring and supporting me in their unique ways.

ACKNOWLEDGEMENTS

First and foremost, I would like to express my sincere gratitude to my supervisor, Prof. Peter. K. Liaw, for supporting me in many aspects through his immense knowledge, patience, motivation, enthusiasm, and encouragement. Under Prof. Liaw's guidance, I learn to do research and to be professional in academia. It is my great honor to have Prof. Liaw as my advisor. I would also like to thank all committee members, including Prof. Yanfei Gao, Prof. Hahn Choo, and Prof. Hairong Qi, for their insightful suggestions and encouragement.

My sincere thanks also go to Dr. Michael C. Gao from National Energy Technology Laboratory (NETL) for his always patient and constructive instructions on my research. I am grateful to Dr. Chuan Zhang and Dr. Fan Zhang at Computherm LLC for their thermodynamic calculations and valuable discussions. I also express my gratitude to Dr. Zongrui Pei from NETL for his help in Monte-Carlo simulations. I appreciate the help in first-principles calculations from Prof. Michael Widom and Mr. Bojun Feng at Carnegie Mellon University. I would like to thank Dr. Ke An, Dr. Yan Chen, and Dr. Dunji Yu from Oak Ridge National Laboratory (ORNL) for their instructions on in-situ neutron diffraction at VULCAN beamline of Spallation Neutron Source (SNS). My thanks also go to Dr. Dong Ma, Dr. Mattew G. Tucker, and Dr. Joerg C. Neuefeind at ORNL for their help and guidance in use of neutron total scattering at NOMAD, SNS. I appreciate Dr. Jonathan D. Poplawsky and Dr. Wei Guo for their help in atomic probe tomography (APT) characterizations at ORNL. I would like to thank Dr. Yang Ren at Advanced Photon Source (APS) of Argonne National Laboratory (ANL) for

his help in synchrotron experiments. I am so grateful to my great friends, Mr. Douglas E. Fielden, Mr. Larry Smith, Mr. Phil Lollar in the mechanical workshop at The University of Tennessee (UT), for the enlightening talks and their great help in machining test samples. I would like to thank Dr. John Dunlap at UT for his always kind help in use of microscopy facilities. I also thank Mr. Gregory Jones for his tutoring on the operation of scanning-electron microscope.

My thanks also go to Ms. Carla Lewrence, Ms. Gena Jenkins, Ms. Martha Gale, Ms. Tonya Brewer, Ms. Tracy Lee, Mr. Frank Holiway, Mr. Randy Stooksbury, Mr. Stephen Stiner, Mr. Adam Cain, Ms. Ms. Ashledy Cole, Ms. Tonya Goins, and Ms. Tracy Mandrekas in our department for their great help.

I would like to thank all of my student colleagues for their help and friendship. I am especially grateful to Mr. Zhinan An, Dr. Xie Xie, Dr. Haoling Jia, Dr. Zhiqian Sun, Dr. Zhi Tang, Dr. Bilin Chen, Dr. Tong Yang, Dr. Lu Huang, Dr. Gian Song, Dr. Louis J. Santodonato, Dr. Haoyan Diao, Dr. Shuying Chen, Dr. Shaoyu Wang, Mr. Chanho Lee, Mr. Peiyong Chen, Mr. Xuesong Fan, Mr. Zongyang Lyu, Ms. Di Xie, Dr. Yangyang Zhao, Dr. Yuan Li, Dr. Peijun Hou, Ms. Hui Wang, Mr. Zengquan Wang, and Dr. Jamieson Brechtl at UT. I also thank many visiting scholars in our group.

I would like to acknowledge the financial support from the National Science Foundation under grant of DMR-1611180 and the U.S. Army Research Office under project number of W911NF-13-1-0438. I also appreciate the financial support from the Shull Wollan Center Graduate Research Fellowship.

ABSTRACT

Recently, exceptional properties that are continuously found in an intriguing new class of metallic structural materials, high-entropy alloys (HEAs), demonstrate their great potential for engineering applications particularly in extreme environments where conventional alloys reach their limits. The attractive properties in HEAs are mainly attributed to HEAs exhibited special effects, such as, vast compositional space, heterogeneous local atomic environments, tunable stacking-fault energy (SFE), ductile multicomponent intermetallic precipitates, and integrated various engineering concerns. Therefore, the concept of HEAs opens up new avenues to develop advanced high-performance alloys for overcoming some drawbacks appeared in traditional alloys. In this work, two main tasks are studied for developing advanced precipitation-strengthened alloys by the HEA concept through integrated experimental and theoretical methods.

In the first task, to develop significantly cheaper and lighter high-temperature alloys than Ni-base superalloys, precipitation-strengthened body-centered-cubic (BCC) HEAs, which possess a microstructure analogous to that of the γ/γ′ Ni-base superalloys, are designed, using the CALPHAD-based high-throughput computational method (HTCM). The fundamental understanding of the phase stability, precipitation strengthening, and order-disorder transition in the newly-designed lightweight HEAs are revealed by *in-situ* neutron scattering, advanced microcopies, *ab initio* molecular dynamics (AIMD), and Monte-Carlo (MC) simulations. The insights obtained in this study offer a paradigm to develop high-performance lightweight HEAs via the high-throughput method.

In the second task, in order to develop advanced fatigue-resistant HEAs, a B2 precipitation-strengthened $Al_{0.5}CoCrFeNi$ HEA is designed, which exhibits the outperforming fatigue life at low strain amplitudes compared with traditional materials. Its real-time cyclic-deformation mechanisms are revealed by *in-situ* neutron diffraction and advanced microscopy experiments. The present work indicates that various beneficial cyclic-deformation mechanisms, such as the multicomponent-precipitation strengthening, deformation twinning, and reversible stress-induced martensitic phase transformation can be synergistically integrated into HEAs together. Guided by this design idea, fatigue-resistant precipitation-strengthened HEAs can be developed, which can be generalized to other alloys systems.

TABLE OF CONTENTS

CHAPTER I INTRODUCTION 1

1.1 Development of Advanced Precipitation-strengthened Lightweight HEAs 2

1.2 Development of Advanced Precipitation-strengthened Fatigue-resistant HEAs 4

1.3 Framework 6

CHAPTER II LITERATURE REVIEW 8

2.1 High-entropy Alloys 8

2.2 Precipitation-strengthened HEAs 9

CHAPTER III DESIGN OF LIGHTWEIGHT HIGH-ENTROPY ALLOYS 15

3.1 Introduction 15

3.2 Materials and Methods 16

3.3 Phase-formation Rules of HEAs 18

3.4 Results 25

3.4.1 Newly-designed lightweight HEAs 25

3.4.2 Criteria based on ΔH_{mix}, δr, and Ω 28

3.4.3 Criteria based on ϕ, Φ, and Φ_f 30

3.4.4 CALPHAD modeling 37

3.5 Discussions 43

3.5.1 Thermodynamic mixing properties of Al-Cr-Nb-Ti-V and Cr-Nb-Ti-V-Zr systems 43

3.5.2 Common issues of empirical rules 46

3.5.3 Perspectives of future design of lightweight HEAs 50

CHAPTER IV PHASE STABILITY AND TRANSFORMATION BEHAVIORS OF A LIGHTWEIGHT HIGH-ENTROPY ALLOY 54
4.1 Introduction 54
4.2 Materials and Methods 56
4.2.1 Sample preparation and hardness test 56
4.2.2 Microscopy, diffraction, and atom-probe tomography 57
4.2.3 CALPHAD modeling 58
4.2.4 AIMD simulation 59
4.2.5 DFT calculations at zero temperature 59
4.3 Results 60
4.3.1 Phase identification and evolution 60
4.3.2 TEM characterization 64
4.3.3 APT analysis 67
4.3.4 CALPHAD modeling 71
4.3.5 DFT calculations at zero temperature 73
4.3.6 AIMD modeling 77
4.4 Discussions 81
4.4.1 Phase stability, transformation, and precipitation behaviors of the $L2_1$ phase 81
4.4.2 Perspectives of the future design of advanced lightweight HEAs 85
CHAPTER V HIGH-THROUGHPUT DISCOVERY AND STUDY OF HIGH-PERFORMANCE PRECIPITATION-STRENGTHENED LIGHTWEIGHT HIGH-ENTROPY ALLOYS 90
5.1 Introduction 90

5.2 Materials and Methods 92
5.2.1 The CALPHAD-based HTCMs 92
5.2.2 Sample preparation, microstructural characterizations, and mechanical testing 93
5.2.3 In-situ neutron scattering experiments 95
5.2.4 Ab initio molecular dynamics (AIMD) simulations 96
5.3 Results 99
5.3.1 CALPHAD-based HTC screening results 99
5.3.2 Systematic experimental investigations on identified LWHEAs 101
5.3.3 Theoretical simulations via AIMD and MC 113
CHAPTER VI REAL-TIME INSIGHT INTO THE CYCLIC-DEFORMATION MECHANISMS OF A PRECIPITATION-STRENGTHENED HIGH-ENTROPY ALLOY 130
6.1 Introduction 130
6.2 Materials and Methods 131
6.2.1 Sample preparation 131
6.2.2 LCF experiments 132
6.2.3 Microstructural characterizations 132
6.2.4 In-situ neutron diffraction measurements 133
6.3 Results 135
6.3.1 Microstructural characterizations 135
6.3.2 Monotonic and cyclic stress responses 135
6.3.3 Fatigue life prediction 139

6.3.4 In-situ neutron diffraction during monotonic and cyclic loadings..... 140
6.4 Discussions 156
6.5 Conclusions..... 158
CHAPTER VII CONCLUSIONS..... 159
CHAPTER VIII FUTURE WORK..... 161
LIST OF REFERENCES..... 163
VITA..... 180

LIST OF TABLES

Table 3.1 Nominal chemical compositions in at.% and the estimated densities, ρ, of the newly-designed $Al_xCrFeMnTi_y$ (x = 1, 1.5, 2, 3, and 4; y = 0.25 and 1) alloys. 18

Table 3.2 The microstructures and the formation-rule parameters, for typical and lightweight HEAs reported and newly-designed HEAs..... 23

Table 3.3 The effectiveness of the phase-formation prediction for lightweight HEAs using the empirical phase-formation rules (√ and × represent successful and unsuccessful predictions, respectively). 38

Table 4.1 Average compositions (at.%) of BCC, $L2_1$ (measured by APT), and C14 Laves (measured by EDS) phases in the as-cast and annealed samples. Moreover, the equilibrium compositions of each phase calculated by CALPHAD at the temperatures of 750 °C, 850 °C, 1,000 °C, and 1,200 °C are also listed in the Table. The superscript, Exp, means that the phase is measured by APT or EDS; the superscript, Eq, suggests that the phase is predicted by CALPHAD assuming the equilibrium state. 68

Table 4.2 Calculated diffusion constants ($\times 10^{-5}$ cm^2/s) and corresponding activation energies of the liquid $Al_{1.5}CrFeMnTi$ from the present AIMD simulations. ... 80

Table 5.1 Nominal chemical compositions of the identified eight alloys. 94

Table 5.2 The nearest-neighbor interaction parameters, J_{ij} , in eV. 100

Table 5.3 APT measured chemical compositions of the BCC and $L2_1$ phases in the Alloys 1 and 8. 109

Table 6.1 Chemical compositions of the FCC matrix and B2 precipitates in the $Al_{0.5}CoCrFeNi$ HEA (in atomic percent, at.%) measured by energy-dispersive scanning (EDS). 137

Table 6.2 The fitting values of parameters shown in the strain-life equation..... 141

LIST OF FIGURES

Figure 1.1 The framework of the present integrated experimental and theoretical work. (The abbreviations shown in the framework stand for: SEM - Scanning-electron microscopy; EBSD - Backscattered-electron diffraction; XRD - X-ray diffraction; ND - Neutron diffraction; (HR) TEM - (High-resolution) Transmission-electron microscopy; APT - Atomic-probe tomography; CALPHAD - CALculation of PHAse Diagrams; AIMD - Ab initio molecular dynamics; DFT - Density functional theory; CPFEM - Crystal-Plasticity Finite-Element Modeling). 7

Figure 2.1 Exceptional strength-ductility combination achieved in the MCINPS alloys at ambient temperature. (a) Engineering stress-strain curves of the MCINPS alloys compared with the FeCoNi base alloy, showing a significant increase of strength without ductility reduction. The Al7Ti7 alloy exhibits ductile dimpled structures without macroscopic necking. (b) Yield strength versus the product of strength and ductility of the MCINPS alloys compared with those of other high-performing materials [8]. 11

Figure 3.1 XRD patterns of a series of newly-designed lightweight HEAs: (a) $Al_{1.0}CrFeMnTi_{0.25}$; (b) $Al_{2.0}CrFeMnTi_{0.25}$; (c) $Al_{3.0}CrFeMnTi_{0.25}$; (d) $Al_{4.0}CrFeMnTi_{0.25}$; (e) $Al_{1.5}CrFeMnTi$; and (f) $Al_{2.0}CrFeMnTi$. 26

Figure 3.2 SEM images of a series of newly-designed lightweight HEAs. (a) $Al_{1.0}CrFeMnTi_{0.25}$; (b) $Al_{2.0}CrFeMnTi_{0.25}$; (c) $Al_{3.0}CrFeMnTi_{0.25}$; (d)

$Al_{4.0}CrFeMnTi_{0.25}$; (e) $Al_{1.5}CrFeMnTi$; and (f) $Al_{2.0}CrFeMnTi$. (GBs represent grain boundaries) 27

Figure 3.3 Plots of (a) ΔH_{mix} and (b) Ω versus δ_r for a series of the developed classic HEAs and lightweight HEAs (each composition symbol shown in Figures 3.3-3.7 is marked with the same composition's number shown in Table 3.2)..... 29

F**igure 3.4** The variation of the single-parameter, ϕ, with respect to (a) ΔH_{mix}, (b) δ_r, and (c) Ω. 31

Figure 3.5 The variation of the thermodynamic parameter, Φ, with respect to (a) ΔH_{mix}, (b) δ_r, and (c) Ω. 33

Figure 3.6 The variation of thermodynamic parameter Φ_f with respect to (a) ΔH_{mix}, (b) δ_r, and (c) Ω. 34

Figure 3.7 Comparison plots of (a) Φ_f versus ϕ and (b) Φ_f versus Φ. 36

Figure 3.8 Predicted phase formation in (a, d) AlNbTiV; (b, e) NbTiVZr; (c, f) $AlCr_{0.5}NbTiV$; (g) AlCrNbTiV; (h) CrNbTiZr; and (i) CrNbTiVZr using the TCNI8 database. The non-equilibrium solidification for plots (d-f) are generated using the Scheil model [105]..... 40

Figure 3.9 Calculated thermodynamic mixing properties of the BCC phase at 1,000 °C: (a-c) $AlTi_x$, $AlVTi_x$, AlNbVTix, and $AlCrNbVTi_x$; (d-f) $NbAl_x$, $NbTiAl_x$, $NbTiVAl_x$, and $CrNbTiVAl_x$; (g-i) $CrTi_x$, $CrVTi_x$, $CrNbVTi_x$, and $CrNbVZrTi_x$ pseudo-binaries using the TCNI8 database. ΔS_{mix}^{BCC}, ΔH_{mix}^{BCC}, and ΔG_{mix}^{BCC} are the entropy of mixing, enthalpy of mixing, and Gibbs-free energy of mixing for the BCC solid-solution phase , respectively. The reference state

is the BCC phase at 1,000 °C. The dashed curves in (a), (d), and (g) are the ideal configurational entropies. 44

Figure 4.1 EBSD-phase mappings. (a) the as-cast state, (b) the annealed state at 750 °C for 168 h, (c) the annealed state at 850 °C for 168 h, (d) the annealed state at 1,000 °C for 504 h, and (e) the annealed state at 1,200 °C for 168 h (the red and blue regions represent the BCC + $L2_1$ and C14 phases, respectively. Meanwhile the fraction of each phase was given, and the insets are the corresponding enlarged BSE images of each state)..... 61

Figure 4.2 Diffraction patterns of the $Al_{1.5}$CrFeMnTi alloy. (a) ex-situ synchrotron X-ray diffraction patterns in the as-cast, 750 °C-annealed, and 850 °C-annealed states, and (b) In-situ neutron scattering at RT, 800, 1,000, 1,200, and 1,400 °C. 63

Figure 4.3 TEM images of the as-cast HEA. (a) bright-field image, (b) dark-field image using the common diffraction spots of $L2_1$ and BCC phases, (c) dark-field image using the diffraction spot of the C14 Laves phase, and (d) the selected area electron diffraction (SAED) pattern along $<110>_{L2_1+BCC}$ 65

Figure 4.4 TEM DF, SAED, and HRTEM micrographs of different states. (a) the as-cast specimen, (b) aged at 750 °C for 168 h, and (c) aged at 850 °C for 168 h, showing the $L2_1$ particles in the BCC matrix. 66

Figure 4.5 APT analysis of $Al_{1.5}$CrFeMnTi HEA in different processing states. (a) APT results in the as-cast state, including one box with the 18 at.% Cr isoconcentration surface showing the locations of $L2_1$ and BCC phases. The proximity histogram is constructed across the interphase between the large

FeTi-rich particle and small Cr-rich particle. (b) APT results of the annealed samples at 750 °C for 168 h, containing chemical mappings, experimental and binomial composition frequency distributions, and the LBM fit of BCC and $L2_1$ phases, respectively. The results show the inhomogeneity of Cr, Fe, Mn, and Ti. (c) APT results of the annealed samples at 850 °C for 168 h, showing the 12 at.% Ti isoconcerntration surfaces and the proximity histogram constructed across the interphase between the $L2_1$ and BCC phases. 70

Figure 4.6 Phase diagram prediction. (a) equilibrium calculation of the $Al_{1.5}CrFeMnTi$ alloy and (b) isopleth of $Al_{1.5}CrFeMnTix$. 72

Figure 4.7 The comparisons of experimentally-measured and CALPHAD-predicted compositions in the constituent phases. (a) BCC, (b) $L2_1$, and (c) C14. 74

Figure 4.8 DFT-predicted enthalpy of formation. (a) selected $L2_1$ compounds and (b) C14 compounds at zero temperature. 75

Figure 4.9 AIMD simulations. (a) selected partial PDFs of $Al_{1.5}CrFeMnTi$ at T = 1,800 °C from the present AIMD simulations (the inset shows a snapshot of the atomic structure) and (b) calculated diffusion constants for $Al_{1.5}CrFeMnTi$ from AIMD simulations as a function of inverse temperature. 78

Figure 4.10 Schematic illustration of ideal microstructure in the future design of advance lightweight HEAs based on the Al-Cr-Fe-Mn-Ti system (orange and blue represent $L2_1$ and BCC phases, respectively). 88

Figure 5.1 Screening optimal alloy compositions of the Al-Cr-Fe-Mn-Ti system based on the progressive criteria used in the present study. (a) Al-Cr projection, (b) Al-Fe projection, (c) Al-Mn projection, and (d) Al-Ti projection. 102

Figure 5.2 (a) Synchrotron XRD patterns of alloys 1-8, (b) and (c) In-situ neutron-scattering patterns of alloy 1 ($Al_{20}Cr_5Fe_{50}Mn_{20}Ti_5$) and alloy 7 ($Al_{30}Cr_5Fe_{50}Mn_{10}Ti_5$) (The label of order means that the reflections are exclusive to the $L2_1$ structure, while the label of fundamental means that the reflections are common to both the ordered $L2_1$ and disordered BCC structures), and (d-g) The microstructure of the as-cast alloy 1: (d) BSE image, and EDS mapping pertaining to (e-g) Al, Cr, Fe, Mn and Ti, respectively.. 103

Figure 5.3 BSE images of Alloys 1-8. 106

Figure 5.4 TEM characterizations of selected representative alloys. (a-f) DF images of Alloys 1 ($Al_{20}Cr_5Fe_{50}Mn_{20}Ti_5$), 2 ($Al_{25}Cr_5Fe_{50}Mn_{15}Ti_5$), 3 ($Al_{35}Cr_5Fe_{40}Mn_{10}Ti_{10}$), 4 ($Al_{30}Cr_{10}Fe_{35}Mn_{15}Ti_{10}$), 7 ($Al_{30}Cr_5Fe_{50}Mn_{10}Ti_5$), and 8 ($Al_{16}Cr_5Fe_{50}Mn_{24}Ti_5$) taken by the unique (111) reflection of $L2_1$ phase and corresponding SADPs in the [100] and [110] zone axis, respectively. 107

Figure 5.5 APT characterizations of selected representative alloys. (a-c) elemental distributions of Alloys 1, 2, and 7, respectively. 108

Figure 5.6 (a-d) GSAS Rietveld refinements on the neutron diffraction results of Alloys 1, 2, 7, and 8 at RT, respectively. During the refinements, Alloys 2 and 7 are also treated as BCC + $L2_1$ two-phase structure, and then we obtain the lattice misfits of Alloy 1 (0.192%), Alloy 2 (-0.002%), Alloy 7 (0.001%), and Alloy 8 (0.319%). The pretty small lattice misfits of Alloys 2 and 7 also indicate that

these two alloys have a single-phase $L2_1$ structure rather than two-phase BCC and $L2_1$ structures. 111

Figure 5.7 (a) Compressive stress-strain plots of Alloys 1-8 at RT, (b) and (c) Comparison of yield strength and specific yield strength as a function of temperatures between Alloys 1, 8 and other materials, respectively [116, 194-197]. 112

Figure 5.8 (a-e) AIMD simulated partial PDFs of Alloy 1 ($Al_{20}Cr_5Fe_{50}Mn_{20}Ti_5$) at T = 1,600 °C, and f simulated diffusion constants of the constituent elements at selected temperatures. 114

Figure 5.9 (a) and (b) The LRO parameters as a function of temperature in Alloys 1 ($Al_{20}Cr_5Fe_{50}Mn_{20}Ti_5$) and 7 ($Al_{30}Cr_5Fe_{50}Mn_{10}Ti_5$), respectively. (c) and (d) The SRO parameters as a function of temperature in Alloys 1 and 7, respectively. The black arrows indicate the change of the most abundant Fe as neighbor of all elements..... 117

Figure 5.10 LRO parameters of the Fe_2AlTi of $L2_1$ structure. 119

Figure 5.11 The first six SRO parameters of the Fe_2AlTi of $L2_1$ structure. Above ~2600K, all the renormalized SRO parameters approach the concentration fractions of random state. 119

Figure 5.12 (a) and (b) Pair-distribution functions (PDFs) of the Alloys 1, 2, and 7 at RT measured by neutron total scattering method. (c) and (d) lattice strain as a function of applied stress along loading direction in Alloy 1 and Alloy 7 at RT, respectively. 124

Figure 5.13 A flowchart that shows the atomic occupancies of Al, Cr, Fe, Mn, and Ti on the sublattice sites of X, Y, and Z in the $L2_1$ (X_2YZ) structure and the $L2_1$ precipitates/APD evolution rules based on the eight designed LWHEAs.. 128

Figure 6.1 LCF sample and microstructural information. (a), Sample used for LCF testing. (b) and (c), EBSD phase map and corresponding IPF image, respectively. (d) and (e), Selected area electron diffraction (SAED) patterns of FCC and B2 phases, respectively. (f), HEXRD of the $Al_{0.5}$CoCrFeNi alloy, showing the presence of FCC and B2 phases (the diffraction peaks of FCC and B2 phases are indexed as F*hkl* and B*hkl*, respectively). 136

Figure 6.2 Tensile and LCF results of the $Al_{0.5}$CoCrFeNi alloy. (a), Uniaxial tensile curve of the $Al_{0.5}$CoCrFeNi alloy at RT. (b), Cyclic-stress response (CSR) curves of the $Al_{0.5}$CoCrFeNi HEA at different strain amplitudes. (c), Hysteresis loops of the $Al_{0.5}$CoCrFeNi HEA at selected typical numbers of cycles fatigued at the strain amplitude of ± 1%. (d), Total strain amplitude, elastic strain amplitude, and plastic strain amplitude versus the number of reversals to failure ($2N_f$), displaying the presence of a bilinear Coffin-Manson relationship that signifies a variation of the cyclic-deformation modes..... 138

Figure 6.3 Real-time in-situ neutron diffraction results. (a), Lattice strain as a function of applied stress during the uniaxial tension. (b), Two-dimension (2D) contour maps of the B2-{110} d-spacing along the transverse direction, exhibiting the formation of the martensitic phase. (c), Lattice-strain evolutions of the FCC-{111} and B2-{110} at selected 1^{st}, 2^{nd}, and 5^{th} cycles along loading direction. (d), The evolution of $FWHM_G$/d versus the number of cycles at the strain

amplitudes of ± 0.5%, ± 1%, and ± 1.75%. e, The relationship of B2-[110] FWHM versus applied stress along longitudinal and transverse directions at 50^{th} cycle at the strain amplitude of ± 1.75%. (f) and (g), The real-time *in-situ* neutron diffraction peak-intensity evolution at different fatigue cycles along longitudinal and transverse directions at the strain amplitudes of ± 1.75% and ± 1%, respectively. 142

Figure 6.4 Synchrotron XRD diffraction profiles as a function of the applied tensile stress. (a), Full patterns along the transverse direction (TD), (b), B-[110] along TD during the uniaxial tension (M denotes the martensite), showing the occurrence of the martensitic transformation upon the stress beyond 650 MPa (marked by the red arrow). 146

Figure 6.5 The relationship of B2-[110] FWHM versus applied stress along the longitudinal and transverse directions at the 50th cycle under the strain amplitudes of ± 0.5% (a) and ± 1% (b). 148

Figure 6.6 TEM and SEM characterized structural evolution at different strain amplitudes. (a) and (b), (c) and (d), (e) and (f), and (g) and (h) are the TEM bright-field (BF) images at the strain amplitudes of ± 0.25%, ± 0.5%, ± 1%, and ± 0.25%, respectively, showing the structural evolution of the cyclic response of deformation features (the inset figure in Figure 6.6a is the dark-field (DF) image, showing the plastically-deformable B2 phase). (i-l) are the SEM images of the fractured samples at the strain amplitudes of ± 0.25% and ± 1.75%, exhibiting the crack-formation features at low and high strain amplitudes. 152

Figure 6.7 (a), Summary of dominated cyclic-deformation mechanisms of $Al_{0.5}CoCrFeNi$ at different strain amplitudes. (b), The comparison of Coffin-Manson fatigue data for the present alloy and other conventional alloys [232-238]. (c), A mechanistic approach to the design of fatigue-resistant high-entropy alloys based on the present study. 155

CHAPTER I

INTRODUCTION

High-entropy alloy (HEA) as a new concept has been proposed to extend the field of research in the area of alloys [1-5]. The concept of HEA has revolutionized the strategy of the traditional alloy design by using multi-principal components (≥ 5) instead of one or two key components [1-5]. HEAs have exhibits many special effects that are barely found in traditional alloys, such as vast compositional space [3-5], high configurational entropy [3, 4], heterogeneous local atomic environments [6], tunable stacking-fault energy (SFE) [7], ductile multicomponent intermetallic precipitates [8], biased sluggish diffusion [9], and integrated various engineering concerns [3, 4]. Due to these unique effects, HEAs have exhibited high strength [10, 11], good ductility [12], excellent fracture toughness [13], high fatigue resistance [14-17], great corrosion resistance [18, 19], etc. These continuously found exceptional properties in HEAs demonstrate their great potential for engineering applications particularly in extreme environments where conventional alloys reach their limits. Therefore, the HEA-design concept opens a vast unexplored compositional region for developing advanced high-performance materials, which can replace some conventional materials with the drawbacks that cannot be simply overcome by traditional alloying process. Motivated by this concern, the purpose of the present work is to experimentally and theoretically design advanced high-performance materials by the HEA concept.

1.1 Development of Advanced Precipitation-strengthened Lightweight HEAs

It is well known that material performance at elevated temperatures is pivotal in many industrial practices from material production and processing to transportation and power generation [20]. Continuously improving the performance of materials for high-temperature applications is essential for industrial companies to stay competitive since the operational efficiency of a fuel conversion system requires higher operating temperature and pressure [20]. For example, as one of the most widely studied and most sophisticated high-temperature structural materials, the Ni-base superalloys have been developed and continuously improved to meet the specific requirements of aircraft jet engines for ever greater efficiency and thrust in the past few decades [21]. However, the development and improvement of Nickel-base superalloys have been evolutionary rather than revolutionary. Their operating temperatures (T_{use}) almost approach $0.8T_m$ and reach their application limits. Moreover, the raw materials of Ni-base superalloys are expensive and heavy. All these issues pose a high and urgent demand for people to develop advanced lightweight and low-cost structural materials for high-temperature applications. Recently, HEAs have shown great chances to possess outstanding high-temperature performances even with a relatively-low density [22-25]. Therefore, a critical question becomes to rise in mind: Could we develop advanced lightweight precipitation-strengthened alloys for high-temperature and cost-effective applications? Considering the special effects exhibited in HEAs, our alloy-design strategy is to use the HEA concept to mimic the γ/γ' microstructure in Nickel-base superalloys for pursuing outstanding high-temperature

performance. At the same time, practical engineering application concerns, such as low density, low cost, corrosion and oxidation resistance, etc., are considered in the alloy design by adding targeted elements. For example, aluminum and titanium are added for lowering the density of designed alloys. The addition of reasonable content of chromium into designed alloys can be utilized for corrosion and oxidation resistance in the high-temperature service environment. Moreover, a large amount of iron is added for the cost concern. Therefore, in the first part of the dissertation (Chapters III, IV, and V), we will focus on the development of advanced lightweight precipitation-strengthened structural materials for extreme environmental applications designed by the HEA concept. Specifically, the first part of the dissertation is composed of the following chapters.

In Chapter III, phase-formation rules are assessed from empirical rules and CALPHAD (acronym of the calculation of phase diagrams) method, based on a series of literature reported lightweight HEAs (LWHEAs) and our newly-designed Al-Cr-Fe-Mn-Ti LWHEAs. Future perspectives on the design of LWHEAs are discussed in light of CALPHAD modeling and physical metallurgy principles.

In Chapter IV, an Al-Cr-Fe-Mn-Ti LWHEA with coherent $L2_1$ precipitation within the body-centered-cubic (BCC) matrix is selected for the detailed study of its phase stability and transformation behaviors, which help to build a relatively-reliable CALPHAD thermodynamic database.

In Chapter V, aided by the built CALPHAD database on the Al-Cr-Fe-Mn-Ti multi-component system, the high-throughput CALPHAD-based method is used to efficiently screen out the coherent $L2_1$ precipitates-strengthened BCC LWHEAs for high-temperature and cost-effective applications.

Therefore, the objective of the first part of the present work is to (1) study the fundamental phase stability and transformation behaviors of newly-designed precipitation strengthened LWHEAs; (2) optimize the alloy-design strategies by integrated high-throughput theoretical and experimental methods; (3) understand order-disorder-transition and deformation behaviors of the optimized LWHEAs at room and elevated temperatures with theoretical models, which are verified through focused experimental efforts; and (4) provide fundamental understandings of developing next-generation lightweight advanced structural materials with high-performance properties.

1.2 Development of Advanced Precipitation-strengthened Fatigue-resistant HEAs

It has been widely demonstrated that HEAs exhibit exceptional mechanical properties, such as, extremely high tensile strength [8, 11], excellent ductility [12, 26], combined with good corrosion [18, 19], fatigue resistance [14-16, 27], and radiation tolerance [28, 29]. Some HEAs process all of the above properties simultaneously, making them promising candidates as structural materials in contemporary industries; e.g., turbo-pumps for rocket engines and advanced gas turbines. For these long-term applications, the fatigue properties of HEAs must be examined carefully. However, to our knowledge, very limited studies have been done for HEAs on their long-term fatigue behavior. Several works on the high-cycle fatigue (HCF) have been reported [14, 15, 27, 30], but very limited works have been published on the low-cycle fatigue (LCF) behavior of HEAs [31, 32]. HCF covers the accumulated damage caused by low-amplitude high-frequency elastic strains, while LCF characterizes the materials degradation subjected to plastic strains,

which is critical for the assessment of engineering components with stress-concentrated regions, such as the "dovetail" or "fir tree" for turbine blades. These regions will raise the local stress level, leading to plastic deformation, and will fail in only several hundreds and thousands cycles. Therefore, for the practical applications of HEAs in the future, it is of great significance to investigate the fundamental LCF behavior of HEAs. More recently, it has been reported that multicomponent intermetallic precipitates in HEAs can be plastically deformable [8, 33], which can bring out remarkable precipitation strengthening, and meanwhile, without much loss of ductility due to the load redistribution and strain partitioning between precipitates and matrix followed by co-deformation. Therefore, in the second part of the present work, multicomponent intermetallic precipitates will be introduced into the FCC matrix for improving fatigue performance. At the same time, corresponding cyclic responses and roles of the multicomponent precipitates and matrix will be probed using the advanced real-time in-situ neutron diffraction and electron microscopy methods. Ultimately, insightful alloy-design strategies for developing advanced fatigue-resistant precipitation-strengthened structural HEAs can be provided.

Thus, the goal of the second part of this work is to (1) design a precipitation-strengthened HEA for LCF study; (2) conduct a fundamental study of the LCF behavior of this HEA; (3) clarify the cyclic deformation mechanism of HEAs during LCF using state-of-the-art characterization methods, e.g., advanced microscopy and in-situ neutron diffraction; and (4) based on the fundamental understanding of deformation characteristics obtained from the present work, design and develop innovative HEAs with excellent LCF properties.

1.3 Framework

To efficiently realize the goals in both parts, a systematic research plan that integrates experimental and theoretical efforts is proposed, as shown in the framework of Figure 1.1. The present research mainly focuses on the design and study of advanced precipitation-strengthened HEAs from four aspects, including (1) Task I: Alloy design and processing to design targeted precipitation-strengthened HEAs based on the thermodynamic predictions; (2) Task II: Microstructural Characterizations to experimentally investigate the microstructure, transformation, deformation, and fracture failure behaviors; (3) Task III: Deformation Mechanisms to reveal the underlying fundamental deformation behaviors of the studied precipitation-strengthened HEAs; and (4) Task IV: Theoretical Modeling to establish a basic understanding of the phase stability, phase transformation, and deformation mechanisms of the studied precipitation-strengthened HEAs.

In summary, the overall goal of the present work is to (1) promote the development of advanced precipitation-strengthened lightweight HEAs for high-temperature and cost-effective applications, and (2) stimulate the basic research on the fatigue behavior of HEAs, and contribute to the fundamental understanding of LCF deformation behavior in precipitation-strengthened HEAs, and, consequently, further optimize the fatigue-resistant HEAs. Ultimately, the real engineering applications of HEAs can be accelerated based on the proposed research.

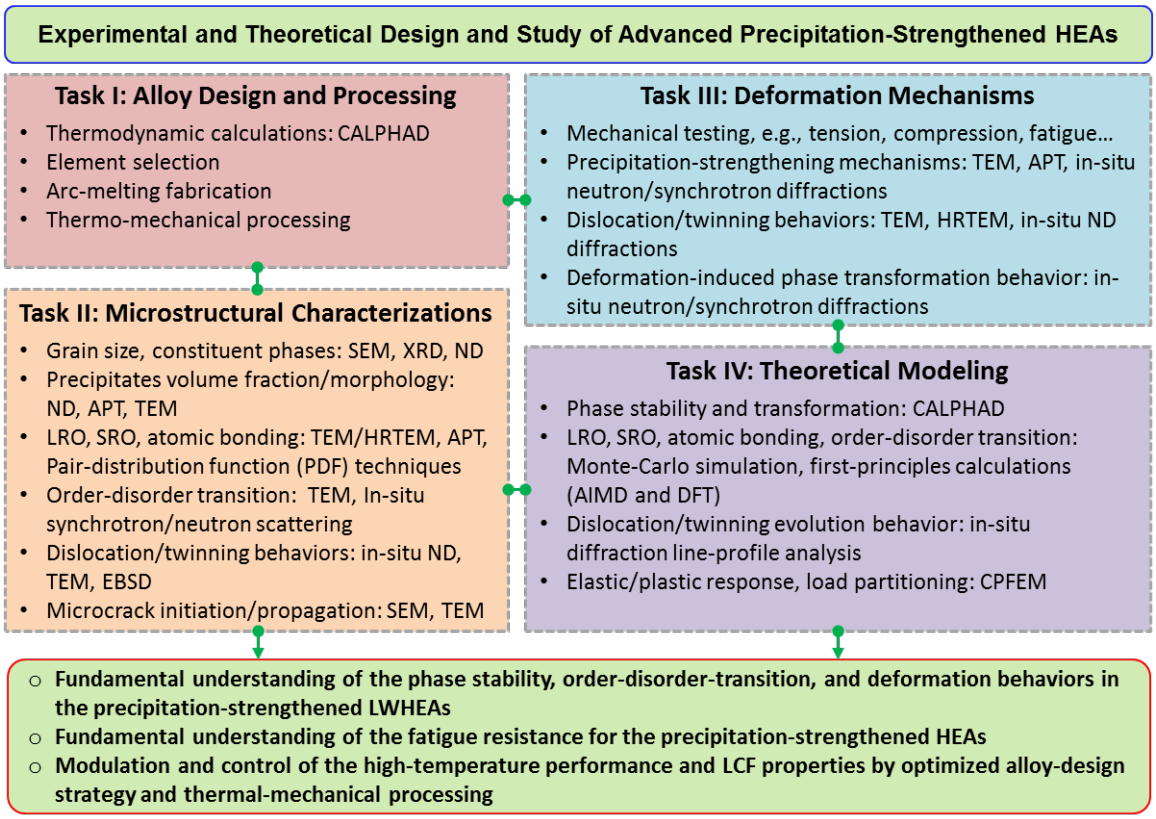


Figure 1.1 The framework of the present integrated experimental and theoretical work. (The abbreviations shown in the framework stand for: SEM - Scanning-electron microscopy; EBSD - Backscattered-electron diffraction; XRD - X-ray diffraction; ND - Neutron diffraction; (HR) TEM - (High-resolution) Transmission-electron microscopy; APT - Atomic-probe tomography; CALPHAD - CALculation of PHAse Diagrams; AIMD - Ab initio molecular dynamics; DFT - Density functional theory; CPFEM - Crystal-Plasticity Finite-Element Modeling).

CHAPTER II

LITERATURE REVIEW

2.1 High-entropy Alloys

Over the past fifteen years, a newly-emerging intriguing alloy system, called high-entropy alloys (HEAs), has experienced a huge development because of their increasingly found exceptional properties compared with traditional alloys [1-4, 34, 35], such as the outstanding high-temperature strength [10], good thermal stability [36], enhanced fatigue and fracture resistance [14, 15], great wear and corrosion resistance [37, 38], high strength-to-weight ratio [22, 25], improved radiation resistance [28, 29, 39], etc. Unlike the conventional alloys with a one and barely two principal elements, HEAs are composed of five or more principal elements, and each principal element usually lies in the range of 5 ~ 35 at.% (atomic percent) [2]. Although containing multi-principal elements, HEAs can form simple face-centered cubic (FCC), body-centered cubic (BCC), or hexagonal close-packed (HCP) solid-solution phases. The formation of simple solid-solution phases can be attributed to the increasing configurational entropy in HEAs, which makes it is possible to have lower Gibbs free energies of solid-solution phases than those of intermetallic phases [3, 4].

By mixing together multiple principal elements in high concentrations, HEAs possess some unique effects that are barely found in traditional alloys. The most famous effects are HEAs' four 'core effects', including the high entropy effect, the lattice distortion effect, sluggish diffusion, and the 'cocktail' effect [40]. The high-entropy effect

is the signature effect of HEAs, proposing that multi-principal elements (≥ 5) lead to an increase of configurational entropy, which may favor solid-solution phases over competing intermetallic compounds. The lattice distortion effect stems from the different atom sizes that lead to the crystal lattices distorted from the perfect lattices. The severely distorted lattice in HEAs may interact with dislocation motions, which could have significant impacts on mechanical properties [41, 42]. The sluggish diffusion effect is proposed in HEAs because the heterogeneous lattice environments could lead to the difficulty in substitutional diffusion and high diffusional activation energies [9]. It is worth noting that whether the sluggish diffusion is a substantial HEA effect is still under debate recently, because sluggish diffusion in some HEAs is indeed not obvious [4, 9, 43, 44]. The cocktail effect in HEAs is proposed since exceptional materials properties could be found due to unexpected synergies. Besides the four core effects, other notable effects are also found in HEAs, such as the vast compositional space [3-5], tunable stacking-fault energy (SFE) [7], ductile multicomponent intermetallic precipitates [8], concentration waves [6], and integrated various engineering concerns [3, 4]. All these effects in HEAs could be controllably utilized for developing high-performance materials.

2.2 Precipitation-strengthened HEAs

Although the initial motivation for HEAs was to avoid the intermetallic phases because of their brittle features, the intermetallic phases are not always the detrimental factor. If a proper design strategy can rationally control the structure, morphology, size, and volume ratio of an intermetallic phase, the difficulty of balancing the strength and ductility could be conquered. In fact, the role of intermetallic phases in optimizing the

strength-ductility combination has been extensively found in the conventional alloys. The pearlite structure in steels is a good paradigm, in which the alternating layers of soft ferrite and hard cementite (Fe_3C) joint together. This unique arrangement of ferrite and cementite layers offers the steels an outstanding strength-ductility combination. Another example is the Ni-based superalloys, in which the cuboidal ordered FCC γ′ phase (Ni_3Al) coherently precipitates in the FCC γ matrix [21]. The coherent two-phase microstructure renders the Ni-base superalloys have exceptional creep resistance. In fact, most reported HEAs are composed of multiphase structures rather than the expected single-phase solid solutions. The main reason is that the Gibbs free energies of solid solutions (ΔG_{SS}) cannot compete with the Gibbs free energies of intermetallic phases (ΔG_{IM}) over the entire composition ranges, structural scales, and temperatures in many HEA systems [4, 45]. From this standpoint, many works have already started to introduce beneficial secondary phases into HEAs to enhance their mechanical properties. For example, the eutectic alloy concept has been considered to design the composite structure. Y.P. Lu et al [46-48] designed eutectic HEAs (EHEAs) with a mixture of soft FCC and hard BCC phases, and an enhanced balance of fracture strength and ductility was obtained. In order to mimic the γ/γ′ microstructure in Ni-base superalloys, J.Y. He et al [46] induced the coherent nano-size $L1_2$ precipitates via the minor alloy addition of Ti and Al, which drastically increased the strength of the single-phase FCC-CoCrFeNi HEA. More recently, T. Yang et al. [8] used the HEA-design concept successfully break the strength and ductility trade-off by controllably introducing high-density ductile multicomponent intermetallic nanoparticles (MCINPs) in complex alloy systems (Figure 2.1). It demonstrates that precipitation hardening has become an effective way to improve the strength of HEAs without losing

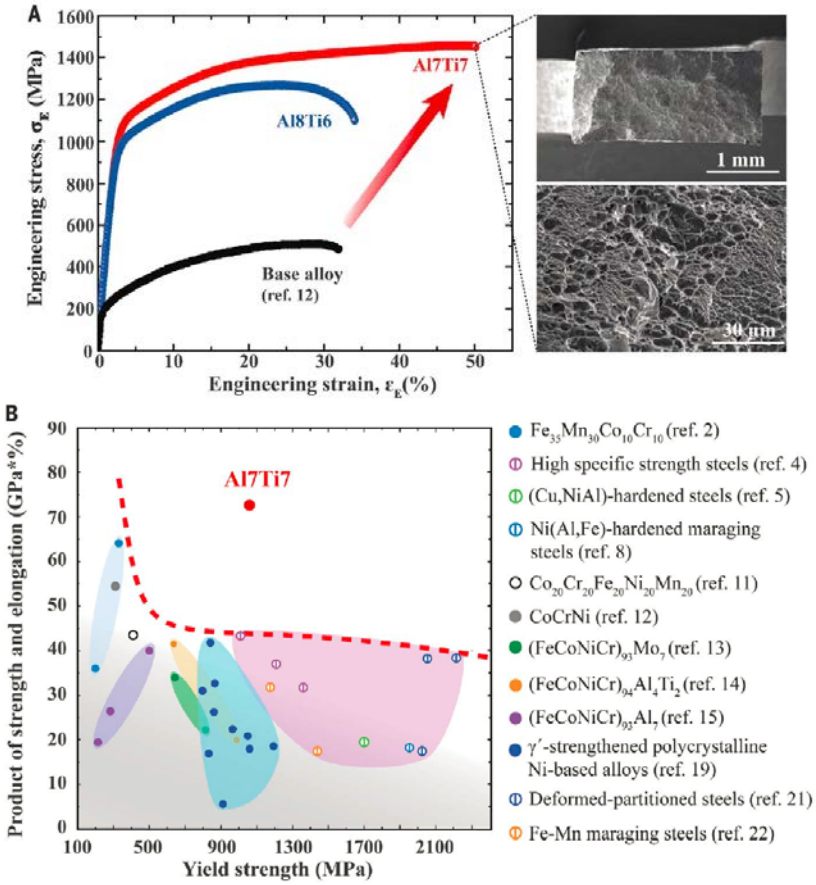


Figure 2.1 Exceptional strength-ductility combination achieved in the MCINPS alloys at ambient temperature. (a) Engineering stress-strain curves of the MCINPS alloys compared with the FeCoNi base alloy, showing a significant increase of strength without ductility reduction. The Al7Ti7 alloy exhibits ductile dimpled structures without macroscopic necking. (b) Yield strength versus the product of strength and ductility of the MCINPS alloys compared with those of other high-performing materials [8].

much plasticity [46-48]. Above all, HEA-design strategy for developing precipitation-strengthened materials can be utilized to improve performance unattainable by the pure single-phase HEAs.

It is well known that precipitation hardening is a very effective way to improve the strengths of materials without apparently sacrificing ductilities, such as the cases in γ′-$L1_2$ strengthened Ni-based and Co-based superalloys [21, 49]. As such, coherent or incoherent precipitates have been extensively applied to HEAs to enhance their strengths, especially for those alloys with low strengths or targeting outstanding high-temperature performance [50-54]. Generally, for coherent precipitates, they have a similar crystal structure and a lattice parameter to the parent matrix so that the total free energy contributing from the coherency elastic-strain energy and the interfacial energy be minimized [55]. The interplay between elastic-strain energy and interfacial energy determines the equilibrium shape of the precipitates. The common shapes of coherent precipitates observed in HEAs are uniformly distributed spherical and cuboidal. Spherical coherent precipitates are mostly found in the HEAs with γ′-$L1_2$/γ-FCC microstructures. For instance, nanosized spherical coherent precipitates, i.e., $L1_2$-Ni_3(TiAl), are formed in the soft FCC-FeCoNiCr HEA via the minor additions of Ti and Al [50, 56].

The formation of spherical shape is ascribed to negligible lattice misfit δ between the precipitates and the matrix phases [57, 58]. δ is expressed by the following equation:

$$\delta = 2 \times \frac{a_\beta - a_\alpha}{a_\beta + a_\alpha} \tag{2.1}$$

where a_α and a_β are the lattice parameters of α matrix and β precipitate, respectively.

As a result, the interfacial energy will play a dominated role in determining the equilibrium shape of precipitates. At a fixed volume, the spherical shape has the minimum interfacial energy, compared with other shapes. Thus, with the favorable total free energy, spherical precipitates are commonly formed in the systems with near-zero lattice misfit [21, 55].

Cuboidal coherent precipitates are generally found in the BCC-type HEAs with B2/BCC or $L2_1$/BCC microstructures [51-53, 59, 60]. Wang et al. reported the formation of cuboidal B2 nanoprecipitates in $Al_{0.7}CoCrFe_2Ni$ HEA, which are coherently distributed in the BCC matrix [51]. Except for cuboidal ordered phase formed in disordered matrix, Senkov et al. also found that coherent BCC nanoscale precipitates are present in the ordered B2 matrix [53].

The formation of cuboidal shape is the result of increasing lattice misfit and different elastic stiffness between precipitates and matrix phases, leading to the dominant role from elastic-strain energy in determining the morphologies of precipitates. Due to the dominant elastic-strain energy, the precipitates shape tends to take a form that can accommodate the increasing elastic strain. Therefore, a cuboidal shape with elastic stiffness anisotropy will be formed in this case. Moreover, the formed cuboidal precipitates mostly align unique crystallographic orientations in the matrix, such as $\langle 100 \rangle$ directions, a soft direction in most cubic metals [55].

As the lattice misfit increases to an extent that the elastic strain energy is too high to be burdened by the materials system, the interfaces between precipitates and matrix tend to become incoherent so that the elastic strain energy can be released [55].

Precipitates with incoherent interfaces will have higher interfacial energy but the coherency strain energy will be absent [55]. When two phases have completely different crystal structures, it is unlikely that any coherent or semicoherent interfaces form between the interfaces between the precipitates and the matrix, that is, the precipitate is said to be incoherent [55]. For example, the precipitated needle-like NiAl-rich B2 phase within the FCC matrix in an $Al_{0.3}$CoCrFeNi HEA after aging treatment at intermediate temperatures displays the incoherent interfaces with the matrix [61].

In a word, the morphology of the coherent and incoherent precipitates appeared in HEAs strongly depends on the interplay of elastic and interfacial energies and the structures of the precipitates and the matrix, similar to the situations in conventional alloys.

As known, the precipitation strengthening can be divided into two categories, particle shearing or Orowan bowing. For the coherent precipitation, possible strengthening effects could be produced from coherency strengthening, modulus mismatch strengthening, and order strengthening when dislocation cut through the nanoscaled precipitates [62]. On the other hand, when the precipitate size is large enough, the dislocation shearing becomes difficult, so that dislocation bypass mechanism, i.e, Orowano bowing mechanism, will play a key role in contributing to the strengthening. The detailed coherent precipitation strengthening mechanism will be discussed in CHAPTER V.

CHAPTER III

DESIGN OF LIGHTWEIGHT HIGH-ENTROPY ALLOYS

3.1 Introduction

Due to the demand from transportation and defense industries, the development of a new generation of lightweight alloys has also brought widespread interest in HEAs to the materials science and engineering communities, expressly, for the purpose of saving energy and raw materials [24, 25, 63-69]. The trial-and-error approach that has been used for the traditional alloys design is costly and time-consuming for the discovery of new HEAs because of the vast compositional space that they occupy. As a consequence, efforts have been made to study HEA phase-formation rules to accelerate the discovery process [35, 70-83]. Taking advantage of the phase-formation rules, the constitutive phases in HEAs can be controlled and adjusted to improve mechanical properties. In recently-developed lightweight HEAs (the densities of lightweight HEAs are defined as less than 7.00 $g \cdot cm^{-3}$ here, considering that most HEAs studied in the literature have densities more than 7.00 $g \cdot cm^{-3}$). A majority of them are composed of solid solutions (SS) and intermetallics (IM), with only a few compositions forming single-phase solid solutions [24, 25, 64, 67, 69]. Most of the lightweight HEAs contain Al and/or Ti in high concentrations in order to lower the density. However, Al (and Ti) tends to form very stable intermetallic compounds with (late) transition-metal elements (TMs) due to the apparent differences in atomic radii and electronegativity. Although Li- and Mg-containing HEAs are reported [84-86], their microstructures show a mixture of various intermetallic compounds.

In order to explore advanced lightweight HEAs, it is essential to adjust the alloy composition, and, thus, the resulting constitutive phases in the microstructure in order to achieve the desired physical and mechanical properties, while keeping the density as low as possible. Therefore, it is important to investigate these empirical phase-formation rules, as applied to lightweight HEAs. Meanwhile, the CALPHAD (the acronym of the calculation of phase diagrams) method has been used here to compare the effectiveness of predicting the single-phase solid solutions versus the empirical parameters.

In this regard, many developed formation rules have been summarized and discussed section. The corresponding parameters are also calculated, using these rules, by applying them to a series of developed HEAs and our newly-designed lightweight HEAs, aiming to provide more available experimental data for the assessment of the phase-formation rules in this study. Moreover, the CALPHAD modeling is performed for several equimolar lightweight HEAs. Combined with the experimental results, the phase-prediction effectiveness of the phase-formation rules and CALPHAD method for lightweight HEAs are studied as a way to accelerate the design of new lightweight HEAs with targeted properties.

3.2 Materials and Methods

Several new lightweight HEAs, containing five elements: Al, Cr, Fe, Mn and Ti have been designed. To examine the compositional effect on the density and phase formation, the Al molar ratio is allowed to vary from 1 to 4. To minimize the formation of detrimental intermetallic compounds, the Ti molar ratio is kept at 1 or 0.25. Strictly speaking, $Al_2CrFeMnTi_{0.25}$, $Al_3CrFeMnTi_{0.25}$, and $Al_4CrFeMnTi_{0.25}$ alloys do not meet the

HEA definition [HEAs consist of 5 or more elements between 5 and 35 atomic percent (at.%).] proposed by Yeh et al. [2]. They were designed to explore the lower-density compositional space. In consideration of the possible high-temperature applications, these newly-developed alloys contain Al and Cr in large amounts. The addition of Al (or Cr) holds the potential to form a protective dense surface scale of Al_2O_3 (or Cr_2O_3).

The $Al_xCrFeMnTi_y$ alloys (where the x and y values are in molar ratios: x = 1, 1.5, 2, 3, and 4; and y = 0.25 and 1, respectively) were prepared by arc-melting the constituent elements (element purity > 99.9 weight percentage). To achieve a homogeneous distribution of elements in the alloy, the melting and solidification processes were repeated five times.

The chemical composition and estimated density, ρ, of the alloys are listed in Table 3.1. Note that the densities of these alloys were estimated, using a rule of mixtures assumption, based on a disordered solid solution, as given by:

$$\rho = \frac{\sum c_i A_i}{\sum \frac{c_i A_i}{\rho_i}} \tag{3.1}$$

where c_i, A_i, and ρ_i are the atomic percentage, atomic weight, and density of the ith constituent element.

The alloys studied here are in the as-cast state. The crystal structures were identified on the well-polished bulk samples by X-ray diffraction (XRD, Bruker, Billerica, MA, USA), using a Bruker diffractometer with Cu Kα radiation. The microstructures were characterized, by scanning-electron microscopy (SEM, Carl Zeiss, Oberkochen, Germany),

Table 3.1 Nominal chemical compositions in at.% and the estimated densities, ρ, of the newly-designed $Al_xCrFeMnTi_y$ (x = 1, 1.5, 2, 3, and 4; y = 0.25 and 1) alloys.

Alloy	Al	Cr	Fe	Mn	Ti	ρ ($g \cdot cm^{-3}$)
$Al_{1.5}CrFeMnTi$	27.28	18.18	18.18	18.18	18.18	5.31
$Al_2CrFeMnTi$	33.32	16.67	16.67	16.67	16.67	5.06
$AlCrFeMnTi_{0.25}$	23.53	23.53	23.53	23.53	5.88	5.87
$Al_2CrFeMnTi_{0.25}$	38.10	19.05	19.05	19.05	4.75	5.16
$Al_3CrFeMnTi_{0.25}$	48.00	16.00	16.00	16.00	4.00	4.71
$Al_4CrFeMnTi_{0.25}$	55.17	13.79	13.79	13.79	3.46	4.40

using a LEO Gemini 1525 field-emission scanning-electron microscope equipped with the backscattering-electron (BSE, K. E. Developments Ltd., Cambridge, UK) detector and the energy-dispersive X-ray spectrometry (EDX, Oxford Instruments, Abingdon, UK).

3.3 Phase-formation Rules of HEAs

In order to predict the formation of solid solutions in HEAs, many phenomenological parameters based on thermodynamics and physics have been proposed [3, 34, 35, 70, 71, 73, 87]. In this study, several classic models were selected, and their main features are summarized as follows:

Based on thermodynamics and Hume-Rothery rules, Zhang et al. [3, 35, 70] put forward three parameters to suggest a criterion for the formation of a solid solution: the atomic-radius difference (δ_r), enthalpy of mixing (ΔH_{mix}), and entropy of mixing (ΔS_{mix}). They are defined by Eqs. (3.2-3.4), respectively:

$$\delta_r = \sqrt{\sum_{i=1}^{n} c_i (1 - r_i/\overline{r})^2} \tag{3.2}$$

where $\overline{r} = \sum_{i=1}^{n} c_i r_i$, c_i and r_i are the atomic percentage and radius of the ith element,

respectively; and

$$\Delta H_{\text{mix}} = \sum_{i=1, i\neq j}^{n} \Omega_{ij} c_i c_j \tag{3.3}$$

where, $\Omega_{ij} = 4\Delta H_{ij}^{\text{mix}}$, ΔH_{mix} is the enthalpy of mixing between the *i*th and *j*th elements at the equi-molar composition in the liquid, using the Miedema model; and

$$\Delta S_{\text{mix}} = -R\sum_{i=1}^{n}(c_i \ln c_i) \tag{3.4}$$

where R is the gas constant. Note that the configurational entropy of an alloy usually decreases, as the temperature decreases since lowering the temperature promotes developing atomic ordering or separation for the alloy. As a result, the true S_{conf} is temperature dependent, and its temperature dependence can be calculated from hybrid Monte Carlo/molecular dynamics (MC/MD) simulations [88]. Other entropy contributions to solid solutions or intermetallics phases may include the phonon vibration, magnetism, and electron excitation, which can be calculated from the first-principles density functional theory (DFT) modeling [89, 90].

To further present the balance between the entropy of mixing and the enthalpy of mixing, another parameter, Ω, was also proposed [70, 83], as expressed below:

$$\Omega = \frac{T_{\text{m}} \Delta S_{\text{mix}}}{\left|\Delta H_{\text{mix}}\right|} \tag{3.5}$$

where $T_{\text{m}} = \sum_{i=1}^{n} c_i (T_{\text{m}})_i$, $(T_{\text{m}})_{\text{i}}$ stands for the melting point of the *i*th element.

Based on the existing data for HEAs, the empirical criteria for forming disordered solid solutions in as-cast HEAs were suggested to be -15 kJ·mol^{-1} $< \Delta H_{\mathrm{mix}} <$ 5 kJ·mol^{-1} and $0\% < \delta_{\mathrm{r}} < 5\%$, or $\Omega \geq 1.1$ and $\delta_{\mathrm{r}} < 6.6\%$.

Recently, for the design of single-phase HEAs, Ye et al. [73] proposed a single thermodynamic parameter, ϕ, taking into account the enthalpy of mixing and the excess entropy of mixing, which results from the dense atomic packing and atomic-size misfit. The single-parameter, ϕ, can be expressed as:

$$\phi = \frac{S_C - S_H}{|S_E|} \tag{3.6}$$

where $S_{\mathrm{c}} = \Delta S_{\mathrm{mix}}$, and $S_H = \frac{|\Delta H_{\mathrm{mix}}|}{T_{\mathrm{m}}}$. S_E denotes the excess entropy of mixing, which is a function of the atomic packing and atomic size. As reported, a HEA tends to form a single-phase solid solution when $\phi \geq \phi_c$ (ϕ_c is the critical value of ϕ that separates the single-phase solid solution from the multi-phase structures). Otherwise, a multi-phase structure develops when $\phi \leq \phi_c$. Moreover, the ϕ_c is identified to be around 20 according to the investigation of Ye et al. [73].

In fact, the formation of the solid-solution phase or intermetallic phase depends on the competition of the Gibbs-free energies between solid solutions and intermetallics. In this regard, King et al. [74] proposed a new parameter, Φ, to describe the competition of the Gibbs-free energies between these two phases:

$$\Phi = \left| \frac{\Delta H_{\mathrm{mix}}^{ss} - T_{\mathrm{m}} \Delta S_{\mathrm{mix}}}{\Delta H_f^{Mid}} \right| \tag{3.7}$$

where $\Delta H_{\text{mix}}^{ss} - T\Delta S_{\text{mix}}$ is the change in the Gibbs-free energy for the formation of a fully-disordered solid solution, resulting from a mixture of its individual elements. ΔH_f^{Mid} is the enthalpy of formation of a most stable "hypothetical" intermetallic compound among all the constituent binaries from the constituents of the mixture, while ignoring their entropy since the configurational entropy of intermetallic compounds is usually low or zero [74] and other entropy sources may cancel out between compounds and solid-solution phases [74].

The details to calculate the $\Delta H_{\text{mix}}^{ss}$ and ΔH_f^{Mid} values using the Miedema's model are described in Reference [74], following the approach published in Reference [91]. It should be noted that in general, the calculated $\Delta H_{\text{mix}}^{ss}$ and ΔH_f^{Mid} values, using the Miedema model, have relatively large errors. Therefore, King et al. claimed that when Φ is larger than 1, the solid-solution phase will form at the system's melting temperature. The Φ parameters for all the compositions listed in Table 3.2 were calculated according to Eq. (3.7) via the single-phase high-entropy alloys (SPHEAs) program [92].

Another similar criterion based on enthalpy considerations was proposed by Troparevsky et al. [72]. They used the enthalpy of formation of binary compounds that are predicted, employing DFT calculations in the literature. Based on the calculated enthalpy matrix, it was claimed that a single-phase solid solution would form if the enthalpies of formation of all possible binary compounds fall within a specified range. This range requires binary compounds to be neither too stable, leading to the precipitation of that compound, nor unstable, indicating the immiscibility of the constituent elements. Using

the enthalpy of the formation matrix provided in Reference [72], a parameter, Φ_f (similar to Φ), is calculated, which is expressed as follows.

$$\Phi_f = \frac{T_{\text{ann}} \Delta S_{\text{mix}}}{\left| \Delta H_f^{\text{DFT}} \right|} \tag{3.8}$$

Here, T_{ann} is the annealing temperature used to achieve the corresponding equilibrium state in the experiments, and an appropriate value is suggested to be $T_{\text{ann}} = 0.55T_{\text{m}}$ in the work of Troparevsky et al. [72]. Values in the enthalpy of the formation matrix in Ref. [72] were used for ΔH_f to calculate Φ_f. This model ignores the enthalpy of solid-solution phases and the entropy of intermetallic compounds.

Utilizing these developed phase-formation rules mentioned above, the entirety of the corresponding empirical parameters was calculated, based on existing and newly-designed lightweight HEAs (density < 7.00 g·cm^{-3}). In addition, several classic HEAs are selected to compare with the lightweight HEAs. These parameters are listed in Table 3.2. For a comprehensive list of single-phase HEAs in face-centered cubic (FCC) [1, 3, 34], body-centered cubic (BCC) [3, 34, 93], or hexagonal close-packed (HCP) [3, 25, 34, 94-96] structures that are experimentally verified or computationally predicted, the reader is referred to a recent publication [80]. It should be noted that the listed alloys in Table 3.2 were in the as-cast state, except for $Al_{20}Li_{20}Mg_{10}Sc_{20}Ti_{30}$ and AlFeMgTiZn, which were produced by mechanical alloying.

Table 3.2 The microstructures and the formation-rule parameters, for typical and lightweight HEAs reported and newly-designed HEAs.

Number	Alloys	Density* ($g \cdot cm^{-3}$)	Structure	δ_r (%)	ΔH_{mix} ($kJ \cdot mol^{-1}$)	ΔS_{mix} ($kJ \cdot mol^{-1}$)	T_m (℃)	Ω	φ	Φ	Φ_f	Refs.
1	$Al_{1.5}CrFeMnTi$	5.31	BCC + $L2_1$ + Laves	6.41	−17.98	13.25	1,336.31	1.19	1.63	0.31	0.28	Current work
2	$Al_2CrFeMnTi$	5.06	BCC + $L2_1$ + Laves	6.33	−19.00	12.98	1,279.99	1.06	0.59	0.34	0.27	Current work
3	$AlCrFeMnTi_{0.25}$	5.87	BCC + $L2_1$	5.78	−12.07	12.71	1,357.29	1.72	4.61	0.37	0.28	Current work
4	$Al_2CrFeMnTi_{0.25}$	5.16	BCC + $L2_1$	6.07	−14.80	12.14	1,224.56	1.23	1.93	0.42	0.24	Current work
5	$Al_3CrFeMnTi_{0.25}$	4.71	BCC + $L2_1$ + Laves	6.02	−16.04	11.53	1,142.71	1.02	0.16	0.46	0.25	Current work
6	$Al_4CrFeMnTi_{0.25}$	4.40	BCC + $L2_1$ + Laves	5.86	−15.71	10.73	1,077.10	0.92	−0.92	0.48	0.22	Current work
7	$AlCr_{0.5}NbTiV$	5.71	BCC	4.55	−15.41	13.15	1,704.22	1.69	6.94	0.31	0.35	[24]
8	AlCrNbTiV	5.82	BCC + Laves	5.19	−14.56	13.38	1,724.49	1.84	6.18	0.31	0.36	[24]
9	$AlCr_{1.5}NbTiV$	5.90	BCC + Laves	5.55	−13.75	13.25	1,741.09	1.94	5.72	0.30	0.36	[24]
10	AlFeMgTiZn	4.34	BCC + IM	6.04	−6.44	13.38	987.23	2.62	4.44	1.66×10^{-2}	0.18	[84]
11	AlLiMgZnSn	4.23	FCC + IM	5.33	−6.08	13.38	428.58	1.54	4.72	8.39×10^{-3}	0.10	[85]
12	$AlLi_{0.5}MgZn_{0.5}Sn_{0.2}$	3.22	FCC+ IM	5.66	−3.89	12.31	517.83	2.50	7.93	8.73×10^{-3}	0.11	[85]
13	$AlLi_{0.5}MgZn_{0.5}Cu_{0.2}$	3.73	FCC + IM	6.72	−3.30	12.31	571.13	3.15	7.04	1.25×10^{-2}	0.11	[85]
14	$AlLi_{0.5}MgCu_{0.5}Sn_{0.2}$	3.69	FCC + IM	7.60	−3.65	12.31	621.76	3.02	4.99	1.29×10^{-2}	0.12	[85]
15	$Al_{80}Li_5Mg_5Zn_5Sn_5$	3.05	FCC + IM	3.61	−0.53	6.47	602.50	10.68	12.58	4.66×10^{-3}	0.06	[85]
16	$Al_{80}Li_5Mg_5Zn_5Cu_5$	3.08	FCC + IM	4.10	−0.61	6.47	645.13	9.73	12.07	4.92×10^{-3}	0.07	[85]
17	$Al_{20}Li_{20}Mg_{10}Sc_{20}Ti_{30}$	2.67	FCC	5.30	−0.40	12.95	1,041.83	42.56	16.17	6.27×10^{-4}	0.22	[25]
18	$AlNb_{1.5}Ta_{0.5}Ti_{1.5}Zr_{0.5}$	6.88	BCC	3.07	−15.12	12.51	1,862.79	1.77	14.71	0.27	0.28	[69]

Table 3.2 Continued The microstructures and the formation-rule parameters, for typical and lightweight HEAs reported and newly-designed HEAs.

Number	Alloys	Density* ($g \cdot cm^{-3}$)	Structure	δ_r (%)	ΔH_{mix} ($kJ \cdot mol^{-1}$)	ΔS_{mix} ($kJ \cdot mol^{-1}$)	T_m (℃)	Ω	φ	Φ	Φ_f	Refs.
19	AlNbTiV	5.59	BCC	3.30	−16.25	11.53	1,678.87	1.38	7.22	0.30	0.30	[64]
21	AlNbTiVZr	5.79	BCC + Laves + Zr_2Al	5.53	−17.44	13.38	1,714.09	1.52	3.91	0.23	0.28	[65]
22	$Al_{1.5}$NbTiVZr	5.55	BCC + Laves + Zr_2Al	5.32	−21.55	13.25	1,618.31	1.16	1.71	0.25	0.27	[65]
23	CrNbTiZr	6.67	BCC + Laves	7.84	−5.00	11.53	1,976.75	5.19	4.31	0.66	0.40	[67]
24	CrNbTiVZr	6.57	BCC + Laves	7.67	−4.64	13.38	1,963.40	6.45	5.24	0.79	0.46	[67]
25	NbMoCrTiAl	6.57	BCC + IM	4.87	−13.60	13.38	1,867.09	2.11	8.32	0.32	0.38	[68]
26	NbTiVZr	6.52	BCC	6.03	−0.25	11.53	1,977.50	103.76	7.97	1.86	2.64	[67]
27	$NbTiV_2Zr$	6.34	3 BCCs	6.41	−1.28	11.08	1,964.00	19.36	6.43	1.88	2.52	[67]
28	CoCrFeNi**	8.19	FCC	1.03	−3.75	11.53	1,598.75	5.75	3583.31	1.16	1.27	[97]
29	CoCrFeMnNi**	8.04	FCC	0.92	−4.16	13.38	1,528.20	5.79	34.68	1.12	1.19	[1]
30	HfNbTiZr**	8.38	BCC	4.12	2.50	11.53	2,058.25	10.75	15.26	1.95	6.96	[98]
31	HfNbTaTiZr**	9.94	BCC	4.01	2.72	13.38	2,250.00	12.41	16.90	2.55	8.75	[99]
32	MoNbTaW**	13.80	BCC	2.27	−6.50	11.53	2,884.75	5.60	60.98	1.71	1.08	[93]
33	MoNbTaVW**	13.63	BCC	3.21	−4.64	13.38	2,689.80	8.54	41.17	1.75	1.17	[93]

* If there are no experimental densities provided, the densities will be calculated using Eq. (3.1).

** Listed for comparison purposes.

3.4 Results

3.4.1 Newly-designed lightweight HEAs

Figure 3.1 shows the XRD patterns of our newly-designed lightweight $Al_xCrFeMnTi_y$ HEAs. All major phases are identified. For clarity, unknown phases are not indexed. The XRD results show that all the alloys exhibit the presence of a BCC structure. Besides the fundamental diffraction peaks for the BCC structure, two peaks at about 26° and 30° are detected for all the six compositions, and they are identified as the Fe_2AlTi-type $L2_1$ structure. The XRD patterns also show the existence of the intermetallic C14 Laves phase in $Al_{1.5}CrFeMnTi$ (Figure 3.1e) and $Al_2CrFeMnTi$ (Figure 3.1f) alloys. In addition to BCC and $L2_1$ phases, some complex structures are reflected in $Al_3CrFeMnTi_{0.25}$ (Figure 3.1c) and $Al_4CrFeMnTi_{0.25}$ (Figure 3.1d), which are identified as Al_8Cr_5-type (cI52, I-43m) and $Al_{58.5}Cr_{10.3}Fe_{31.2}$-type (hR26, R3m) phases.

The microstructures of these lightweight HEAs were characterized by SEM, as shown in Figure 3.2. Alloys of $Al_3CrFeMnTi_{0.25}$ (Figure 3.2c), $Al_{1.5}CrFeMnTi$ (Figure 3.2e), and $Al_2CrFeMnTi$ (Figure 3.2f) all exhibit multi-phase structures, while $AlCrFeMnTi_{0.25}$ (Figure 3.2a) and $Al_2CrFeMnTi_{0.25}$ (Figure 3.2b) present a main BCC structure. It is worth noting that the SEM micrograph does not show enough phase contrast between phases in the microstructure of $Al_4CrFeMnTi_{0.25}$ (Figure 3.2d), although multiple phases are detected, using XRD (Figure 3.1d). The black dots appearing on the SEM images are defects produced during the casting process. Since one main purpose of the experimental part provided here is to provide more available experimental data to assess the phase-formation rules, the evidence showing single-phase or multi-phase

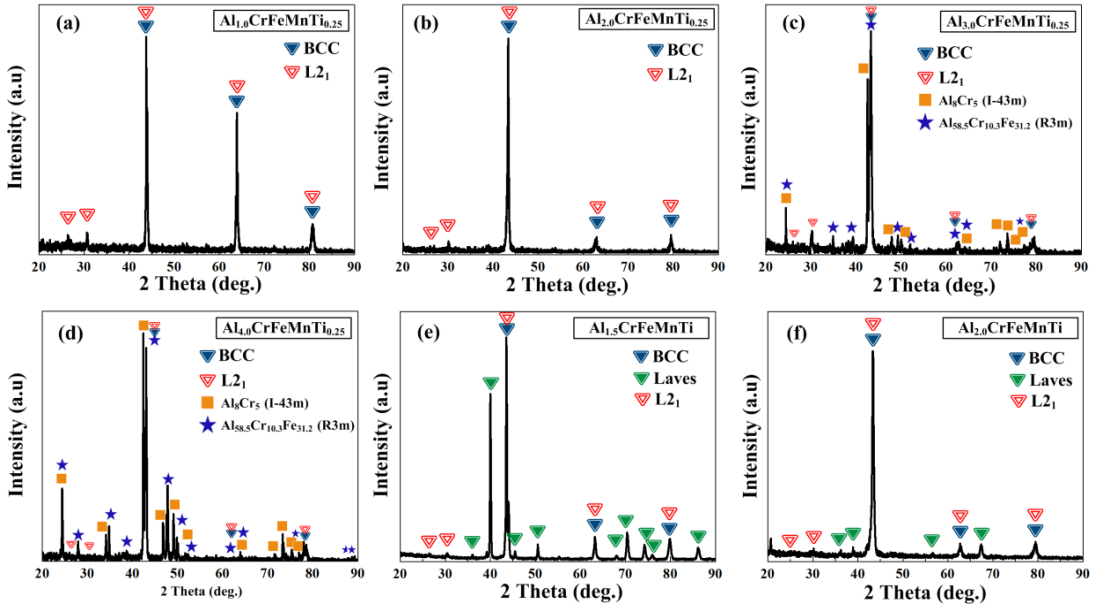


Figure 3.1 XRD patterns of a series of newly-designed lightweight HEAs: (a) $Al_{1.0}CrFeMnTi_{0.25}$; (b) $Al_{2.0}CrFeMnTi_{0.25}$; (c) $Al_{3.0}CrFeMnTi_{0.25}$; (d) $Al_{4.0}CrFeMnTi_{0.25}$; (e) $Al_{1.5}CrFeMnTi$; and (f) $Al_{2.0}CrFeMnTi$.

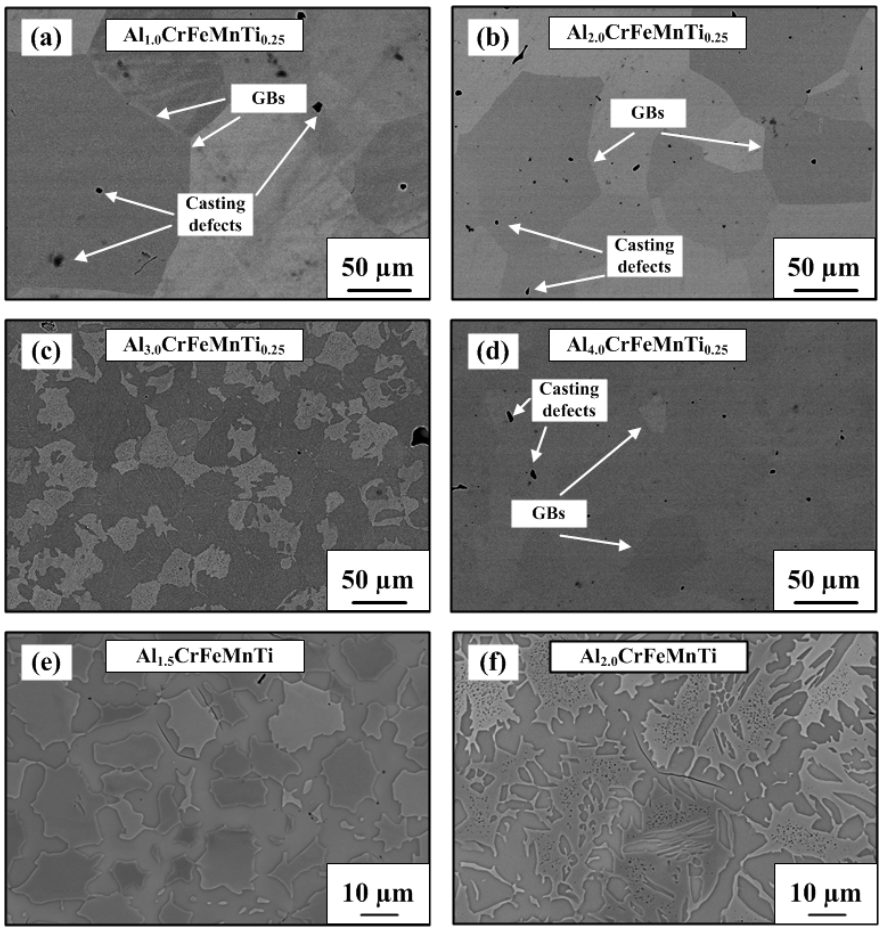


Figure 3.2 SEM images of a series of newly-designed lightweight HEAs. (a) $Al_{1.0}CrFeMnTi_{0.25}$; (b) $Al_{2.0}CrFeMnTi_{0.25}$; (c) $Al_{3.0}CrFeMnTi_{0.25}$; (d) $Al_{4.0}CrFeMnTi_{0.25}$; (e) $Al_{1.5}CrFeMnTi$; and (f) $Al_{2.0}CrFeMnTi$. (GBs represent grain boundaries)

structure is sufficient in this study.

3.4.2 Criteria based on ΔH_{mix}, δr, and Ω

As previously reported, in order to form disordered solid solutions in the as-cast HEAs, the enthalpy of mixing and atomic-radius difference rules suggested that -15 $kJ \cdot mol^{-1} < \Delta H_{mix} < 5\ kJ \cdot mol^{-1}$ and $0 < \delta_r < 5\%$ [35]. For the Ω parameter, solid solutions will form in the range of $\Omega \geq 1.1$ and $\delta_r < 6.6\%$ [70]. The relationship among the three parameters is plotted in two maps, as shown in Figures 3.3a, b. In Figure 3.3, the "SS + IM" symbol refers to the alloys showing multi-phase structure (i.e., solid-solution and intermetallic phases) listed in Table 3.2 The "SS (Lightweight HEAs)" symbol represents those lightweight HEAs forming single-phase solid solutions. The "SS (Classic HEAs)" symbol stands for those selected classic HEAs (Table 3.2) with single-phase solid solutions. Moreover, each composition symbol in Figure 3.3 (and Figures 3.4-3.7) is marked with a number, which has the one-to-one correspondence with the composition's number listed in Table 3.2. The shaded area in yellow color refers to the region where the vast majority of the compositions form a single solid solution, whereas the shaded area in blue color refers to the region where the vast majority of the compositions form "SS + IM." Note all the symbols and the shading color scheme in the following maps in Figures 3.4-3.7 have the same meaning. Figure 3.3a shows the relationship between the enthalpy of mixing (ΔH_{mix}) and atomic-radius difference (δ_r) for a series of previously-developed, classic and lightweight HEAs. The single-phase classic and lightweight HEAs are located in a range of $-16.25\ kJ \cdot mol^{-1} < \Delta H_{mix} < 5\ kJ \cdot mol^{-1}$ and $0 < \delta_r < 6.6\%$.

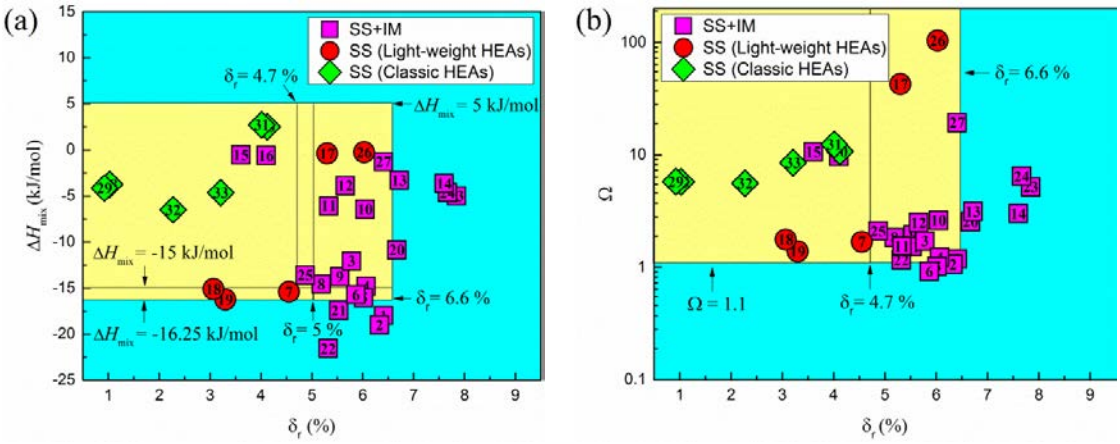


Figure 3.3 Plots of (a) ΔH_{mix} and (b) Ω versus δ_r for a series of the developed classic HEAs and lightweight HEAs (each composition symbol shown in Figures 3.3-3.7 is marked with the same composition's number shown in Table 3.2).

The Ω - δ_r relation presented in Figure 3.3b shows that all the single-phase solid-solution HEAs in this study fall into the suggested "yellow" range of $\Omega \geq 1.1$ and $\delta_r < 6.6\%$. However, many multi-phase HEAs are also located in the range of $4.7\% < \delta_r < 6.6\%$. In fact, it can be clearly seen that a stricter criterion ($\Omega \geq 1.1$ and $\delta_r < 4.7\%$) exists, compared with the reported criterion ($\Omega \geq 1.1$ and $\delta_r < 6.6\%$) [70], which separates the single-phase solid solutions from multi-phases structures in HEAs. In addition, two exceptional lightweight HEAs having δ_r larger than 4.7% are $Al_{20}Li_{20}Mg_{10}Sc_{20}Ti_{30}$ and NbTiVZr [7, 13]. Note that the $Al_{20}Li_{20}Mg_{10}Sc_{20}Ti_{30}$ alloy [7] was produced by the mechanical-alloying method. Thus, the as-synthesized alloy may be far away from its thermodynamic equilibrium, and large internal strains will inevitably be introduced into the alloys after mechanical-alloying. Therefore, this criterion may not be applicable to this alloy. The NbTiVZr alloy [69] has $\delta_r = 6.03\%$, but its $\Omega = 103.76$ is the largest among all the HEAs in this study (Table 3.2). The results shown in Figure 3.3 demonstrate that: (1) the δ_r parameter is superior to ΔH_{mix} or Ω; and (2) the critical δ_r value lies in a range of 4.7% - 6.6%, depending on alloy compositions.

3.4.3 Criteria based on ϕ, Φ, and Φ_f

To integrate the effects of thermodynamics and atomic packing on the phase formation, the single thermodynamic parameter (ϕ) [73] for selected classic HEAs and lightweight HEAs was calculated. Then, plots of ϕ against ΔH_{mix}, δ_r, and Ω are presented in Figure 3.4 to look into the potential criteria through combing these parameters. It can be clearly seen that there is a clear boundary separating the region of solid solutions

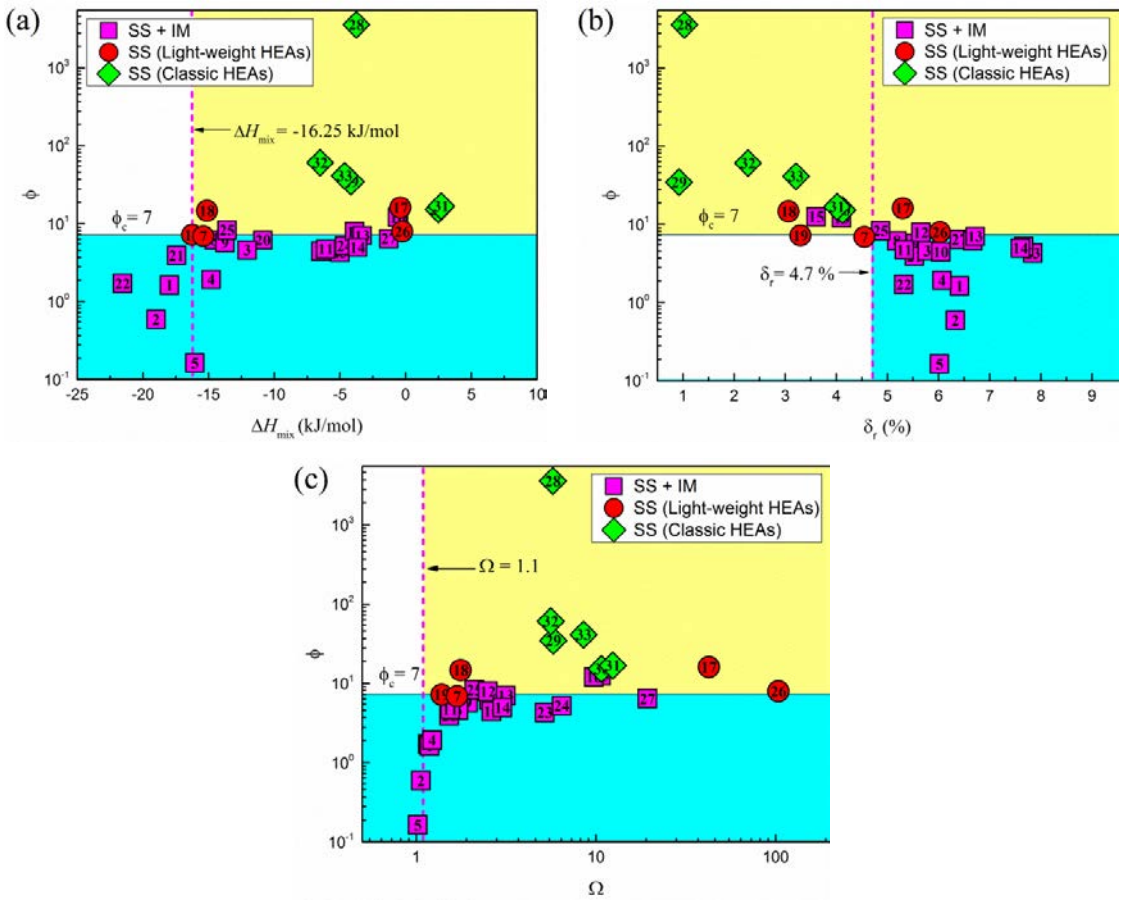


Figure 3.4 The variation of the single-parameter, ϕ, with respect to (a) ΔH_{mix}, (b) δ_r, and (c) Ω.

(in yellow color) from the region of solid solutions + intermetallics (in blue color) based on the ϕ values. The critical, ϕ_c, which is used to separate the two regions, is about 7, while in Ref. [73], this value is about 20. This trend implies that the values of ϕ in lightweight HEAs are somewhat smaller than those classic HEAs. This trend is mainly related to the fact that the lightweight HEAs usually have more negative ΔH_{mix}, which results in the decrease of ϕ [see Eq. (3.6)]. Even so, it can be hypothesized that the thermodynamic parameter, ϕ, is still somewhat effective to distinguish the region of solid solutions and that of solid solutions + intermetallics, which is helpful for the design of new lightweight HEAs.

The hypothesis for the parameters, Φ and Φ_f, is that the phase stability of an HEA is decided by the competition in the Gibbs-free energies between the solid solution and intermetallic phases at constant temperature and pressure. This hypothesis makes it possible to perform computer screening for single-phase solid solutions in a system of an arbitrary number of components. To examine the effectiveness of both parameters with the same physical meaning but different models in the present study, the relations between Φ and Φ_f with respect to ΔH_{mix}, δ_r, and Ω for all alloys listed in Table 3.2 are illustrated in Figures 3.5 and 3.6, respectively. Through the observation of these newly-produced plots, it is important to study if the combination of different rules would generate meaningful results, meanwhile, finding flaws in the currently-reported rules.

In Figure 3.5 and 3.6, it can be clearly seen that both Φ and Φ_f criteria (≥ 1) fail to predict the formation of the lightweight single-phase solid solution (such as AlNbTiV in Table 3.2), though they can predict the classic single-phase HEAs successfully. Most of

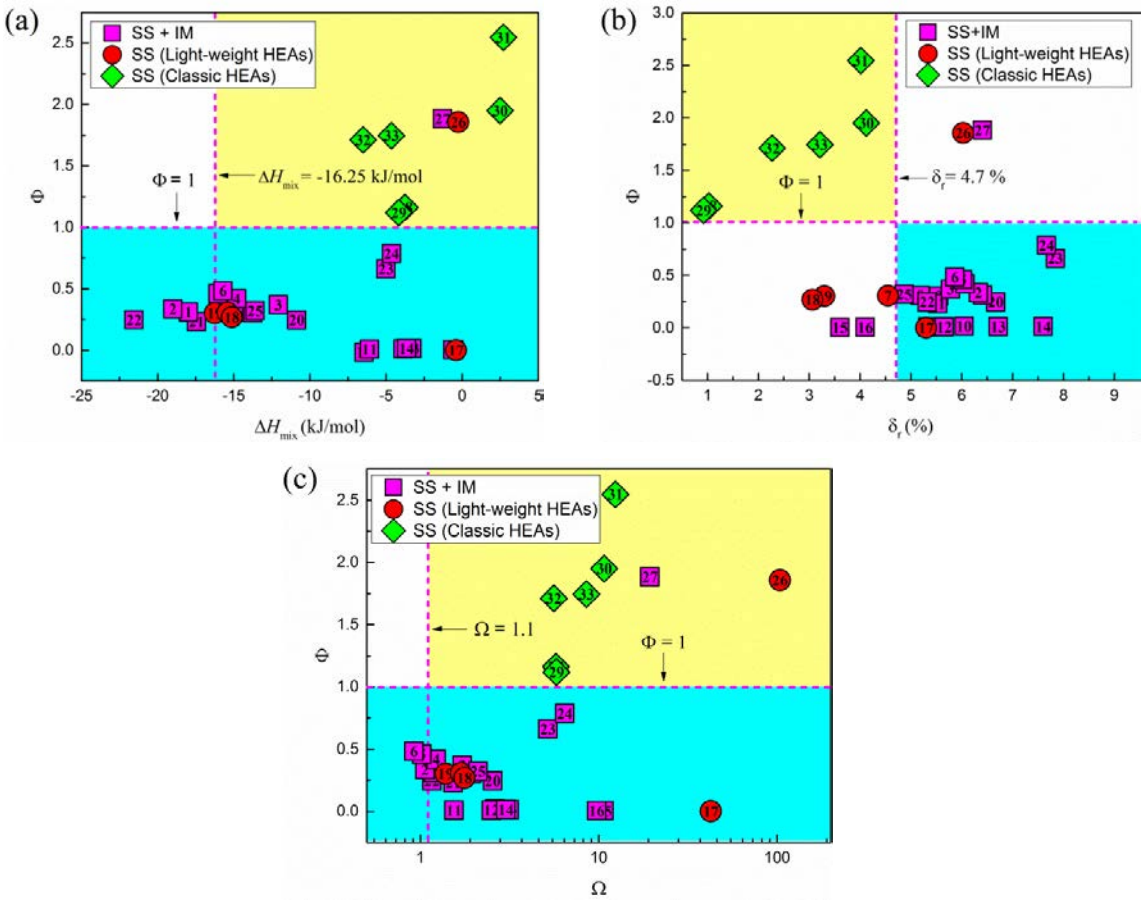


Figure 3.5 The variation of the thermodynamic parameter, Φ, with respect to (a) ΔH_{mix}, (b) δ_r, and (c) Ω.

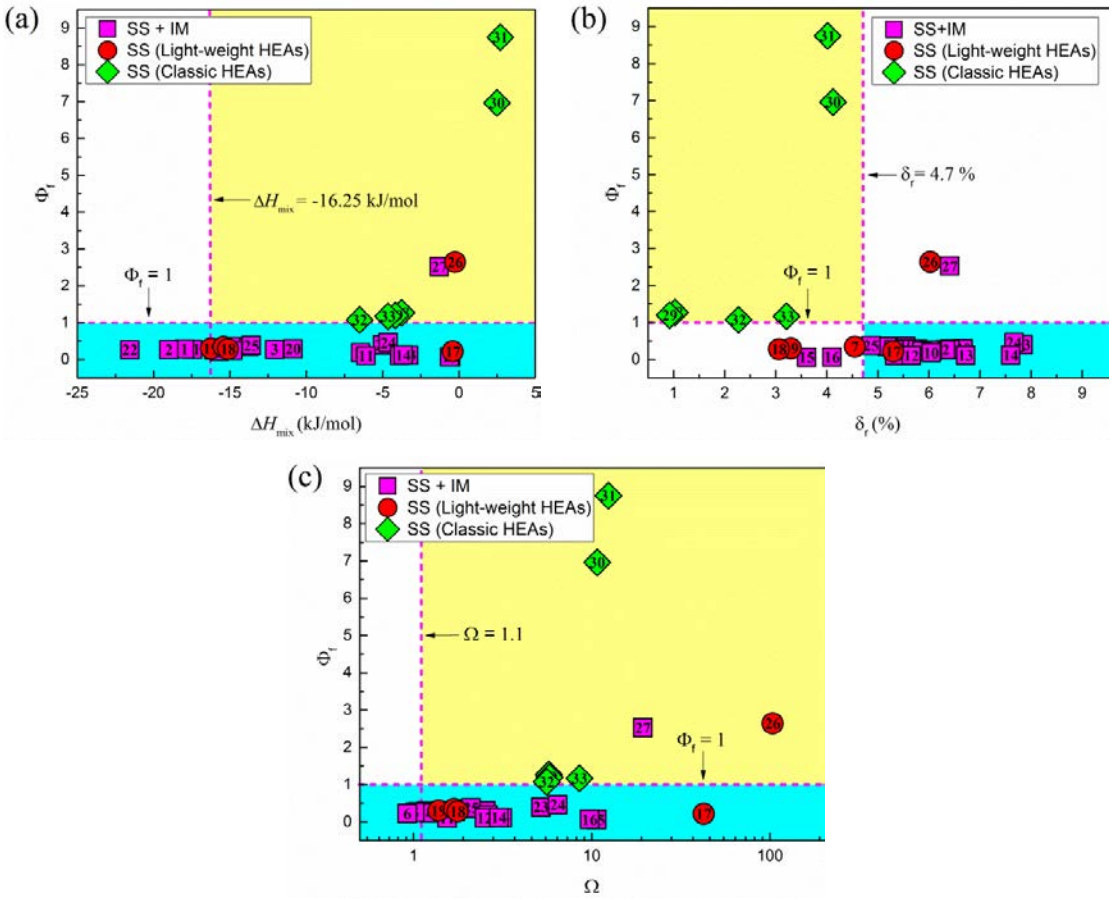


Figure 3.6 The variation of thermodynamic parameter Φ_f with respect to (a) ΔH_{mix}, (b) δ_r, and (c) Ω.

the lightweight single-phase HEAs are located in the "blue" region well below the dashed lines, Φ and Φ_f = 1, e. g., the calculated Φ and Φ_f values for single-phase AlNbTiV are 0.30 (Table 3.2). One exception is the single-phase NbTiVZr [69] alloy, which has Φ and Φ_f values of 1.86 and 2.64 (Table 3.2), respectively, despite its relatively-large δ_r = 6.03%. Conversely, although the $NbTiV_2Zr$ alloy also has large Φ and Φ_f values, it does not form the single-phase solid-solution structure, which may result from the larger atomic-radius difference (δ_r = 6.41%). In short, relying on Φ or Φ_f criterion alone cannot predict the formation of lightweight single-phase solid solutions.

Although the region of solid solutions and region of solid solutions + intermetallics cannot be distinguished, using Φ or Φ_f values ($\geq$ 1) alone, the combination of Φ or Φ_f with the atomic-radius difference, δ_r appears to be the more effective criteria than with ΔH_{mix}, or Ω, as demonstrated in Figures 3.5 and 3.6. In other words, when Φ or Φ_f is less than 1, the single-phase solid solutions may still form if the atomic-radius difference is sufficiently small (In this study, δ_r should be less than the 4.7%). On the other hand, even if δ_r is larger than 4.7%, large Φ or Φ_f parameters may still promote forming single-phase solid solution, as in the NbTiVZr alloy (Table 3.2). In fact, the formation of single-phase solid solutions is the result of the synergy of the thermodynamic factors, atomic-size effects, and other factors. Therefore, thermodynamic factors and atomic-size effects must be considered together when predicting the phase formation of lightweight HEAs.

Furthermore, in order to find more meaningful phase-formation criteria by combing different rules, Φ_f versus ϕ, and Φ_f versus Φ are plotted in Figure 3.7 In Figure 3.7a, the yellow area represents the region forming single-phase solid solutions, while the blue region stands for the area forming single-phase solid solutions plus intermetallic

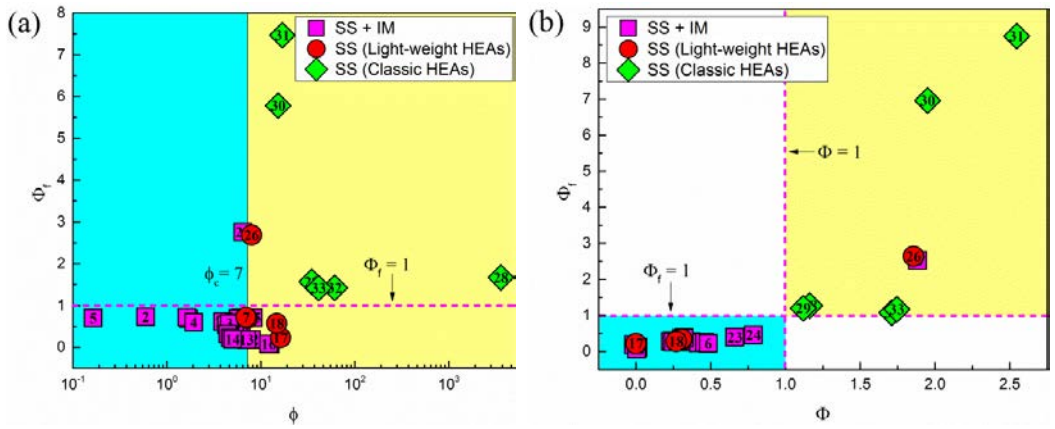


Figure 3.7 Comparison plots of (a) Φ_f versus ϕ and (b) Φ_f versus Φ.

phases, and they are separated by the ϕ_c = 7. In Figure 3.7b, the selected alloys are divided to four regions by the dash lines Φ_f = 1 and Φ =1. In examining the two plots, it is obvious that the combinations of the thermodynamic parameters can only correctly predict the formation of single-phase solid solutions in classic HEAs, while failing to predict the formation of single-phase solid solutions in lightweight HEAs.

3.4.4 CALPHAD modeling

As shown in Table 3.3, empirical rules do not always correctly predict the formation of single-phase solid solutions, and actually none of them works for all the compositions studied. Furthermore, they will not predict the crystal structure of the solid solution or compound phase either. In contrast, the CALPHAD method determines the Gibbs-free energies of all phases in the system as a function of composition and temperature, and, thus, is the ideal tool for predicting the phase formation in multi-component systems, such as HEAs, provided that the database is sufficiently reliable.

The empirical rules evaluated in this study except the Ω and ϕ parameters fail for single-phase AlNbTiV and $AlCr_{0.5}NbTiV$ alloys. For the single BCC NbTiVZr, the Ω, ϕ, Φ, and Φ_f parameters work while the ΔH_{mix} - δ_r, rule fails. On the other hand, all empirical rules work well for AlCrNbTiV, CrNbTiZr, and CrNbTiVZr, except that the Ω - δ_r rule fails for AlCrNbTiV, and these alloys show a mixture of the BCC solid solution with Laves phases.

To demonstrate the effectiveness in predicting the phase stability for lightweight HEAs, the CALPHAD calculations were carried out on selected compositions using the

Table 3.3 The effectiveness of the phase-formation prediction for lightweight HEAs using the empirical phase-formation rules (√ and × represent successful and unsuccessful predictions, respectively).

Alloys	Structure	ΔH_{mix} vs. δ_r	Ω vs. δ_r	ϕ	Φ	Φ_f
$Al_{1.5}CrFeMnTi$	BCC + $L2_1$ + Laves	√	×	√	√	√
$Al_2CrFeMnTi$	BCC + $L2_1$ + Laves	√	√	√	√	√
$AlCrFeMnTi_{0.25}$	BCC + $L2_1$	√	×	√	√	√
$Al_2CrFeMnTi_{0.25}$	BCC + $L2_1$	√	×	√	√	√
$Al_3CrFeMnTi_{0.25}$	BCC + $L2_1$ + Laves	√	√	√	√	√
$Al_4CrFeMnTi_{0.25}$	BCC + $L2_1$ + Laves	√	√	√	√	√
$AlCr_{0.5}NbTiV$	***BCC***	×	√	√	×	×
AlCrNbTiV	BCC + Laves	√	×	√	√	√
$AlCr_{1.5}NbTiV$	BCC + Laves	√	×	√	√	√
AlFeMgTiZn	BCC + IM	√	×	√	√	√
AlLiMgZnSn	FCC + IM	√	×	√	√	√
$AlLi_{0.5}MgZn_{0.5}Sn_{0.2}$	FCC + IM	√	×	×	√	√
$AlLi_{0.5}MgZn_{0.5}Cu_{0.2}$	FCC + IM	√	√	×	√	√
$AlLi_{0.5}MgCu_{0.5}Sn_{0.2}$	FCC + IM	√	√	√	√	√
$Al_{80}Li_5Mg_5Zn_5Sn_5$	FCC + IM	×	×	×	√	√
$Al_{80}Li_5Mg_5Zn_5Cu_5$	FCC + IM	×	×	×	√	√
$Al_{20}Li_{20}Mg_{10}Sc_{20}Ti_{30}$	***FCC***	×	√	√	×	×
$AlNb_{0.5}Ta_{0.5}Ti_{1.5}Zr_{0.5}$	***BCC***	×	√	√	×	×
AlNbTiV	***BCC***	×	√	√	×	×
$Al_{0.5}NbTiVZr$	BCC + Laves + Zr_2Al	√	√	√	√	√
AlNbTiVZr	BCC + Laves + Zr_2Al	√	×	√	√	√
$Al_{1.5}NbTiVZr$	BCC + Laves + Zr_2Al	√	×	√	√	√
CrNbTiZr	BCC + Laves	√	√	√	√	√
CrNbTiVZr	BCC + Laves	√	√	√	√	√
NbMoCrTiAl	BCC + IM	×	×	×	√	√
NbTiVZr	***BCC***	×	√	√	√	√
$NbTiV_2Zr$	3 BCCs	√	×	√	×	×

Single-phase solid-solution HEAs are highlighted by Italic and bold types.

TCNI8 thermodynamic database supplied by ThermoCalcTM (version 2015b, Thermo-Calc Software, Stockholm, Sweden) [100]. This database covers the complete binaries pertaining to elements, Al, Cr, Nb, Ti, V, and Zr, which are important for lightweight HEAs. The previous CALPHAD modeling using this database demonstrated good agreement with the experimental observations for various refractory BCC HEAs [81, 101-104]. The reader is referred to several recent publications [76, 104-107] for guidance on the CALPHAD modeling of HEAs. The predicted phase stability during solidification for these alloys is shown in Figure 3.8.

For AlNbTiV at equilibrium (Figure 3.8a), the database correctly predicts the formation of the BCC phase over an extremely wide temperature range. The primary BCC phase starts to form at T = 1,752 °C; the solidus temperature (T_{sol}) is 1,717 °C. At the decomposition temperature (T_{dec}) of 679 °C, the primary BCC phase decomposes to a Ti-poor BCC phase and $AlTi_3$_DO19 phase. The σ phase forms at T ≤ 485 °C. The ratio of the temperature range where the primary BCC phase is stable over the solidus temperature, namely, $(T_{sol} - T_{dec})/T_{sol}$, is 0.52. Gao [34] suggested that a ratio ≥ 0.3 typically favors the formation of a single-phase solid solution in the as-cast state. Due to slow diffusivities at low temperatures, it is unlikely to observe the BCC decomposition in a normal laboratory condition. The non-equilibrium solidification simulation was accomplished, using the Scheil-Gulliver models [108, 109], which assume equilibrium mixing in the liquid and no diffusion in solids. The simulation also predicts the formation of a single BCC solid-solution phase, as shown in Figure 3.8d.

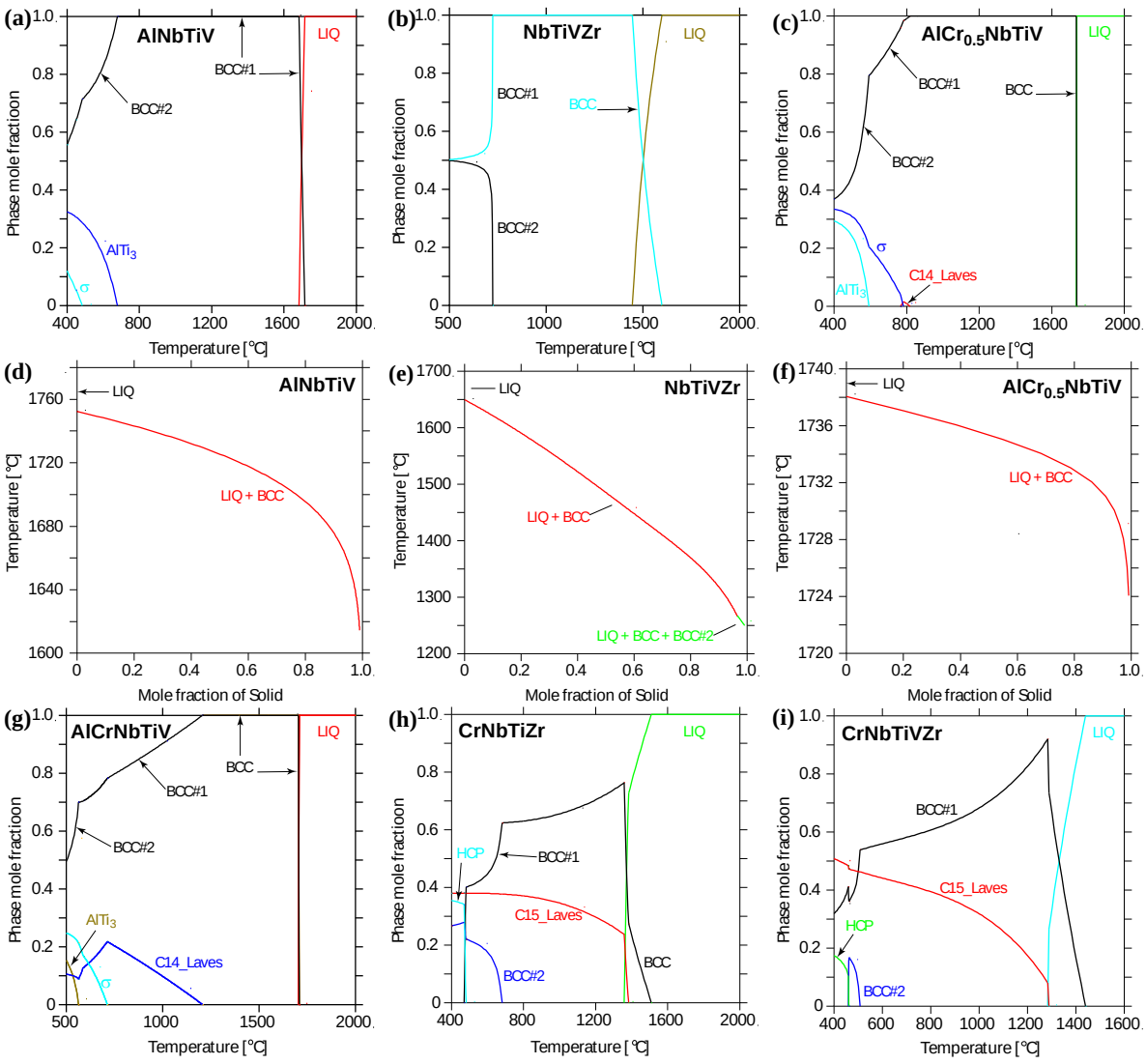


Figure 3.8 Predicted phase formation in (a, d) AlNbTiV; (b, e) NbTiVZr; (c, f) $AlCr_{0.5}NbTiV$; (g) AlCrNbTiV; (h) CrNbTiZr; and (i) CrNbTiVZr using the TCNI8 database. The non-equilibrium solidification for plots (d-f) are generated using the Scheil model [105].

For $AlCr_{0.5}NbTiV$ (Figure 3.8c), the database predicts that the BCC phase forms at T ≤ 1,739 °C; the solidus temperature is 1,734 °C. The C14 Laves phase forms in a narrow temperature range (765-819 °C). The σ phase forms at T ≤ 782 °C. As the temperature decreases, the BCC phase decomposes to the BCC#1 phase that is poor in Nb and Ti (593–765 °C), and then to the BCC#2 phase that is very rich in V but poor in Cr and Nb at T ≤ 593 °C. The $AlTi_3$_DO19 phase forms at 593 °C. The calculated ratio of $(T_{sol} - T_{dec})/T_{sol}$ is 0.46. The Scheil simulation also predicts the formation of a single BCC phase (Figure 3.8f). Using the true bulk composition reported by Stepanov et al. [24], the equilibration calculation predicts that the C14 Laves phase forms at T = 739-883 °C; and the solidus is 1,724 °C. In fact, Stepanov et al. observed the formation of a single BCC phase when homogenized at 1,200 °C and the C14 Laves when annealed at 800 °C, which is in agreement with the predictions shown in Figure 3.8c.

For AlCrNbTiV (Figure 3.8g), the calculated liquids temperature from the database is 1730 °C; the solid temperature is 1726 °C. The primary BCC phase decomposes to the BCC#1 phase and C14 Laves phase at T ≤ 1206 °C. AlTi3_DO19 forms at T ≤ 563 °C, and the σ phase forms at 712 °C. The calculated ratio of $(T_{sol} - T_{dec})/T_{sol}$ is 0.26. Using the true bulk composition reported in Reference [24], the equilibration calculation predicts that the C14 laves phase starts to form at 1,292 °C; the solid temperature is at 1,722 °C. In fact, Stepanov et al. [24] observed the formation of the C14 Laves phase in the homogenized state (i.e., at 1,200 °C) and for annealed states at 800 °C and 1,000 °C. These results generally agree with the predictions shown in Figure 3.8g.

For CrNbTiZr (Figure 3.8h), the database predicts that the primary phase is a Nb-rich BCC phase. As the temperature deceases, the Nb content in the BCC phase decreases, while the Ti content increases. At T ≤ 680 °C, the Ti-rich BCC#1 phase and Nb-rich BCC#2 phase form. The C15 Laves phase forms at T ≤ 1384 °C. For CrNbTiVZr (Figure 3.8i), the primary crystallization phase is a BCC phase that has less Zr and Cr than Nb, V, and Ti, but the Zr and Cr contents continuously increase as the temperature deceases. The C15 Laves phase forms at T ≤ 1,297 °C. For both alloys, the predicted stable phases agree well with experiments [67].

In summary, the present CALPHAD calculations using the TCNI8 database successfully predict the formation of a single BCC phase in AlNbTiV, NbTiVZr, and $AlCr_{0.5}NbTiV$, while most empirical rules fail (Table 3.3). On the other hand, the CALPHAD-predicted crystal structures of intermetallics that form in AlCrNbTiV, CrNbTiZr, and CrNbTiVZr during solidification also agree very well with experiments [24, 67]. However, caution should be noted that the database does not cover thermodynamic descriptions for all constituent ternaries (except the Al-Cr-Ti system) of the Al-Cr-Nb-Ti-V-Zr system. Therefore, the predicted results shown in Figures 3.8 and 3.9 are subject to future improvement upon the inclusion of thermodynamic descriptions for all constituent ternaries as well as further optimization with respect to the experimental data wherever available.

3.5 Discussions

3.5.1 Thermodynamic mixing properties of Al-Cr-Nb-Ti-V and Cr-Nb-Ti-V-Zr systems

In order to lower the density below 7.0 g/cm^3, additions of Al and/or Ti are required for single-phase lightweight HEAs, but excess additions of these elements may cause the formation of brittle intermetallic compounds. Even for the single-phase AlNbTiV, little tensile ductility is expected, since its compressive fracture strain is very small at room temperature (RT) [64]. It is intuitively expected that the formation of strong covalent bonds in a solid solution, which should be reflected in the enthalpy, may cause the embrittlement seen in the alloy. As a consequence, one natural question arises: How do the thermodynamic properties evolve with their additions? Furthermore, as shown in Table 3.3, those developed-empirical rules basically fail for Al-containing single-phase HEAs, but why?

This subsection attempts to answer these questions by first examining the underlying thermodynamic properties of the BCC phase for selected alloy systems, using the CALPHAD method. To eliminate the effect from the pure elements, only the thermodynamic-mixing properties are presented by setting the reference state to the BCC phase at the temperature of interest. The mixing properties of the Al-Cr-Nb-Ti-V system at 1,000 °C are shown in Figures 3.9a-c and Figures 3.9d-f for varying compositions in binaries and pseudo-binaries with respect to Ti and Al, respectively.

For $AlTi_x$, $AlVTi_x$, $AlNbVTi_x$, and $AlCrNbVTi_x$ alloys (Figure 3.9a), the total entropies of mixing (ΔS_{mix}^{BCC}) fall well below the respective ideal configurational entropies. Thus, these systems exhibit significant negative excess entropy ($^{ex}S_{mix}^{BCC}$) for the BCC phase.

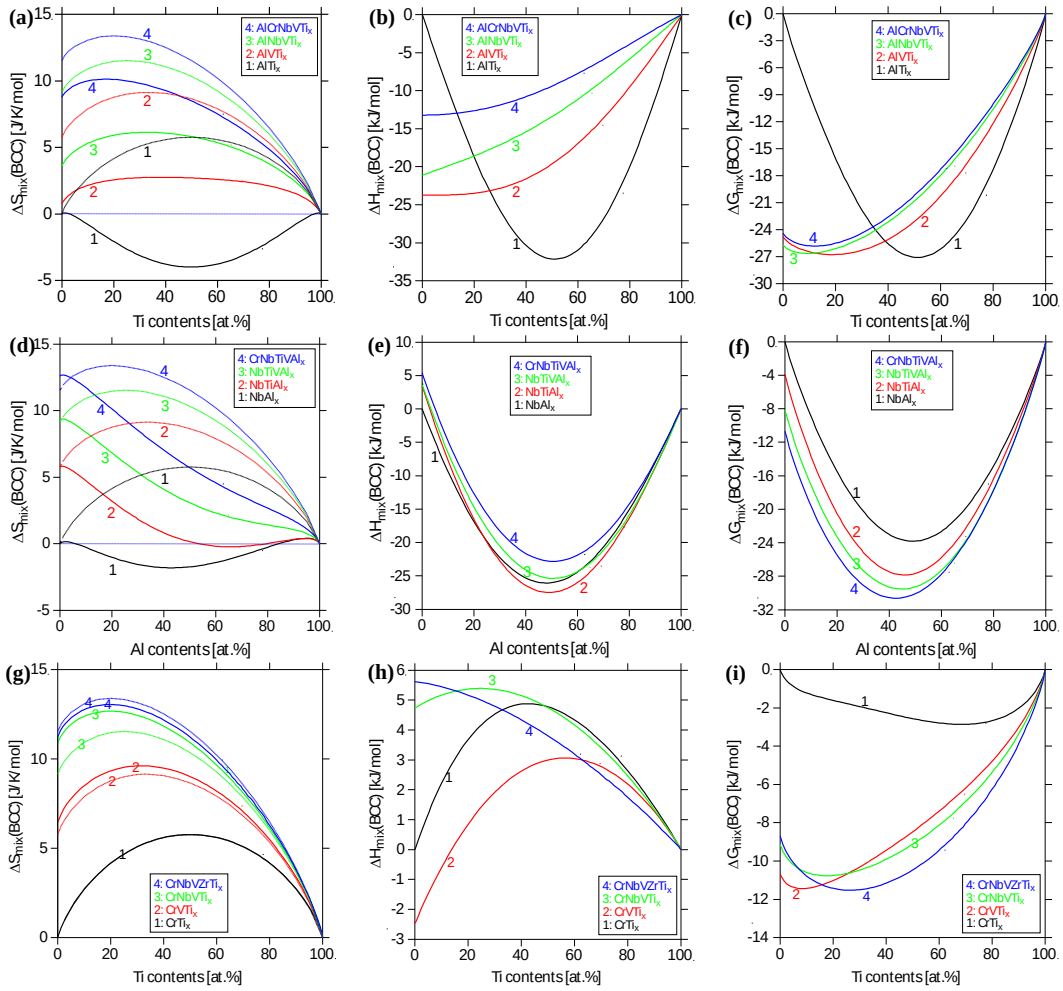


Figure 3.9 Calculated thermodynamic mixing properties of the BCC phase at 1,000 °C: (a-c) $AlTi_x$, $AlVTi_x$, AlNbVTix, and $AlCrNbVTi_x$; (d-f) $NbAl_x$, $NbTiAl_x$, $NbTiVAl_x$, and $CrNbTiVAl_x$; (g-i) $CrTi_x$, $CrVTi_x$, $CrNbVTi_x$, and $CrNbVZrTi_x$ pseudo-binaries using the TCNI8 database. $\Delta S_{\text{mix}}^{\text{BCC}}$, $\Delta H_{\text{mix}}^{\text{BCC}}$, and $\Delta G_{\text{mix}}^{\text{BCC}}$ are the entropy of mixing, enthalpy of mixing, and Gibbs-free energy of mixing for the BCC solid-solution phase , respectively. The reference state is the BCC phase at 1,000 °C. The dashed curves in (a), (d), and (g) are the ideal configurational entropies.

The excess entropy (${}^{ex}S^{\phi}_{\text{mix}}$) of a solution phase (φ) is defined by the difference between the total entropy of mixing ($\Delta S^{\phi}_{\text{mix}}$) and the ideal configurational entropy, as determined in Eq. 3.9:

$$ {}^{ex}S^{\phi}_{\text{mix}} = \Delta S^{\phi}_{\text{mix}} + R\sum_i c_i \ln c_i \tag{3.9}$$

Similarly, the significant negative excess entropy is also observed for $NbAl_x$, $NbTiAl_x$, $NbTiVAl_x$, and $CrNbTiVAl_x$ alloys (except compositions close to the "terminals" in $CrNbTiVAl_x$ and $NbTiVAl_x$, see Figure 3.9d). Also, the compositions with the maximum entropy of mixing deviate substantially from their equimolar compositions (see Figure 3.9d). Note that the $\Delta S^{\text{BCC}}_{\text{mix}}$ values are negative for nearly the entire compositional ranges for both Al-Ti and Al-Nb binaries (Figures 3.9a,d), suggesting that another entropy source, such as the vibrational entropy of mixing, may be extremely negative and dominate the total entropy of mixing.

The enthalpies of mixing ($\Delta H^{\text{BCC}}_{\text{mix}}$) (see Figures 3.9b,e) at the equimolar compositions are very large negative values, and, thus, they contribute significantly to the Gibbs-free energies, as shown in Figures 3.9c,f (Since $\Delta G_{\text{mix}} = \Delta H_{\text{mix}} - T\Delta S_{\text{mix}}$). It is noteworthy that for those M-Ti binaries and pseudo-binaries, the lowest $\Delta H^{\text{BCC}}_{\text{mix}}$ (-32 kJ/mol) occurs at 50 at.% Ti in the Al-Ti binary system, but the value for each system becomes less negative quickly with increasing the number of components (Figure 3.9b). In contrast, for those M-Al binary and pseudo-binaries (see Figure 3.9e), the lowest $\Delta H^{\text{BCC}}_{\text{mix}}$ for each system occurs in the vicinity of 50 at.% Al, due to the strong ordering tendency to form the CsCl-type B2 phase.

To differentiate the effects of Al and Ti additions, the thermodynamic-mixing properties of the Cr-Nb-Ti-V-Zr system are shown in Figures 3.9g-i. It is clear that the absence of Al boosts $\Delta S_{\mathrm{mix}}^{\mathrm{BCC}}$ substantially (if one compares Figure 3.9g to Figures 3.9a,d). $\Delta S_{\mathrm{mix}}^{\mathrm{BCC}}$ for the Cr-Ti binary behaves almost like the ideal entropy of mixing, while the $CrNbVZrTi_x$ pseudo-binary exhibits the small negative excess entropy of mixing, since its total entropy of mixing is smaller than the ideal configurational entropy. Note that the $CrVTi_x$ and $CrNbVTi_x$ alloys actually exhibit the positive excess entropy, since their total entropies of mixing are greater than their ideal configurational entropies. $\Delta H_{\mathrm{mix}}^{\mathrm{BCC}}$ (Figure 3.9h) are positive except Ti-poor compositions for the $CrVTi_x$ alloys, implying repulsive interatomic interactions among these refractory metal elements. In this case, the entropy outweighs the enthalpy in the contribution to the Gibbs free energy (Figure 3.9i).

3.5.2 Common issues of empirical rules

The empirical rules proposed for the solid-solution HEAs are based on Hume-Rothery rules, thermodynamics, or their combination, and they are established, based on the available experimental data reported in the literature, which includes three main categories of the single-phase solid solution, solid solution + intermetallics, and metallic glasses. As the new experimental data emerge, it is not surprising to see that those rules may fail for certain compositions. Because most critical values that are proposed in those empirical rules are not scientifically derived. Rather, they are statistically determined based on the available experimental data. For example, the threshold value of the ϕ parameter was originally proposed to be 20, but it is identified to be 7 for lightweight HEAs in the present study. Similarly, the critical δ_r is identified to be $\leq 4.7\%$, and $\Delta H_{\mathrm{mix}} \geq$

-16.25 kJ·mol^{-1}. A similar phenomenon was also observed for the valence electron concentration (VEC). As reported, FCC phases are found to be stable at higher VEC (> 8) and instead BCC phases are stable at lower VEC (< 6.87) [71]. However, in lightweight HEAs, although VECs for all the listed lightweight HEAs are smaller than 6, most lightweight HEAs do not present the stable single-phase BCC structure. In other words, these threshold values (e.g., ϕ, δ_r, VEC, etc.) are sensitive to alloy systems and compositions, and, therefore, can be a range rather than a fixed value.

Furthermore, the HEA community has used the empirical enthalpy data for liquids, based on the Miedema model [91] to describe the interatomic interactions in the solid-solution HEAs. This out-of-convenience approach may work in certain cases, but in general, it should be avoided if possible. In fact, a prior study by Gao et al. [81] showed that: "both the sign and absolute value of $\Delta H_{\text{mix}}^{\text{BCC}}$ are not necessarily in accord with $\Delta H_{\text{mix}}^{liq}$: For example, nine alloys exhibit opposite sign while seven alloys show the significant contrast in their absolute values." Furthermore, the accuracy of the liquid enthalpy data from the Miedema model is questionable for certain alloy systems.

In order to address the enthalpy contribution for a multi-component solid solution phase, King et al. [74] first proposed to approximate it as the composition weighted sum of the enthalpy of formation of the constituent binary concentrated solid solution based on the Miedema model. However, this approach does not consider the crystal structure of the solid solution phase, and its robustness requires verification with experimental measurements, CALPHAD modeling, and/or DFT calculations.

In general, the enthalpy of mixing of a solid solution is sensitive to the crystal structure, and the value may vary among FCC, BCC, and HCP structures. As proposed in

a recent study [80], the enthalpy of formation (ΔH_f) of solid-solution HEAs with the FCC, BCC, and HCP structures should be used to establish the ΔH_f - δ_r relation. For the enthalpy of the formation of single-phase HEAs, readers are referred to recent first-principles density functional calculations [80, 89, 90, 110], since the experimental enthalpy data for HEAs are not available in the literature.

Φ and Φ_f are designed intentionally to illustrate the thermodynamic competition between the solid-solution and intermetallic phases. While the solid-solution phase contains all the principal elements for both models, the intermetallics is represented by the most stable binary compound. Furthermore, both models ignore the entropy of intermetallic compounds, and Φ_f also ignore the mixing of enthalpy for solid solutions, which have been pointed out by Senkov and Miracle [111]. Consequently, both models have thermodynamic flaws, since the phase stability of a multi-component alloy is not determined by the simple comparison of the Gibbs-free energy in a solid solution without specifying the crystal structure with that of a hypothetical or binary compound phase; rather, it is determined by the equilibrium condition that the chemical potential of each component should be equal in all phases. In fact, the simple comparison of the Gibbs-free energy among phases is only valid for the unary system when to determine phase equilibria.

Also, ignoring the enthalpy contribution of the solid-solution phase, as exercised by Troparevsky et al. [72], can severely underestimate the Gibbs-free energy of certain solid-solution phases if the interatomic interactions among constituent elements are very strong, as evidenced in $AlCrNbVTi_x$ (see Figure 3.9b) and $CrNbTiVAl_x$ (see Figure 3.9e). The present CALPHAD modeling predicts ΔH_{mix}^{BCC} to be -32, -26, -24, -22, -18, and -12

kJ/mol for AlTi, AlNb, AlNbTi, AlTiV, AlNbTiV, and AlCrNbTiV, respectively, at 1,000 °C. On the other hand, the enthalpies of formation for solid-solution phases and intermetallics estimated from the Miedema model may suffer from the inaccuracy issue. Furthermore, using the most stable binary compound to represent the competing intermetallic phase in a multi-component system may overestimate its thermodynamic stability. The combined consequence is that these models will underestimate the likely compositions that may form single-phase solid solutions. For example, forming a single BCC-phase in AlNbTiV was predicted by CALPHAD modeling (Figure 3.8a,d), and was experimentally verified [64], but Φ and Φ_f parameters as well as the ΔH_f - δ_r relation fail to predict the formation of a single solid-solution phase. Nonetheless, the calculated Φ and Φ_f values generally show remarkable similarity for alloys listed in Table 3.2 except certain compositions that contain Al and Mg and/or Li, and those that contain Hf. The similarity between Φ and Φ_f shown in Table 3.2 can be understood, through the ratio

$$\frac{\Phi}{\Phi_f} = \left|\frac{\Delta H_{\text{mix}}^{ss} - T_{\text{m}}\Delta S_{\text{mix}}}{T_{\text{ann}}\Delta S_{\text{mix}}}\right|\left|\frac{\Delta H_f^{\text{DFT}}}{\Delta H_f^{Mid}}\right| \approx \left|\frac{\Delta H_{\text{mix}}^{ss}}{T_{\text{ann}}\Delta S_{\text{mix}}} - 1.82\right|\left|\frac{\Delta H_f^{\text{DFT}}}{\Delta H_f^{Mid}}\right| \qquad (3.10)$$

where Φ and Φ_f can be obtained from Eqs (3.7) and (3.8).

For those alloys with similar values of Φ and Φ_f, $\frac{\Delta H_{\text{mix}}^{ss}}{T_{\text{ann}}\Delta S_{\text{mix}}} \approx -1$ and $\left|\frac{\Delta H_f^{\text{DFT}}}{\Delta H_f^{Mid}}\right| \approx \frac{1}{3}$ can be found from the calculated corresponding parameters, which lead to the ratio of $\frac{\Phi}{\Phi_f} \approx 1$. The special ratio between ΔH_f^{Mid} and ΔH_f^{DFT} among those alloys may be attributed to the intrinsic connection between the Mediema model and DFT calculations.

Lastly, for the Al-containing HEAs, the actual entropy of mixing can be substantially depressed due to strong interatomic interactions between Al and TMs. For example, the calculated ΔS_{mix} are -4, -2, +2, +3, +6, and +10 J/(mol·K) for AlTi, AlNb, AlNbTi, AlTiV, AlNbTiV, and AlCrNbTiV, respectively; they are well below the corresponding ideal configurational entropy (Figures 3.9a,d), especially for the binary and ternary alloys. The much lowered entropy for the Al-containing HEAs may contribute to the additional uncertainty when predicting the solid-solution formation, using those empirical rules.

3.5.3 Perspectives of future design of lightweight HEAs

As demonstrated in the present and other studies, the CALPHAD method is the ideal approach to predict the phase stability in multi-component systems, such as HEAs. The main limitation of CALPHAD is the reliability of the thermodynamic database. A robust self-consistent database for HEAs requires the optimization of all constituent binaries and ternaries over the entire composition and temperature ranges. When such a database is not available, reliance on empirical rules, phase-diagram inspections, and density functional theory (DFT) modeling may be necessary. In fact, Gao et al. [80] has demonstrated an effective approach that combines the phase-diagram inspection, CALPHAD modeling, first-principles DFT calculations, and ab initio molecular dynamics simulations, and suggested hundreds of new single-phase equimolar HEA compositions. For example, Gao suggested quaternary and higher-order equimolar compositions in the Dy-Er-Gd-Ho-Lu-Sc-Sm-Tb-Tm-Y system, Ba-Ca-Eu-Sr-Yb system, Mo-Nb-Ta-Ti-V-W system, and Mo-Nb-Re-Ta-Ti-V-W system [80].

Strong attractive interactions between Al and TMs, and between Ti and late TMs (such as Mn, Fe, Co, and Ni) cause the formation of very stable intermetallic compounds, and, thus, the formation of single-phase HEAs that contain Al and/or Ti in high contents is difficult. Therefore, the total number of single-phase lightweight HEAs is very limited, and their densities are generally above 5.5 g/cm^3 (see Table 3.2). On the other hand, for practical applications, the alloy compositions do not need to be equimolar or near-equimolar ratios, and most importantly, multi-phase microstructures are usually desirable to balance various materials properties, especially the excellent combination of strength and ductility. Therefore, from the application point of view, a rational approach for the future design of lightweight HEAs with a density less than 5.0 g/cm^3 can be described below:

(1) Identify the main alloying elements in addition to the dominant principal element (such as Ti, Al, or Mg), based on the target-properties requirement.

(2) Use the high-entropy concept to adjust the bulk composition so as to maximize the solubility of key strengthening (or ductilizing, anti-oxidation, etc.) alloying elements.

(3) Predict phase stability using the CALPHAD method, DFT modeling, and/or empirical criteria, and design processing and heat-treatment routes to optimize the microstructure.

(4) Fabricate the down-selected alloys and characterize their microstructures and mechanical (and other) properties.

(5) Refine alloy design by repeating the above procedures.

3.6 Conclusions

The present study investigated the phase formation in $Al_xCrFeMnTi_y$, assessed various empirical rules pertaining to lightweight HEAs, and carried out CALPHAD modeling on Al-Cr-Nb-Ti-V and Cr-Nb-Ti-V-Zr systems. The following conclusions were reached:

(1) Empirical rules are not conclusive in predicting the solid-solution formation, and they are susceptible to the alloy systems and compositions that are assessed. As new experimental data emerge, these rules are subject to reevaluation. Consequently, the proposed threshold values pertaining to those empirical rules are sensitive to alloy systems and compositions, and can fluctuate within a range of values. For lightweight HEAs, the following criteria have been identified: $\phi_c \geq 7$, $\delta_r \leq 4.7\%$, and $\Delta H_{mix} \geq -16.25$ kJ·mol^{-1}

(2) The combination of Φ or Φ_f with δ_r appears to be more effective criteria than with ΔH_{mix} or Ω to differentiate SS from SS + IM.

(3) For certain HEAs with strong interatomic interactions among constituent elements, such as Al-containing HEAs, empirical rules may severely underestimate the free energies of the solid-solution phases by ignoring the enthalpy contribution of the solid-solution phase.

(4) The present CALPHAD modeling using the TCNI8 database successfully predicts the single BCC phase in AlNbTiV, $Al_{0.5}$NbTiV, and NbTiVZr, while most empirical rules fail to do so.

(5) The calculated entropies of mixing (ΔS_{mix}^{BCC}) for the BCC phase at 1,000 °C are -4, -2, +2, +3, +6, and +10 J/(mol·K) for AlTi, AlNb, AlNbTi, AlTiV, AlNbTiV, and

AlCrNbTiV, respectively; they are well below the corresponding ideal configurational entropy, especially for the binary and ternary alloys. Therefore, these systems exhibit the noticeable negative excess entropy with the BCC structure.

(6) The present CALPHAD modeling predicts that the enthalpies of mixing ($\Delta H_{\text{mix}}^{\text{BCC}}$) for the BCC phase at 1,000 °C are -32, -26, -24, -22, -18, and -12 kJ/mol for AlTi, AlNb, AlNbTi, AlTiV, AlNbTiV, and AlCrNbTiV, respectively.

(7) Forming Al-containing equimolar lightweight HEAs with a density less than 5.5 g/cm^3 is very challenging due to very attractive interatomic interactions between Al and TMs. As such, future efforts could be shifted towards Al-rich (or Ti-rich, or Mg-rich) alloys that contain large amounts of desirable solute elements, which may dissolve in the solution and/or promote the formation of beneficial precipitates, taking advantage of the high-entropy concept.

CHAPTER IV

PHASE STABILITY AND TRANSFORMATION BEHAVIORS OF A LIGHTWEIGHT HIGH-ENTROPY ALLOY

4.1 Introduction

Recently, HEAs have shown interesting potential due to their unique nature and potential outstanding physical and mechanical properties [1-4, 7, 13-15, 30, 35, 112-114], which offer a vast alloy-design space for exploring advanced lightweight alloys. Based on the concept of HEAs, several lightweight HEAs have been designed by rationally-selecting low-density elements [22-25]. However, most current published work of lightweight HEAs only report the phase/microstructure of the HEAs and a limited set of mechanical properties [23-25]. To date, little work has been made on a systematic study of the phase stability and transformation behavior for HEAs of this type, and, consequently, guidance for future development of lightweight HEAs is very much lacking in fundamental principles and design potential. The underlying phase stability and transformation behaviors in lightweight HEAs are key factors that impact mechanical properties. Nevertheless, the compositionally-complex lightweight HEAs challenge the fundamental understanding of the phase stability and transformation behaviors [36], due to the complicated elemental-diffusion and atomic-bonding environments in HEAs [115] and strong interatomic interactions between Al/Ti and transition metals [22]. Therefore, to achieve desirable mechanical properties, it is key that phase stability and transformation behaviors are understood for the future successful development of lightweight HEAs.

Motivated by the above concerns, a new low-cost, lightweight $Al_{1.5}CrFeMnTi$ HEA (ρ = 5.31 g/cm^3) was designed. Investigation of phase stability and transformation behaviors of this alloy at intermediate temperatures (750 ~ 850 °C) is the primary objective. The design rationale for this alloy was to lower the density through the addition of Al and Ti, and to reduce the alloy cost, using inexpensive constituent elements like Fe, Mn, and Cr, rather than the more expensive elements like Ni and Co. Moreover, the additions of Al and Cr were critically necessary for the high-temperature oxidation resistance, while additions of Mn and Fe enhanced solid-solution strengthening.

The main goal of the present work is to design a lightweight HEA with a microstructure that resembles the classic γ/γ' microstructure found in Ni-based superalloys [21]. It has been shown that the Fe-Al-Ti alloy system can form a BCC and $L2_1$ aligned/coherent two-phase microstructure analogous to the γ/γ' coherent microstructure in Ni-based superalloys [116, 117]. Furthermore, the previous research suggests that $L2_1$ has the greater creep resistance than B2 and $L1_2$ phases because of the limited slip systems available in the alloy [118-120]. Hence, the newly-designed HEA will target to achieve similar BCC and $L2_1$ coherent microstructures through selecting elements of Fe, Al, and Ti.

The $Al_{1.5}CrFeMnTi$ alloy is composed of BCC, $L2_1$, and C14-Laves phases, where the $L2_1$ phase is coherently distributed within the BCC phase in the as-cast state. During high-temperature service, the morphology, size, coherency, and spatial arrangement of the $L2_1$ precipitates will inevitably evolve due to growth, coarsening, and/or phase transformations. In addition, the amount of the C14-Laves phase within the microstructure needs to be controlled for optimal mechanical properties. Therefore, the primary

objectives of this study are to (1) investigate the thermodynamic stability of the Al-Cr-Fe-Mn-Ti quinary system by conducting focused experiments, and combining with CALPHAD modeling and first-principles simulations; (2) study the precipitation behavior of the $L2_1$ phase with respect to the nucleation, morphology, size, coherency, and spatial distribution; and (3) probe the atomic structure and diffusivities of the liquid using ab initio molecular dynamics (AIMD) in relation to the observed as-solidified microstructure. The fundamental understanding of the phase stability and transformations of the $Al_{1.5}CrFeMnTi$ alloy will provide the pertinent alloy-design guidance for developing future lightweight HEAs.

4.2 Materials and Methods

4.2.1 Sample preparation and hardness test

The $Al_{1.5}CrFeMnTi$ alloy used in this investigation was fabricated by arc-melting the constituent elements [purity > 99.9 wt.% (weight percent)], and then drop casting into a water-cooled copper hearth. To achieve a homogeneous distribution of elements in the alloy, the melting and solidification processes were repeated five times. Annealing temperatures, 750, 850 °C, 1,000 °C, and 1,200 °C, were chosen to study the phase stability and transformation behaviors in this alloy. Each as-cast specimen was sealed in an evacuated quartz capsule and annealed at 750, 850 °C, and 1,200 °C for 168 hours (h) (except for the 1,000 °C for 504 h). The annealed samples were water quenched quickly to preserve the equilibrium states.

Vickers microhardness was performed in the BCC + $L2_1$ two-phase region of the as-cast HEA using a BUEHLER MICROMET 2101 microhardness tester. The testing load

was 10 g, and the holding time was 15 s. Measurements were repeated eight times at different regions.

4.2.2 Microscopy, diffraction, and atom-probe tomography

The microstructures were investigated, using SEM, electron-backscattering diffraction (EBSD), energy-dispersive spectroscopy (EDS), and transmission-electron microscopy (TEM) techniques. The crystal structures were identified by the synchrotron XRD on the 11-ID-C beam line at the Advanced Photon Source (APS), Argonne National Laboratory. The bulk specimens were 1 mm thick, measured by a beam energy of 111 keV with a beam size of 0.5 x 0.5 mm. The phase evolution at different temperatures was detected by neutron diffraction, at the Nanoscale-Ordered Materials Diffractometer (NOMAD), Oak Ridge National Laboratory, the Spallation Neutron Source (ORNL, SNS). The neutron-diffraction experiments were conducted over a wide temperature range from room temperature to 1,400 °C on NOMAD, using an aerodynamic levitator [115, 121, 122]. Each temperature was held for 5 minutes. The microstructure was characterized, by SEM, using a LEO Gemini 1525 field-emission scanning-electron microscope equipped with the backscattering electron (BSE) detector and EDS. The TEM imaging was performed on ZEISS LIBRA 200 HT FE MC coupled with EDS. The SEM specimens were initially polished to mirror finish using the 1,200-grit SiC paper and, subsequently, vibratorily polished, using the 0.05 μm SiC suspension for the final surface clarification. Thin foils converted into 3 mm diameter disks for TEM observations were prepared by ion milling using 3 kV Ar ions and an incident angle of ± 4°. The TEM specimens were cooled by liquid N2 during ion milling.

Sharp-tip specimens for atom-probe tomography (APT) were made, using a FEI Nova 200 focused ion beam (FIB) [123, 124]. The APT measurements were performed, employing a local electrode atom probe (LEAP 4000X HR, CAMECA Instruments, USA) [125]. The APT acquisition temperature was set at 50 K. The pulse frequency and fraction were 200 kHz and 20%, respectively. The APT data was reconstructed and analyzed, using the IVAS 3.6.12 software provided by CAMECA Instruments.

4.2.3 CALPHAD modeling

Thermodynamic calculations were carried out, using the PandatTM [126] software and PanHEA database developed by the Computherm, LLC. Its simple idea is based on the thermodynamic law that a system with a given composition, temperature, and pressure attains the state of the lowest Gibbs energy under these given conditions. The most important advantage of the CALPHAD method is to predict the higher-order phase diagrams via the extrapolation from its constituent lower-order systems, such as binary and ternary systems. This method has been successfully employed in the design and processing control of HEAs [107]. The application of the CALPHAD method requires both the computational software and thermodynamic database. Unlike the traditional thermodynamic database focusing on the regions of one or two major components, the HEA thermodynamic database needs to cover almost the entire compositional space of a multi-component system.

4.2.4 AIMD simulation

AIMD simulations of the liquid structure at 1,873 K (1,600 °C), 2,073 K (1,800 °C), and 2,273 K (2,000 °C) were performed, using the Vienna Ab Initio Simulation Package (VASP) [127, 128], a plane-wave pseudo-potential software, in a canonical ensemble (i.e., a constant mole, volume, and temperature). Projector augmented-wave (PAW) potentials [129] and the revised Perdew-Burke-Ernzerhof (PBE) [130] gradient approximation to the exchange-correlation functional were used. Newton's equations of motion were integrated, using the Verlet algorithm [131] with a time step of 1 fs, and the atomic-configuration relaxation and temperature were controlled by a Nose thermostat [132]. A cubic supercell of 196 atoms was built, and the liquid density was determined by adjusting the cell volume so that the pressure was zero at equilibrium. The simulations were performed at the Γ point only, and the electronic-energy-convergence criterion was set to 1×10^{-4} eV/atom at the default plane-wave cutoff energy of 275 eV for a total simulation time of 60 ps.

4.2.5 DFT calculations at zero temperature

The total-energy calculations at zero temperature were carried out on selected binary, ternary, and quaternary $L2_1$ and C14 phases to analyze the trend of the alloying element substitution. The PAW potentials [129] and the PBE [130, 133] gradient approximation for the exchange-correlation functional were used. The Brillouin-zone integrations were performed, using the Monkhorst-Pack k-point meshes [134]. A smearing parameter of 0.2 eV was chosen for the Methfessel-Paxton [135] technique. The plane-wave energy cutoff is held constant at 300 eV. All structures in the non-magnetic state

(i.e., without considering spin polarization) were optimized first, and then were re-optimized, considering the collinear spin polarization (i.e., using ferromagnetic and anti-ferromagnetic spin configurations as the initial input, respectively). Both lattice parameters and atomic coordinates were fully relaxed under zero pressure until the energy convergence reached 1 meV/atom. The configuration that resulted in the lowest energy was used for data analysis.

4.3 Results

4.3.1 Phase identification and evolution

The phases in the alloy were examined, using the SEM, EBSD, synchrotron x-ray diffraction (XRD), and in-situ neutron scattering. The low-magnification EBSD phase maps and high-magnification BSE images of the five conditions (as-cast, annealed at 750 °C, 850 °C, 1,000 °C, and 1,200 °C) are shown in Figures 4.1a-e. Each condition (i.e., as-cast and annealed states) appears to be multi-phase, that is, one BCC-based phase (red color) and one C14 phase (green color). As expected, the annealing treatments introduce some noticeable changes to the microstructure, compared with the as-cast state. Annealing at 750 °C resulted in a larger volume fraction of particles with a significantly-greater size (i.e., ~ 500 nm) distributed in the BCC matrix (SEM inset in Figure 4.1b). The formation of the C14 phase within the BCC-based phase was observed after annealing at 750 °C and 850 °C. The amount of the C14 phase decreases, and the BCC-based phase gradually becomes the primary phase as the annealing temperature increases, except for at 850 °C (Figures 4.1a -e).

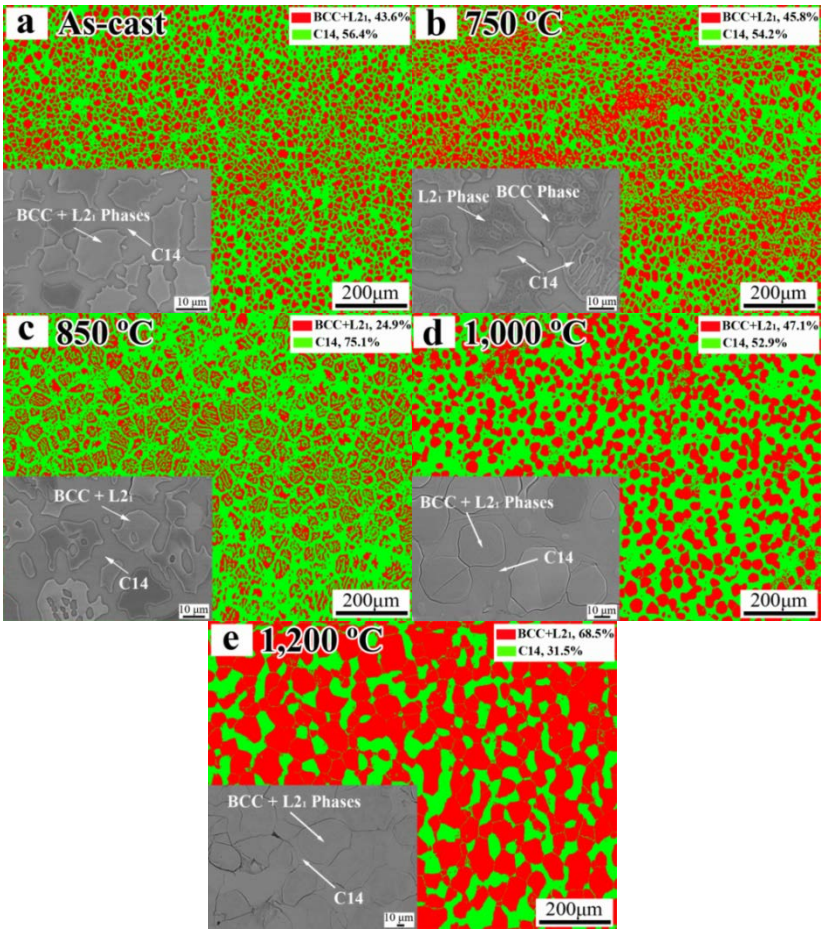


Figure 4.1 EBSD-phase mappings. (a) the as-cast state, (b) the annealed state at 750 °C for 168 h, (c) the annealed state at 850 °C for 168 h, (d) the annealed state at 1,000 °C for 504 h, and (e) the annealed state at 1,200 °C for 168 h (the red and blue regions represent the BCC + $L2_1$ and C14 phases, respectively. Meanwhile the fraction of each phase was given, and the insets are the corresponding enlarged BSE images of each state).

The synchrotron XRD patterns of the $Al_{1.5}CrFeMnTi$ alloy in as-cast, 750 °C- and 850 °C-annealed states are shown in Figure 4.2a. The series of complex Braggs peaks have been identified as the C14 phase; and fundamental Braggs peaks belonging to the BCC phase were detected in the three conditions. Except for the fundamental peaks of the BCC structure, two unique low-angle ($Q \approx 1.8$ and 2.1 $Å^{-1}$) Braggs peaks, [111] and [200], belonging to the $L2_1$ phase, are noticeable in the as-cast and 750 °C-annealed states, but almost disappear in the 850 °C annealed-state (the enlarged section in Figure 4.2a). This trend suggests that the $L2_1$ phase is thermodynamically unstable at 850 °C. Using single-peak-fitting procedures, the lattice parameters of BCC and $L2_1$ phases are determined to be: $a_{BCC}^{\text{as-cast}} = 2.9583$ Å and $a_{L2_1}^{\text{as-cast}} = 5.9392$ Å for the as-cast state; and $a_{BCC}^{750\ °C} = 2.9420$ Å and $a_{L2_1}^{750\ °C} = 5.9141$ Å for the 750 °C-annealed state. Consequently, the lattice-misfit (δ) between BCC and $L2_1$ phases is calculated to be 0.38% for the as-cast state and 0.51% for the 750 °C-annealed states (Eq. 4.1):

$$\delta = \frac{2\left(a_{L2_1} - 2a_{BCC}\right)}{\left(a_{L2_1} + 2a_{BCC}\right)} \tag{4.1}$$

Furthermore, to visually observe the phase transformation and stability of this alloy, in-situ neutron scattering at elevated temperatures were conducted, using aerodynamic levitation and laser heating [115]. As shown in Figure 4.2b, five different temperatures, including RT, 800, 1,000, 1,200, and 1,400 °C, were selected to collect the neutron-diffraction data. At room temperature, the as-cast alloy was composed of $L2_1$, BCC, and C14 phases. When the temperature exceeded 1,000 °C, the $L2_1$ phase disappears since the unique $L2_1$ peaks disappear (as the blue arrows indexed in Figure 4.2b shown),

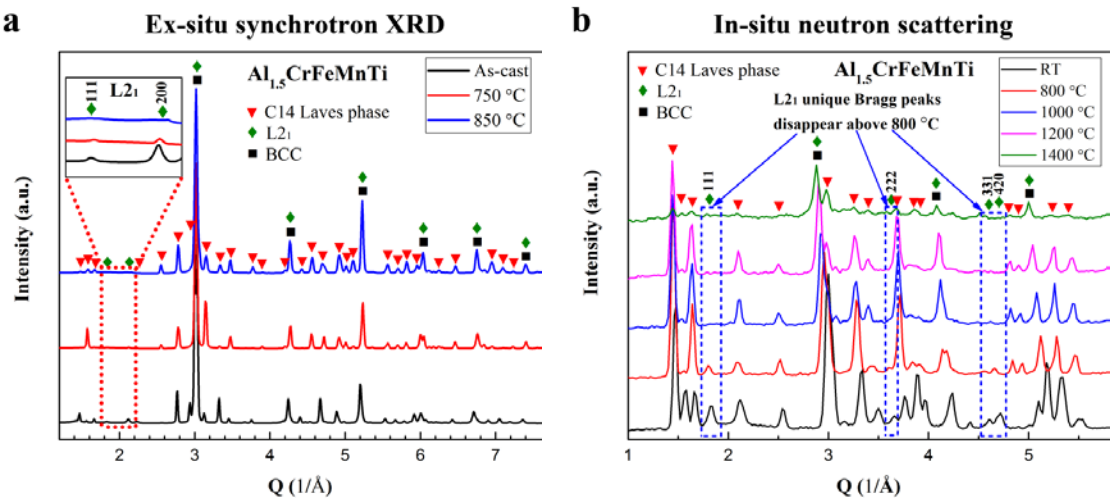


Figure 4.2 Diffraction patterns of the $Al_{1.5}CrFeMnTi$ alloy. (a) ex-situ synchrotron X-ray diffraction patterns in the as-cast, 750 °C-annealed, and 850 °C-annealed states, and (b) In-situ neutron scattering at RT, 800, 1,000, 1,200, and 1,400 °C.

including (111), (222), (331), and (420). The results are consistent with the experimental observations in the TEM, as discussed later. When annealing at 1,400 °C, the diffraction peaks of the C14 phase become very weak, indicating that the amount of the C14 phase decreases, accordingly, to a very small amount.

4.3.2 TEM characterization

To further identify the crystal structures of constituent phases, TEM was performed. The representative bright-field (BF) and dark-field (DF) TEM morphologies of BCC-based and C14 phases in the as-cast state are given in the Figure 4.3. To characterize the $L2_1$ particles in the BCC matrix, the DF, selected-area electron diffractions (SAEDs), and high-resolution TEM (HRTEM) images were conducted for the as-cast, 750 °C-, and 850 °C-annealed states, in Figures 4.4a, 4.4b, and 4.4c, respectively.

Figure 4.4a shows the DF, SAEDs, and HRTEM micrographs of the as-cast state. SAEDs were obtained through tilting the zone axis to $<001>_{L2_1+BCC}$ and $<110>_{L2_1+BCC}$. There is no obvious difference between the DF images taken along the $<001>$ and $<110>$ directions. Thus, no B2 phase is present in the three conditions. Therefore, the DF image of $L2_1$ particles was taken, using the (010)-type superlattice reflection along the $<110>_{L2_1+BCC}$ zone axis. As seen in Figure 4.4a, highly-ordered spatially-distributed $L2_1$ particles are present in the BCC matrix with a size of ~ 30 nm, which are coherent with the BCC matrix. The morphology of BCC/$L2_1$ phases in the as-cast state shown on the DF image is analogous to that of the classical γ / γ' in Ni-based superalloys [136]. It is worth noting that side-band reflection spots are found around the superlattice reflection spots. These side-band reflection spots should be due to the modulated structure formed during

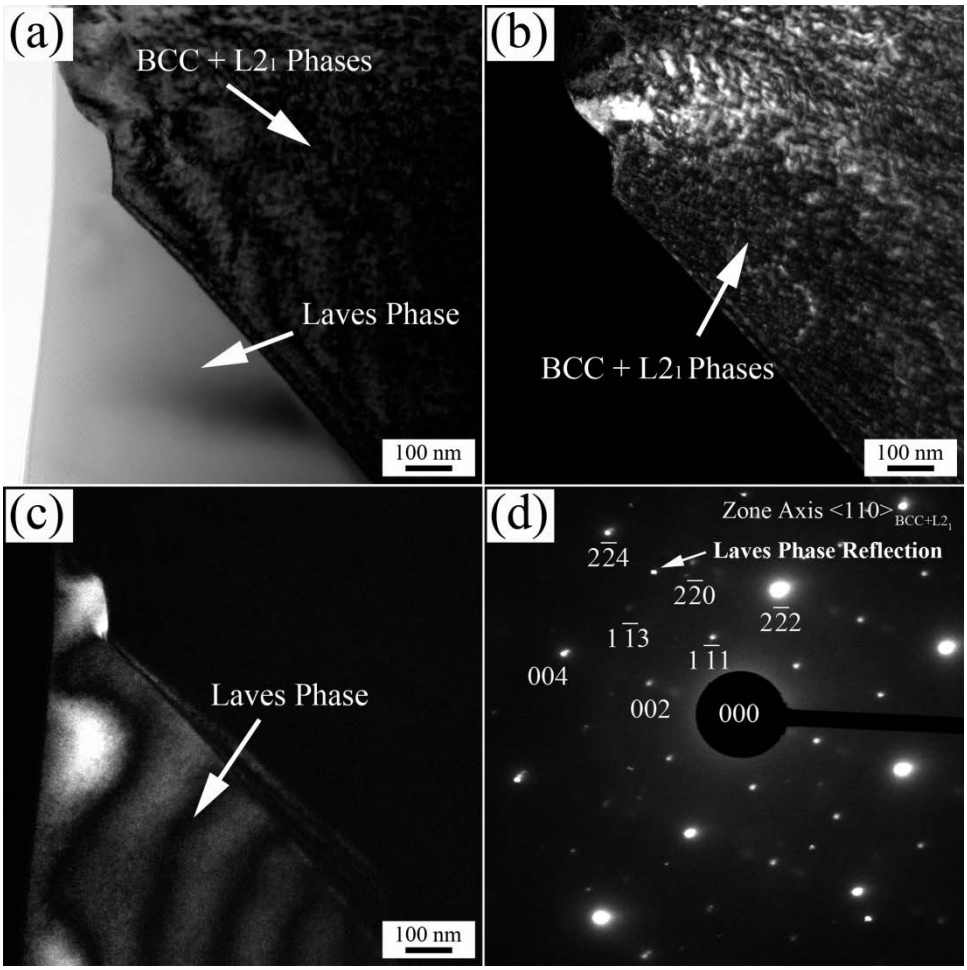


Figure 4.3 TEM images of the as-cast HEA. (a) bright-field image, (b) dark-field image using the common diffraction spots of $L2_1$ and BCC phases, (c) dark-field image using the diffraction spot of the C14 Laves phase, and (d) the selected area electron diffraction (SAED) pattern along $<110>_{L2_1+BCC}$.

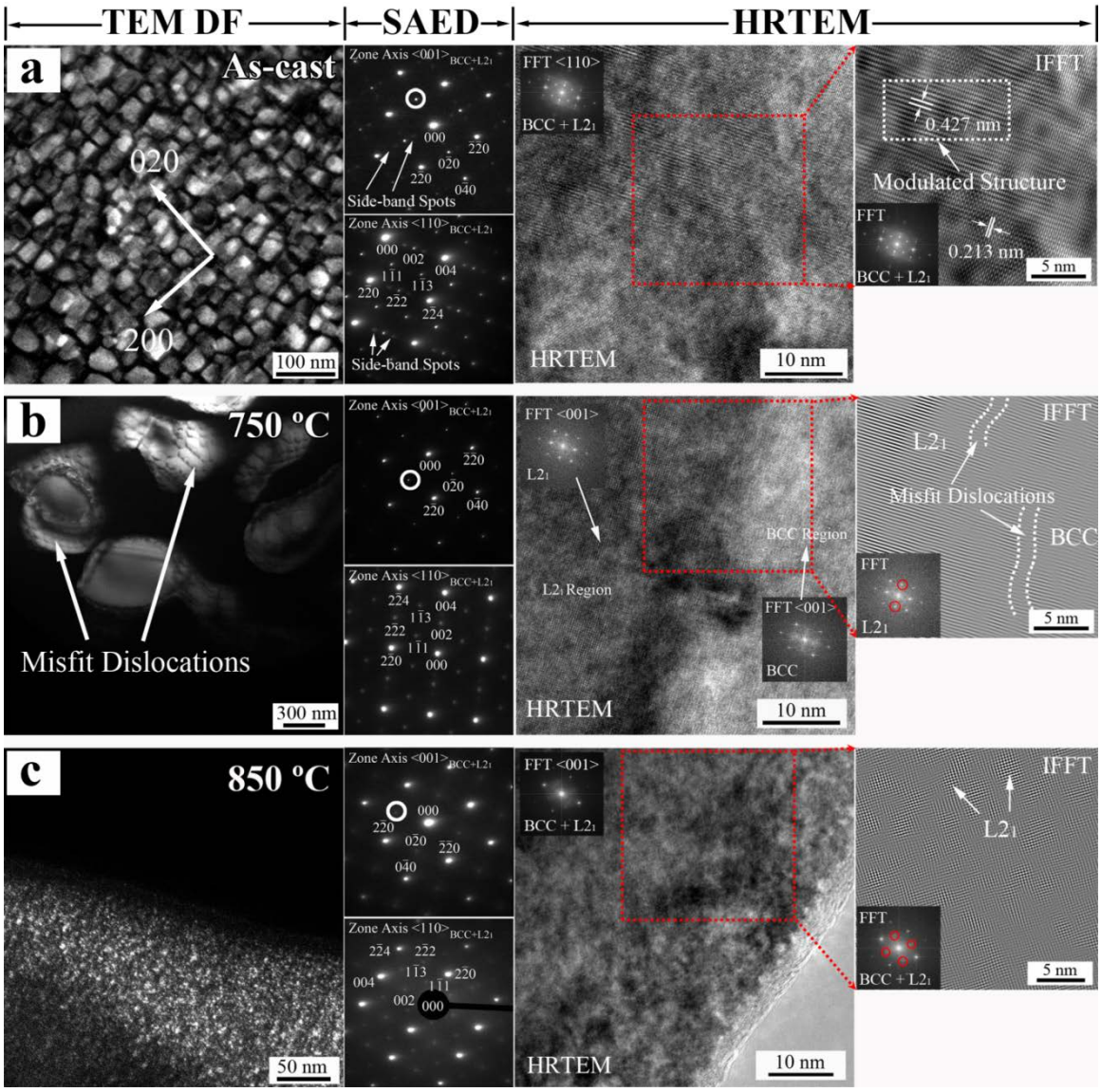


Figure 4.4 TEM DF, SAED, and HRTEM micrographs of different states. (a) the as-cast specimen, (b) aged at 750 °C for 168 h, and (c) aged at 850 °C for 168 h, showing the $L2_1$ particles in the BCC matrix.

the casting process, which was further demonstrated by the HRTEM and Inverse Fast Fourier Transform (IFFT) shown in Figure 4.4a.

After annealing at 750 °C for 168 h, the DF, SAEDs, and HRTEM micrographs (Figure 4.4b) show that the $L2_1$ particles grow and coarsen, resulting in large irregular particles with a size of about 500 nm. These results are consistent with the observed particles in the SEM inset of Figure 4.1b. As presented in the HRTEM and corresponding IFFT, misfit dislocations are present at the interface between $L2_1$ precipitates and the BCC matrix, indicative of a large lattice misfit. The loss of the $L2_1$/BCC coherency is the natural consequence of coarsening via the coalescence of the precipitates, as exhibited on the DF image in Figure 4.4b.

Figure 4.4c presents the DF, SAEDs, and HRTEM images of the annealed specimen at 850 °C also for 168 h. The DF image reveals the appearance of very fine $L2_1$ precipitates (~ 4 nm); and the superlattice reflection spots unique to the $L2_1$ phase are very weak along the zone axis of $<110>_{L2_1+BCC}$. The IFFT image using the $L2_1$ order reflection spots also indicates that the $L2_1$ order is a very short range, suggesting the nucleation stage of the $L2_1$ phase and lack of obvious growth. Moreover, no satellites reflections around the main diffraction spots, characteristic of spinodal decomposition, were observed in the SAEDs along both $<001>$ and $<110>$ directions.

4.3.3 APT analysis

The chemical compositions of $L2_1$ and BCC phases in as-cast, 750 °C- and 850 °C-annealed states were measured by the APT, and the results are given in Table 4.1. Inspection of these results shows that the BCC phase is enriched in Cr and poor in Fe and

Table 4.1 Average compositions (at.%) of BCC, $L2_1$ (measured by APT), and C14 Laves (measured by EDS) phases in the as-cast and annealed samples. Moreover, the equilibrium compositions of each phase calculated by CALPHAD at the temperatures of 750 °C, 850 °C, 1,000 °C, and 1,200 °C are also listed in the Table. The superscript, Exp, means that the phase is measured by APT or EDS; the superscript, Eq, suggests that the phase is predicted by CALPHAD assuming the equilibrium state.

States	Phases	Chemical compositions (at.%)				
		Al	Cr	Fe	Mn	Ti
As-cast	BCC^{Exp}	28.35 ± 0.18	37.97 ± 0.19	7.73 ± 0.11	21.82 ± 0.17	4.08 ± 0.08
	$L2_1^{Exp}$	26.39 ± 0.30	7.04 ± 0.16	28.79 ± 0.30	19.81 ± 0.26	17.95 ± 0.25
	$C14^{Exp}$	25.08 ± 0.49	12.71 ± 0.48	20.80 ± 0.34	13.37 ± 0.43	27.60 ± 0.22
Annealed at 750 °C for 168 h	BCC^{Exp}	26.29 ± 0.01	33.99 ± 0.02	13.31 ± 0.01	21.21 ± 0.01	5.20 ± 0.01
	BCC^{Eq}	28.02	25.64	7.7	36.43	2.21
	$L2_1^{Exp}$	27.38 ± 0.01	11.65 ± 0.01	27.65 ± 0.01	17.93 ± 0.01	15.39 ± 0.01
	$L2_1^{Eq}$	24.91	5.31	43.93	0.74	25.1
	$C14^{Exp}$	26.47 ± 0.17	9.15 ± 0.21	21.09 ± 0.10	15.88 ± 0.14	27.41 ± 0.04
	$C14^{Eq}$	27.67	16.55	16.51	6.92	32.35
Annealed at 850 °C for 168 h	BCC^{Exp}	27.36 ± 0.09	30.46 ± 0.09	13.61 ± 0.07	21.57 ± 0.08	6.86 ± 0.05
	BCC^{Eq}	28.28	23.2	14.26	30.32	3.94
	$L2_1^{Exp}$	25.16 ± 0.42	11.41 ± 0.31	25.58 ± 0.42	18.32 ± 0.38	19.22 ± 0.38
	$C14^{Exp}$	25.37 ± 0.10	9.60 ± 0.02	21.59 ± 0.04	15.78 ± 0.10	27.66 ± 0.07
	$C14^{Eq}$	26.28	13.2	22.07	6.14	32.31
Annealed at 1,000 °C for 504 h	BCC^{Exp}	27.43 ± 0.08	36.93 ± 0.08	9.33 ± 0.05	21.74 ± 0.07	4.56 ± 0.03
	BCC^{Eq}	28.48	22.05	15.91	26.15	7.41
	$L2_1^{Exp}$	26.69 ± 0.11	8.36 ± 0.07	27.87 ± 0.11	19.23 ± 0.10	17.85 ± 0.09
	$C14^{Exp}$	23.50 ± 0.04	11.53 ± 0.03	21.78 ± 0.02	14.94 ± 0.04	28.25 ± 0.07
	$C14^{Eq}$	25.74	13.29	21.05	8.1	31.81
Annealed at 1,200 °C for 168 h	BCC^{Exp}	28.44 ± 0.07	24.36 ± 0.06	16.17 ± 0.05	21.47 ± 0.06	9.43 ± 0.04
	BCC^{Eq}	28.32	20.38	17.28	20.01	13.02
	$L2_1^{Exp}$	28.48 ± 0.18	12.14 ± 0.13	24.26 ± 0.17	19.44 ± 0.16	15.51 ± 0.15
	$C14^{Exp}$	20.38 ± 0.03	12.55 ± 0.02	22.06 ± 0.01	13.79 ± 0.02	31.23 ± 0.05
	$C14^{Eq}$	24.63	12.63	20.47	11.04	31.23

Ti. In contrast, the $L2_1$ phase is rich in Fe and Ti and depleted in Cr. Note that the chemical composition of the C14 phase in Table 4.1 was measured, using the EDS method. The C14 phase is enriched in Ti up to 27 atomic percent (at.%) and depleted in Cr and Mn. In the as-cast state (Figure 4.5a), the 18 at.% (atomic percent) Cr isoconcentration surface highlights the locations of $L2_1$ and BCC phases and the proximity histograms which are constructed across the interphase between the large FeTi-rich particle ($L2_1$ phase) and small Cr-rich particle. For example, small Cr-rich particles are present in the large FeTi-rich $L2_1$ particle (~ 40 nm). Through the observation of the proximity histogram in Figure 4.5a (highlighted by the dark dashed boxes), Cr partitions from the $L2_1$ particles to the Cr-rich particles, while Fe and Ti partitions from the Cr-rich particles to the $L2_1$ particles. Finally, the partition behavior leads to the final Cr-rich domains containing ~ 38.31 at.% Cr, 7.46 at.% Fe, 28.88 at.% Al, 21.43 at.% Mn, and 3.77 at.% Ti. The extreme chemical similarity between these small Cr-rich particles and the BCC phase in the as-cast state (listed in Table 4.1) suggests that they are the same phase.

Figure 4.5b shows the chemical distributions of the constituent atoms in the BCC and $L2_1$ phases for the 750 °C-annealed state, respectively. The nano-scale chemical inhomogeneity of Cr, Fe, Mn, and Ti can be observed in both BCC and $L2_1$ phases, which should result from the decomposition behavior during long-time annealing. To determine the decomposition amplitude in the BCC and $L2_1$ phases, the averaged peak-to-trough Cr composition (ΔCr) was used. As shown in Figure 4.5b, the amplitudes of ΔCr determined by the Langer-Bar-on-Miller (LBM) method [137] (see the Supplementary Materials) are 6% for the BCC phase and 5% for the $L2_1$ phase after annealing at 750 °C for 168 h.

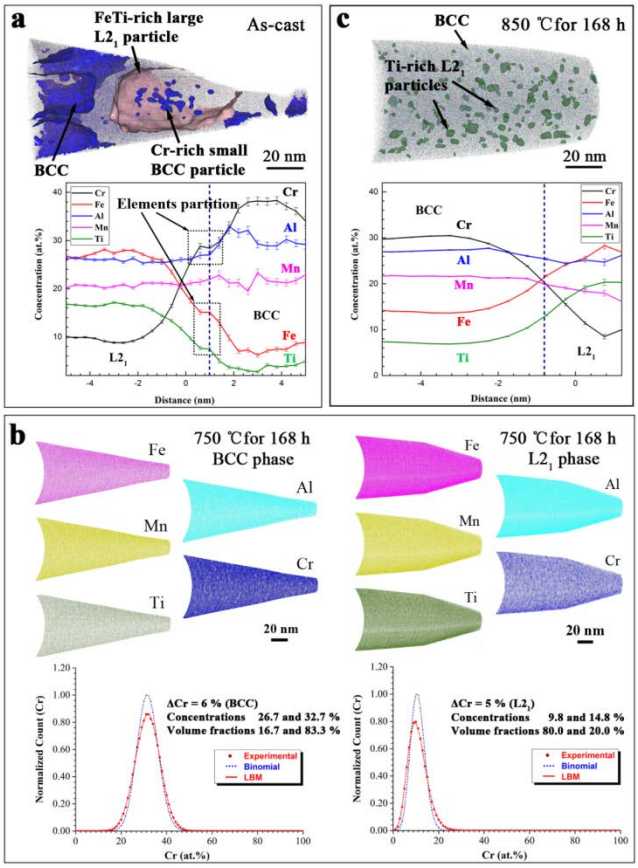


Figure 4.5 APT analysis of $Al_{1.5}CrFeMnTi$ HEA in different processing states. (a) APT results in the as-cast state, including one box with the 18 at.% Cr isoconcentration surface showing the locations of $L2_1$ and BCC phases. The proximity histogram is constructed across the interphase between the large FeTi-rich particle and small Cr-rich particle. (b) APT results of the annealed samples at 750 °C for 168 h, containing chemical mappings, experimental and binomial composition frequency distributions, and the LBM fit of BCC and $L2_1$ phases, respectively. The results show the inhomogeneity of Cr, Fe, Mn, and Ti. (c) APT results of the annealed samples at 850 °C for 168 h, showing the 12 at.% Ti isoconcerntration surfaces and the proximity histogram constructed across the interphase between the $L2_1$ and BCC phases.

Figure 4.5c displays the 12 at.% Ti iso-concentration surfaces for the 850 °C-annealed state. This figure gives the size and morphology information of the $L2_1$ precipitates. Consistent with the TEM observation in Figure 4.5c, the nano-size (~ 4 nm) Cr-depleted $L2_1$ particles are observed in the BCC matrix. The compositions of the BCC and $L2_1$ phases were determined from the proximity histogram constructed across the interphase between the $L2_1$ and BCC phases, as shown on the bottom image in Figure 4.5c. This figure shows a similar chemical distribution with the other two states, i.e., Fe and Ti are enriched in $L2_1$ precipitates, while Cr is depleted; and the BCC phase is enriched in Cr while lean in Fe and Ti.

4.3.4 CALPHAD modeling

To gain insight into the observed phase-transformation behavior, especially the evolution characteristics of $L2_1$ phases, a self-consistent thermodynamic database of the Al-Cr-Fe-Mn-Ti system was first developed, based on present experiments and density functional theory (DFT) calculations. The equilibrium calculation of the $Al_{1.5}$CrFeMnTi alloy (Figure 4.6a) shows that the BCC phase forms first at about 1,403 °C, and it is the majority phase within the temperature range from 700 °C to 1,360 °C, especially at the higher temperatures in this ranges. The fraction of the C14 phase is also high (about 45% at 800 °C). Based on the thermodynamic information, the $L2_1$ phase is stable at the temperatures below 837 °C (marked by the arrow in Figure 4.6a); this trend agrees well with experimental observations in the current work (Figures 4.2b and 4.4b). Moreover, Figure 4.6b shows the calculated isopleth of $Al_{1.5}$CrFeMnTix. As is seen in Figure 4.6b, the constituent phases (BCC + $L2_1$ + Laves-C14 phases) in the present composition of

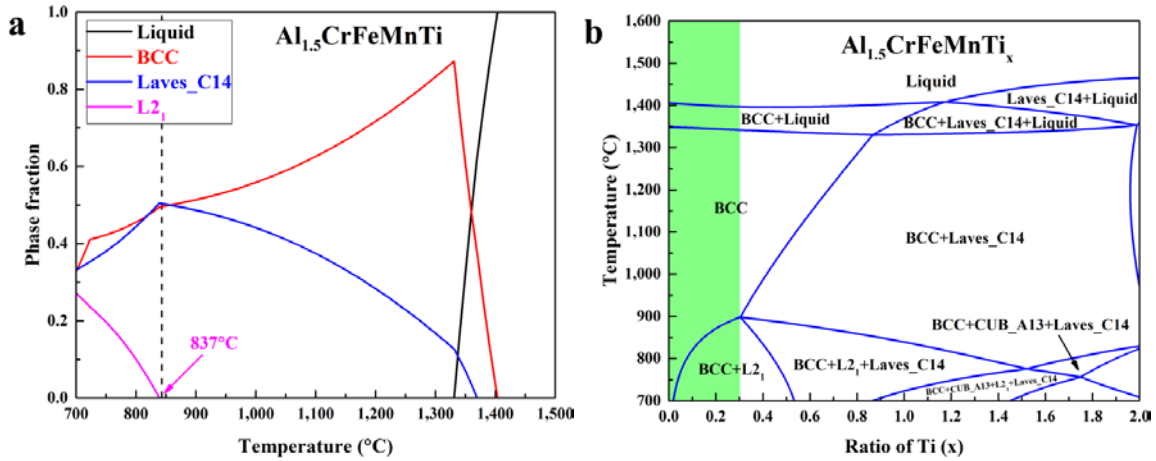


Figure 4.6 Phase diagram prediction. (a) equilibrium calculation of the $Al_{1.5}$CrFeMnTi alloy and (b) isopleth of $Al_{1.5}$CrFeMnTix.

$Al_{1.5}$CrFeMnTi match well with the prediction. It is worth noting that a BCC + $L2_1$ two-phase region is observed in the calculated isopleth (highlighted by the light green in Figure 4.6b).

In addition to the information on phase evolution versus temperature, the equilibrium composition for each phase in the $Al_{1.5}$CrFeMnTi alloy is given in Table 4.1 at 750 °C, 850 °C, 1,000 °C, and 1,200 °C for the comparison with experimental results. There is a reasonably good agreement observed between the experimentally-measured and predicted compositions (see Figure 4.7).

4.3.5 DFT calculations at zero temperature

To assist in analyzing the measured compositions of $L2_1$ and C14 phases in the alloy, DFT calculations were carried out to predict the enthalpies of formation of a variety of virtual compositions in binary, ternary, and quaternary systems. In terms of the $L2_1$ phase, DFT calculations (Figure 4.8a) predict an enthalpy of -44 kJ/mol for $AlFe_2Ti$, -19 kJ/mol for $AlMn_2Ti$, and -4 kJ/mol for $AlCr_2Ti$. In them, only the $AlFe_2Ti$ $L2_1$ was reported to be stable for the constituent ternaries. Since both Cr and Mn contents were observed in the $L2_1$ phase of the quinary $Al_{1.5}$CrFeMnTi alloy, focus is centered on $L2_1$ $Al(Cr,Fe)_2Ti$, $Al(Cr,Mn)_2Ti$, and $Al(Fe,Mn)_2Ti$. The results indicate that substituting Cr for Fe in $AlFe_2Ti$ linearly increases the energy (i.e., makes the enthalpy more positive), indicating that such substitution is energetically unfavorable. In the case of the $L2_1$ $AlMn_2Ti$, substituting Cr for Mn lowers the energy initially until 6.25 at.% Cr and then almost linearly increases the energy thereafter, suggesting a limited Cr solubility in the $L2_1$ phase when Mn is present. The change in the enthalpy of $Al(Fe,Mn)_2Ti$ is also linear.

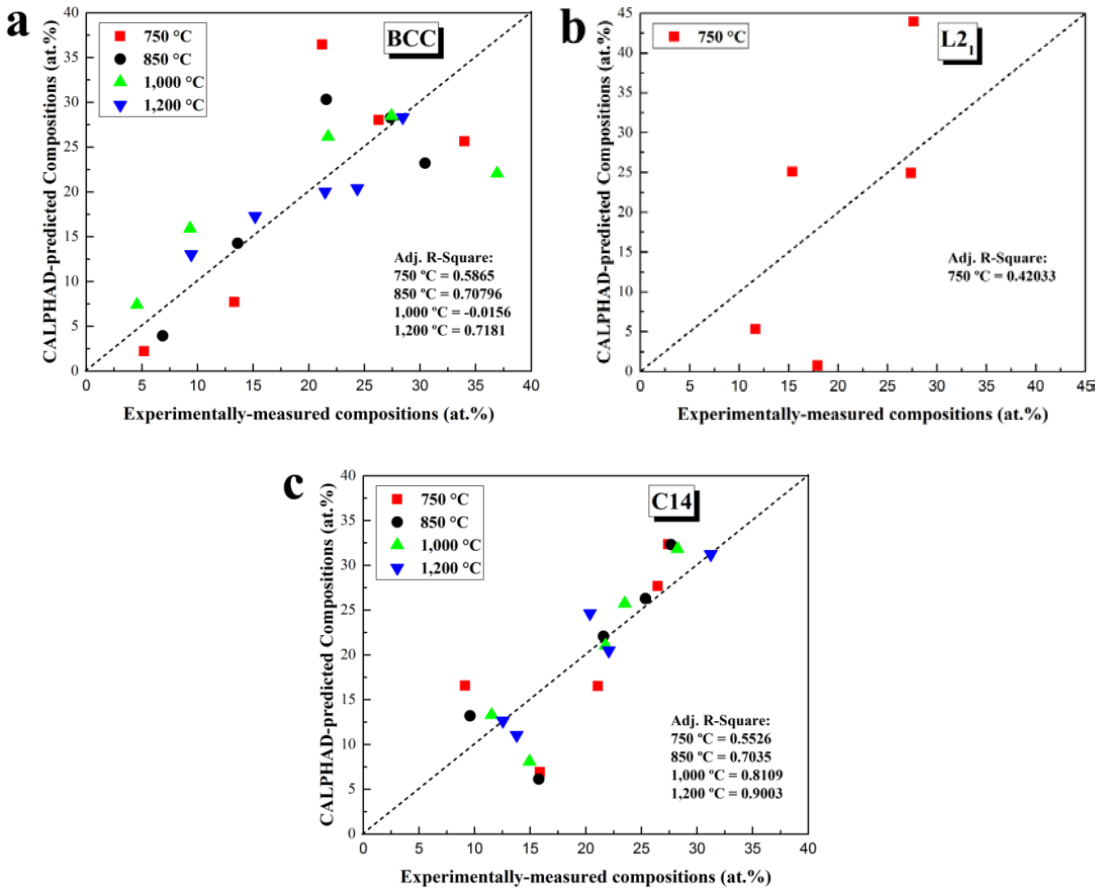


Figure 4.7 The comparisons of experimentally-measured and CALPHAD-predicted compositions in the constituent phases. (a) BCC, (b) $L2_1$, and (c) C14.

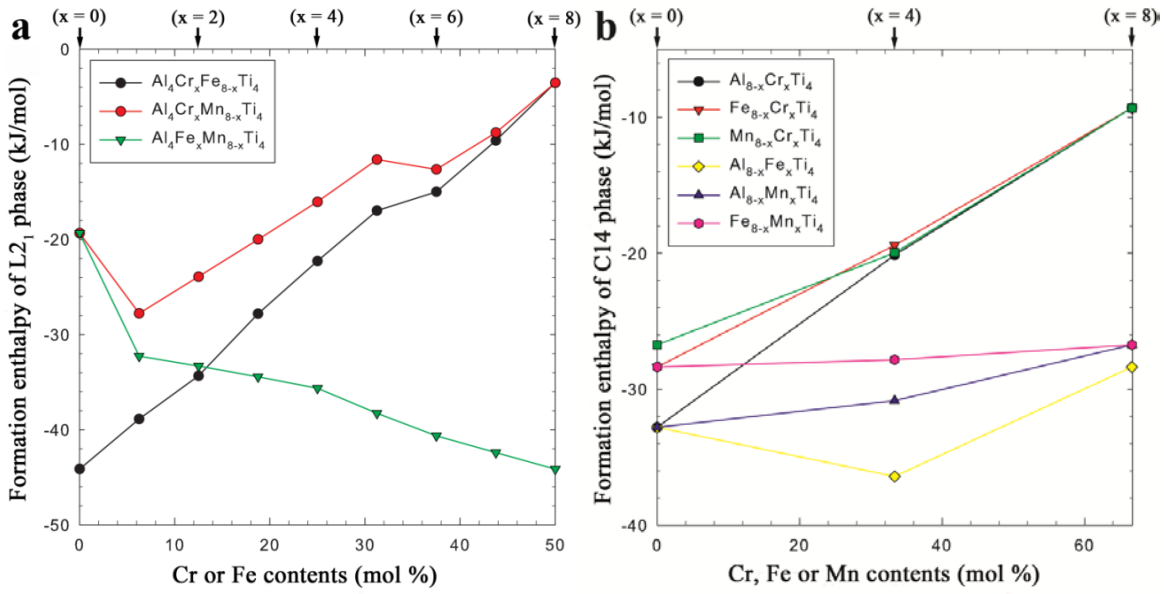


Figure 4.8 DFT-predicted enthalpy of formation. (a) selected $L2_1$ compounds and (b) C14 compounds at zero temperature.

In short, the enthalpy analysis suggests that the Cr substitution in the $L2_1$ phase is the least favorable among these five elements, and, consequently, its solubility in the $L2_1$ phase should be limited. The DFT calculations are consistent with present experiments in that the Cr content in the $L2_1$ phase is the lowest, compared to other constituent elements (i.e., 7.04 at.% Cr in the as-cast state, 11.65 at.% Cr and 11.41 at.% Cr in the 750 °C- and 850 °C- annealed states, respectively) (see Table 4.1).

A stable C14 phase is reported in binary Cr_2Ti, Fe_2Ti, and Mn_2Ti compounds, and the complete miscibility between Fe and Mn in the C14 phase is reported at the Fe-Mn-Ti 1,000 °C isotherm [138]. Among the binary C14 compounds, the DFT calculations (Figure 4.8b) show that Cr_2Ti has the highest enthalpy of -9 kJ/mol, while Al_2Ti, Fe_2Ti, and Mn_2Ti have significantly lower enthalpy that ranges between -33 and -27 kJ/mol. Substitution among these elements causes almost a linear enthalpy-composition relation except that the mixing between Fe and Al in $Al_{8-x}Fe_xTi_4$ noticeably lowers the enthalpy (Figure 4.8b). In fact, experiments [138] show that C14 Fe_2Ti can dissolve nearly 50 at.% Al at 1,000 °C in the Al-Fe-Ti ternary. In short, the enthalpy analysis together with the established binary and ternary phase diagrams [138] suggests that Al, Fe, Mn, and Ti should be the main constituent elements of the C14 phase in this quinary system, and the Cr solubility should be limited. These calculations support the measured C14 composition in the as-cast state (12.71 at.% Cr), as well as in the 750 °C- and 850 °C-annealed states (9.6 at.% Cr and 9.15 at.% Cr, respectively) (Table 4.1).

4.3.6 AIMD modeling

The atomic structure in the liquid state often reveals the useful information about the preferred interatomic bonding that may impact the formation of the disordered solid solution during solidification [3, 115, 139-141].

The partial pair distribution function (PDF) gives the information about the probability of such bond formation by measuring the intensity of near-neighbor pairs against the total random distribution. The partial PDF [$g_{ab}(r)$] was calculated, using:

$$g_{ab}(r) = \frac{V}{N_a N_b} \frac{1}{4\pi r^2} \sum_{i=1}^{N_a} \sum_{j=1}^{N_b} \left\langle \delta\left(\left|r_{ij}\right| - r\right) \right\rangle \tag{4.2}$$

where V is the volume of the super cell, N_a and N_b are the number of elements, a and b, $\left|r_{ij}\right|$ is the distance between elements, a and b, and the bracket, < >, denotes the time average of different configurations. The liquid structure of $Al_{1.5}CrFeMnTi$ shows the somewhat-preferred first-nearest-neighbor pair correlation for certain element pairs (AlFe, AlTi, and AlMn) than for other pairs (e.g., FeFe, TiTi, and AlAl) at 1,600 °C, 1,800 °C, and 2,000 °C, as shown in Figure 4.9a. This trend suggests the existence of the short-range order, albeit not strong, in the liquid, if one compares it with liquid structures of the CuNiPdPtP [3, 139] and $Al_{1.3}CoCrCuFeNi$ [115] HEAs.

Previous AIMD simulations [3, 115, 139] show that preferred bond pairs of Al-Ni, Cr-Fe, and Cu-Cu in the liquid state of the multi-phase $Al_{1.3}CoCrCuFeNi$ HEA may serve as the precursors to nucleating B2, BCC, and FCC phases, respectively, during solidification. Conversely, the lack of the potent short-range order, or chemical separation,

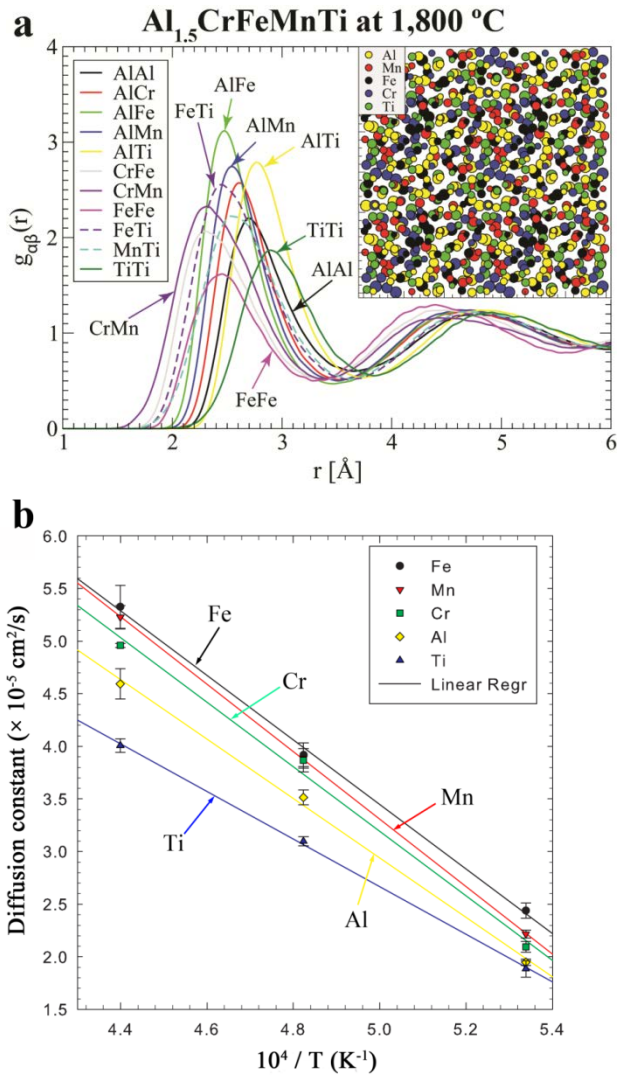


Figure 4.9 AIMD simulations. (a) selected partial PDFs of $Al_{1.5}CrFeMnTi$ at T = 1,800 °C from the present AIMD simulations (the inset shows a snapshot of the atomic structure) and (b) calculated diffusion constants for $Al_{1.5}CrFeMnTi$ from AIMD simulations as a function of inverse temperature.

is predicted in the liquid state of single-phase HEAs, including HfNbTaTiZr [3, 139, 141], MoNbTaVW [141], HfNbTaTiVZr [142], GdDyLuTbY [143], CoOsReRu [143], MoPdRhRu [143], CoCrFeNi [141], CoCrMnNi [141], and CoCrFeMnNi [141]. Note that Cr tends to form short-range bonds with unlike elements rather than the segregating into Cr clusters in CoCrFeNi [141], CoCrMnNi [141], and CoCrFeMnNi [141], and similar behavior was found for Mo in MoPdRhRu [143]. The present study tends to support the previous arguments [3, 115, 139] that a liquid structure that lacks strong elemental segregation, or potent short-range order, will likely promote the formation of disordered solid solutions as the primary crystallization phase during solidification (Figure 4.1e).

By examining the atomic trajectory, the diffusion constants were obtained by plotting the mean square displacement (MSD) versus time using the following equation:

$$D_i = \lim_{t\to\infty} \frac{\left\langle \left| R_i(t) - R_i(0) \right|^2 \right\rangle}{6t} \tag{4.3}$$

where D_i is the self-diffusion constant of the species, *i*, and $R_i(t)$ and $R_i(0)$ denote the atomic positions of the species, *i*, at time, *t*, and *t = 0*, respectively. The angular brackets denote an average over all the same species. The as-determined diffusion constants are listed in Table 4.2, and are also shown in Figure 4.9b as a function of the inverse temperature. At the three temperatures investigated (i.e., 1,600 °C, 1,800 °C, and 2,000 °C), Ti has the lowest diffusivity, followed by Al. Iron has the highest diffusivity, followed by Mn and Cr. The diffusion constants appear to satisfy an Arrhenius-type behavior within the temperature range studied (Figure 4.9b). Correspondingly, the

Table 4.2 Calculated diffusion constants ($\times 10^{-5}$ cm^2/s) and corresponding activation energies of the liquid $Al_{1.5}CrFeMnTi$ from the present AIMD simulations.

Elements	1,873 K (1,600 °C)	2,073 K (1,800 °C)	2,273 K (2,000 °C)	Calculated activation energy (kJ/mol)
Al	1.95 ± 0.03	3.51 ± 0.07	4.59 ± 0.14	76.42 ± 4.66
Cr	2.09 ± 0.05	3.87 ± 0.11	4.96 ± 0.02	77.28 ± 9.28
Fe	2.44 ± 0.07	3.92 ± 0.11	5.33 ± 0.20	69.40 ± 14.49
Mn	2.22 ± 0.04	3.89 ± 0.09	5.23 ± 0.11	76.34 ± 12.07
Ti	1.89 ± 0.08	3.10 ± 0.04	4.01 ± 0.06	67.03 ± 8.40

diffusion activation energies of the five elements are calculated (see Table 4.2). It can be seen that Cr has the largest activation energy (77.28 kJ/mol), and Ti has the smallest activation energy (67.03 kJ/mol).

4.4 Discussions

4.4.1 Phase stability, transformation, and precipitation behaviors of the $L2_1$ phase

The phase stability and transformation, and precipitation behaviors of $L2_1$ precipitates in the BCC matrix can greatly impact the mechanical behavior. Therefore, we now discuss these behaviors as follows.

The formation of the $L2_1$ phase is closely related to the chemical compositions in the alloy. The $L2_1$ phase is enriched in Fe and Ti, and depleted of Cr. By contrast, the BCC matrix is rich in Cr and lean in Fe and Ti (Table 4.1). This chemical distribution suggests a coupled role of Fe, Ti, and Al during the formation of the $L2_1$ phase in the BCC matrix. As shown in the partial PDF results simulated by AIMD (Figure 4.9a), the Al-Fe and Al-Ti pairs exhibit a higher possibility to be found as the nearest neighbors than other combinations (e.g., AlAl, FeFe, and TiTi), and as such, may promote the nucleation of $L2_1$ precipitates. It has been extensively reported that the $D0_3$ structure of Fe_3Al can evolve into the $L2_1$ structure of $AlFe_2Ti$ by the addition of Ti, where the Fe four sites at (1/2, 1/2, 1/2) will be substituted by Ti [116, 117, 144, 145]. Moreover, the DFT-predicted enthalpy of formation of $AlFe_2Ti$ has the most negative value (Figure 4.8a), indicating that $AlFe_2Ti$ is the main structure in the $L2_1$ phase. Accordingly, Cr and Mn will substitute partially on the Fe lattice sites, leading to the possible formation of $Al(Cr,Fe,Mn)_2Ti$. Since the

solubility of Cr is limited, and Ti is necessary in the $L2_1$ phase, the diffusion behaviors of Ti and Cr will play an important role in the formation of the $L2_1$ phase. As shown in Figure 4.5a (black dash boxes), the partitions of Cr to the BCC phase, and Ti and Fe to $L2_1$ indicate the presence of a chemical driving force for the formation of BCC and $L2_1$ phases. Note the calculated diffusion parameters for the elements in this alloy are shown in Figure 4.9b and Table 4.2. The Ti and Al with relatively-slow diffusion capabilities will impact the formation of energetically-favorable Fe-Al-Ti clusters (i.e., favor the nucleation of the $L2_1$). It is likely that the clustering and ordering mechanisms drive the formation of the $L2_1$ phase [146].

Although the present CALPHAD calculation predicts that the $L2_1$ phase is stable below 837 °C (Figure 4.6a), the formation of high-density $L2_1$ precipitates was observed in the quenched samples annealed at temperatures above 837 °C. This trend is due to the homogeneous nucleation from the BCC matrix during quenching from temperatures above 837 °C. It is assumed that annealing above 837 °C causes the $L2_1$ phase to dissolve. However, the $L2_1$ phase has the nucleation advantages due to the small interfacial energy between the $L2_1$ and BCC phases, resulting from the small lattice mismatch [120, 147]. Although a reasonable agreement between the CALPHAD-predicted and experimentally-measured compositions of constituent phases is achieved (Table 4.1 and Figure 4.7), a perfect agreement is not obtained, in particular, in the lower-temperature annealed states and the nanosized $L2_1$ phase. The disagreement may be accounted by multiple reasons: (1) The samples annealed at lower temperatures did not reach equilibrium; (2) there was larger uncertainty in measuring the compositions of the nano-$L2_1$ precipitates; and (3) the imperfection of the database.

The equilibrium shape of the $L2_1$ precipitates is determined by the balance between the elastic-strain energy (E_{el}) and interfacial energy (E_s) during precipitation [148, 149]. The critical size of the precipitate inclusion is expressed by [148, 149]:

$$r_{crit} = \frac{E_s}{E_{el}} = \frac{S_p \cdot \gamma_s}{2\mu\varepsilon^2 V} \frac{1-\nu}{1+\nu} \tag{4.4}$$

where S_p is the surface area of the inclusion, γ_s is the interfacial energy of the inclusion per unit area, V is the volume of the inclusion, and ε is the misfit. μ and ν are the shear modulus and Poisson's ratio, respectively. The shape of the precipitate is dominated by the elastic energy when the inclusion size is larger than r_{crit}, and by the interfacial energy when otherwise.

The total free-energy minimization criterion, combined with the critical size of the inclusion has been utilized to qualitatively explain the morphological evolution in many coherent inclusion-matrix systems [58, 120, 136, 150-152]. For the $Al_{1.5}$CrFeMnTi alloy in the 850 °C-annealed state, extremely-fine $L2_1$ precipitates (~ 4 nm) were observed within the BCC phase (Figure 4.4c). The particle morphology is ellipsoidal in nature (Figures 4.4c and 4.5c). Since the $L2_1$ phase nucleates from the BCC matrix after annealing at 850 °C, the lattice misfit is close to zero, i.e., it is fully coherent (see HRTEM, Figure 4.4c). Thus, the ellipsoid with the minimum interfacial energy is the energetically-stable shape. Also, the very low lattice misfit decreases the nucleation barrier precipitation [120, 147, 153], and is responsible for the observed high nucleation rate of the $L2_1$ phase.

In the case of the as-cast state, the highly-ordered $L2_1$ precipitates featuring the cuboidal morphology are spatially distributed in the BCC matrix (Figure 4.4a). The cuboidal morphology of the $L2_1$ phase in the as-cast state is believed to result from the elastic field generated by the large precipitate-matrix misfit (δ = 0.38%). The elastic-strain energy contributing to the equilibrium shape of the inclusion becomes dominant when the precipitate-matrix system has a higher lattice misfit, i.e., the inclusion size exceeds r_{crit}. Thus, the precipitate with a cuboidal morphology possesses a lower total energy than an ellipsoid [57, 120, 154].

Moreover, the cooling rate in the as-cast state is significantly lower than that for samples quenched after annealing at 850 °C. As a result, the $L2_1$ precipitates in the as-cast state have much longer time to coarsen during solidification, which leads to the larger lattice misfit between BCC and $L2_1$ phases. As the particle size increases, the elastic-strain field facilitates the change in the particle morphology from an ellipsoid to a cube [148, 155].

Furthermore, in the as-cast state (Figure 4.4a), the $L2_1$ precipitates not only align along the *elastically-soft* crystallographic directions, <100>, of the BCC matrix, but also maintain a minimum inter-precipitate separation. This feature can be attributed to the elastic interaction between the misfitting cuboidal precipitates that leads to long-range attractive and short-range repulsive forces [156]. In the 750 °C-annealed state, the aligned microstructure of cuboidal precipitates has disappeared, and irregular-shaped particles have formed, accompanying the appearance of misfit dislocations at the precipitate-matrix interface (see Figure 4.4b). The formation of irregular-shaped particles is attributed to the

growth and coalescence of neighboring precipitates, and this process is related to the relaxation of misfit strains by misfit dislocations. Due to the presence of misfit dislocations at the precipitate-matrix interface, the influence of the elastic stress becomes minimal, and the shape and spatial arrangement of the precipitates are governed by the interfacial energy alone. Consequently, the drive for minimizing the interfacial energy results in the agglomeration of neighboring precipitates at the expense of the disappearance of the aligned microstructure (Figure 4.4b).

4.4.2 Perspectives of the future design of advanced lightweight HEAs

The phase stability and transformation behaviors of the $Al_{1.5}CrFeMnTi$ alloy are studied here, which offers an in-depth insight of design strategy for developing lightweight HEAs in the future.

Firstly, to lower the density, light alloying elements, such as Al and/or Ti, are generally utilized for the design of lightweight HEAs. However, due to the very strong attractive interaction between Al/Ti and 3d-transition metals, brittle intermetallic compounds form readily. The C14-Laves phase (i.e., Fe_2Ti, Cr_2Ti, and Mn_2Ti) is very stable in the Cr/Fe/Mn-Ti binary phase diagrams. Thus, it is not surprising to observe its formation in a large amount in the as-cast $Al_{1.5}CrFeMnTi$ alloy. However, the present CALPHAD calculations predict that the C14 phase can be avoided by keeping Ti contents low (highlighted the light green in Figure 4.6b). An optimal composition window for $Al_xCrFeMnTi_y$ can be: $1 < x < 2$ and $0 < y < 0.3$ (here x and y refer to the Al and Ti molar ratios, respectively). The suggested range of the Al content ($1 < x < 2$) is based on our successful observation of the BCC/$L2_1$ two-phase structure in the as-cast $AlCrFeMnTi_{0.25}$

and $Al_2CrFeMnTi_{0.25}$ alloys [22]. Note the molar ratios of Cr, Fe, and Mn can be optimized for the oxidation, strength, and cost considerations.

Secondly, in order to maximize strength, ductility, oxidation resistance, etc., other main alloying elements, as well as minor elements, should be rationally manipulated, meanwhile by taking advantage of the high-entropy concept. For example, to improve precipitation strengthening, Fe is added to promote the formation of the $AlFe_2Ti$-type $L2_1$ phase. Also, the Cr content can be varied to achieve the better high-temperature performance with the enhanced oxidation resistance. In other words, the ideas of elemental additions stemming from the traditional physical metallurgy can be applied in the design of lightweight HEAs.

Thirdly, in conjunction with the experimental results, the combination of CALPHAD, DFT, and AIMD shows the powerful predictive capability on phase stabilities and transformations in the lightweight HEA. Therefore, the integrated experimental and computational approach used herein can be employed to explore other advanced lightweight HEAs. The CALPHAD method can predict the stable phases, phase compositions, volume fractions, and transformation temperatures, which provides an effective guide for materials design. With the energetics input from DFT calculations, the development of reliable CALPHAD databases can be greatly expedited. The AIMD simulations can reveal the short-range order and predict diffusion constants in the liquid state, which is important for interpreting phase formation during solidification. Under the guidance of the modeling and experimental results, a transformable dispersed coherent $L2_1$ phase can be utilized in the refined Al-Cr-Fe-Mn-Ti system. An ideal two-phase microstructure, i.e., a high-density nanosized $L2_1$ phase coherently disperses in the BCC

matrix, while much smaller BCC particles can also form in the $L2_1$ precipitates, can be suggested with high probability of success (Figure 4.10). This ideal microstructure can contribute to both the precipitation and solid-solution strengthening, crucial in developing the high-temperature strength. Note the hardness value (3.668 ± 0.177 GPa) of the BCC + $L2_1$ two-phase region in this as-cast alloy is comparable and even superior to those of commercial Inconel 718 nickel-based superalloys (2.932 ~ 4.325 GPa) [157], suggesting that desirable mechanical properties of lightweight HEAs with a coherent BCC/$L2_1$ microstructure can be achieved in the future.

4.5 Conclusions

The phase stability and transformation behaviors of a lightweight $Al_{1.5}$CrFeMnTi HEA have been systematically investigated, using integrated experimental and theoretical modeling approaches. The main conclusions are summarized as follows:

(1) The newly-designed $Al_{1.5}$CrFeMnTi lightweight HEA is composed of BCC, $L2_1$, and C14-Laves phases, where the $L2_1$ phase is coherently-distributed within the BCC phase in the as-cast state. The size, shape, coherency, and spatial distribution of $L2_1$ phase were, subsequently, altered through annealing treatments at 750 °C and 850 °C. The $L2_1$ phase has great nucleation advantage due to the small interfacial energy between the $L2_1$ and BCC phases, resulting from the small lattice mismatch.

(2) CALPHAD thermodynamic modeling successfully predicted the constituent phases and the phase-transformation temperature of $L2_1$ phase (837 °C), which are consistent with the experimental results. A BCC + $L2_1$ two-phase region can be obtained in the predicted phase diagram through lowering the content of Ti.

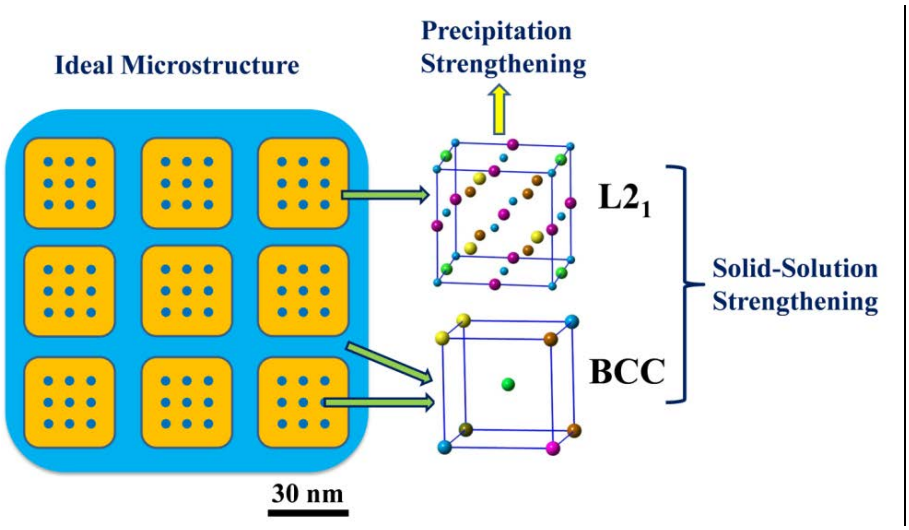


Figure 4.10 Schematic illustration of ideal microstructure in the future design of advance lightweight HEAs based on the Al-Cr-Fe-Mn-Ti system (orange and blue represent $L2_1$ and BCC phases, respectively).

(3) The DFT-predicted the enthalpies of formation of a variety of virtual compositions in binary, ternary, and quaternary systems explain the measured compositions of $L2_1$ and C14 phases. The preferred bond pairs (AlFe, AlTi, and AlMn) predicted by the AIMD simulations imply the potential formation mechanism of $L2_1$ precipitates.

(4) Based on the present study, the future design strategy of advanced lightweight HEAs is suggested here.

Overall, the present study reveals the likelihood of developing novel lightweight HEAs with a coherent BCC/$L2_1$ microstructure, featuring the lower density (below 6 g/cm^3) and cost in the future.

CHAPTER V

HIGH-THROUGHPUT DISCOVERY AND STUDY OF HIGH-PERFORMANCE PRECIPITATION-STRENGTHENED LIGHTWEIGHT HIGH-ENTROPY ALLOYS

5.1 Introduction

To develop significantly cheaper and lighter high-temperature alloys than Ni-base superalloys, precipitation-strengthened body-centered-cubic (BCC) alloys, which possess a microstructure analogous to that of the γ/γ' Ni-base superalloys, has been developed. Numerous efforts can be found in the literature in the development of novel ferritic alloys containing a disordered BCC matrix with ordered B2 (NiAl-type) and/or $L2_1$ (Ni_2TiAl-type) precipitates due to their good creep resistance at elevated temperatures and relatively lower density [119, 158, 159]. However, the emerging precipitation-strengthened ferritic alloys still face some drawbacks, such as not high enough high-temperature strength, and still expensive and heavy raw materials. To overcome these shortcomings, new alloy-design strategies for developing a new generation of precipitation-strengthened BCC alloys are required. Recently, the concept of high entropy alloy (HEA) or multi-principal element alloy (MPEA) has revolutionized the strategy of the traditional alloy design by using multi-principal components (≥ 5) instead of one or two key components [1-4, 36, 114]. This HEA-design concept opens up a new avenue for developing new-type precipitation-strengthened lightweight and low-cost BCC alloys for high-temperature structural applications [22, 52]. In the development of such materials, critical goal-oriented design strategies are the prerequisite, including cheap raw materials, low density,

high melting temperature (T_m), good oxidation resistance, great creep resistance, and high strength with acceptable ductility. Thus, a rational selection of chemical compositions is of very significance to take account of these essential factors. Our previous work [52] developed a new lightweight and low-cost $Al_{1.5}CrFeMnTi$ HEA, containing coherent nanoscaled $L2_1$ precipitates strengthened BCC matrix and C14 Laves phase. Despite of its lower density and cost than traditional ferritic alloys [119, 158, 159], the alloy is brittle due to the presence of C14 Laves phase in large volume fraction. The dissimilarity of crystal structures and different thermal expansion coefficients between the C14 Laves phase and BCC-base phase increases the tendency of cracking along their phase boundaries. Hence, the C14 Laves phase or other detrimental intermetallic phases need to be eliminated for improving the mechanical properties of the Al-Cr-Fe-Mn-Ti LWHEA, namely, generating a BCC/L21 duplex microstructure. It is well known that the microstructure of a material is determined by its composition and the processing procedure it went through [160, 161], therefore, we can produce the BCC/L21 duplex microstructure by adjusting chemical compositions and optimizing the proper manufacturing process. However, the vastness of the compositional space poses a huge challenge for efficiently screening out suitable compositions. The trial-and-error experimental method is obviously not suitable since it is extremely costly and time-consuming to screen the proper alloys in a vast composition space. This is even true for a quinary system, not to mention a higher-order ($n \geq 5$) multi-component system. Fortunately, the pace of discovering promising HEAs can, in principle, be accelerated by the development of efficient computational screening methods and tools [162, 163]. In the present work, the CALPHAD-based high-throughput computational tool is employed to

efficiently explore the Al-Cr-Fe-Mn-Ti system for the discovery of new-type precipitation-strengthened BCC LWHEAs. The subsequent detailed experimental and theoretical studies on the discovered lightweight HEAs provide insights into developing high-performance LWHEAs via the high-throughput alloy-design method.

5.2 Materials and Methods

5.2.1 The CALPHAD-based HTCMs

The CALPHAD (stands for ***cal***culation of ***pha***se ***d***iagrams) approach [160, 164-166] is currently the only method that can be used to obtain multi-component phase diagrams with enough accuracy for practical applications without the need of heavy experimental work [167]. This argument has made the CALPHAD method a key building block in the two largest driving forces in materials engineering today - ICME (Integrated Computational Materials Engineering) [168] and MGI (Materials Genome Initiative) [169]. The application of the CALPHAD method requires both thermodynamic database to provide the Gibbs energies (as a function of pressure, temperature, and composition) for the individual phases and the computational software to calculate the equilibrium state by an energy-minimization procedure. Over the past three decades, the development of the consistent multi-component thermodynamic databases has grown steadily and several commercial softwares, such as Pandat^{TM} [170], Thermo-Calc [171], FactSage [172], etc., have become available. Although the CALPHAD approach has been well accepted in the design and development of advanced materials [105, 107, 139, 173-176], its full potential has not been fully released due to the low efficiency to explore the entire composition and

temperature space of a multi-component system. Here we need to emphasize that this trend is due to the limitation of the computational tools, but not the CALPHAD method.

In order to meet the increasing demand for massive calculations in the field of HEAs, a high-throughput calculation (HTC) tool in the frame of CALPHAD is developed and implemented in Pandat^{TM} [170]. This CALPHAD-based HTC tool enables thousands of calculations in a defined compositional space to be performed automatically. Alloy compositions that satisfy user-defined criteria can then be identified through mining the thousands of simulated results. Here we would like to emphasize that the current HTC module is a combinatorial tool for both the high-throughput calculation and high-throughput screening. Its speed and efficiency are markedly improved and significantly advantageous over the conventional CALPHAD method. The HTCM of the present work is explained in detail in the supplementary document.

5.2.2 Sample preparation, microstructural characterizations, and mechanical testing

To verify the reliability of the current HTC method, eight different alloys were identified from thousands of compositions and fabricated via the arc-melting method. The nominal chemical compositions of these alloys are listed in Table 5.1. To ensure the chemical homogeneity, the ingot was melted at least six times before drop-casting. Three of the discovered HEAs, Alloy 1 ($Al_{20}Cr_5Fe_{50}Mn_{20}Ti_5$), Alloy 2 ($Al_{20}Cr_5Fe_{50}Mn_{20}Ti_5$), and Alloy 7 ($Al_{20}Cr_5Fe_{50}Mn_{20}Ti_5$), were selected for the further detailed characterizations. Scanning-electron microscopy (SEM) coupled with energy-dispersive spectroscopy (EDS), synchrotron X-ray diffraction (XRD), atomic-probe tomography (APT), and transmission-electron microscopy (TEM) were used for microstructure characterization. The samples

Table 5.1 Nominal chemical compositions of the identified eight alloys.

Alloys	Al (at. %)	Cr (at. %)	Fe (at. %)	Mn (at. %)	Ti (at. %)
Alloy 1	20	5	50	20	5
Alloy 2	25	5	50	15	5
Alloy 3	35	5	40	10	10
Alloy 4	30	10	35	15	10
Alloy 5	30	5	40	15	10
Alloy 6	30	5	45	10	10
Alloy 7	30	5	50	10	5
Alloy 8	16	5	50	24	5

for the SEM/EDS and XRD observation were polished using the vibration polishing method after finer grinding with a 1200 grit SiC paper. TEM specimen was prepared by a Ga^+ focus ion beam (FIB) with a final milling voltage of 5 keV. To high-throughput determine the mechanical properties of these new alloys, room and elevated-temperature compression tests of these eight alloys were also carried out at the strain rate of $2 \times 10^{-4}\ s^{-1}$, using the hydraulic Mechanical Testing System (MTS). Each test was repeated three times. The sample size for the compression tests is 3 mm in diameter and 6 in length.

5.2.3 In-situ neutron scattering experiments

In-situ neutron scattering experiments were performed on selected discovered alloys at the Spallation Neutron Source (SNS), Oak Ridge National Laboratory (ORNL), in order to understand the underlying deformation mechanisms and the $L2_1$ order-disorder transition behavior. In-situ neutron diffraction experiments were conducted on Alloys 1 and 7 during their uniaxial compressive deformation on the VULCAN Engineering Materials Diffractometer, SNS, ORNL. The incident neutron beam with a beam size of 5 mm × 6 mm hit the cylindrical samples with a size of ϕ6 mm × 12 mm. To obtain a better d-spacing resolution, the high-resolution (HR) mode of the neutron was chosen. During the compressive deformation of both alloys, force-control mode was used in the region of elastic and obvious plastic work hardening deformation, followed by displacement control at the late plastic deformation region. After the measurements, the data were analyzed by the single-peak fitting method, using the event-based data reduction software, VULCAN Data Reduction and Interactive Visualization softwarE (VDRIVE) [177]. The pair-distribution functions (PDFs) of Alloys 1, 2, and 7 were also measured on the Nanoscale-

Ordered Materials Diffractometer (NOMAD) instrument at SNS [121], ORNL. The total neutron scattering data were collected from room temperature to 1,050 °C/1,080 °C, using the ILL furnace installed on the NOMAD instrument. The samples were put into vanadium cans, and then heated at a ramp rate of 10 °C/min under a vacuum environment (~10^{-6} mbar). At selected temperatures, the samples were held for 24 min for data collection. To produce each total scattering function and associated PDF, the measured scattered intensities were normalized by scattering from the empty vanadium can and then subjected to a background subtraction from the empty container using the IDL software developed for the NOMAD instrument. The PDF, G(r) was obtained by a Fourier transformation of the structure function, S(Q), using a Q_{max} of 22 $Å^{-1}$ [178],

$$G(r) = \frac{2}{\pi}\int Q[S(Q)-1]\sin(Qr)dQ \tag{5.1}$$

where Q is the scattering vector, defined by $Q = \frac{4\pi \sin\theta}{\lambda}$.

The measured PDFs were fitted with the MC-calculated 2,000-atoms structure, using the PDFgui software [179].

5.2.4 Ab initio molecular dynamics (AIMD) simulations

The atomic structure and transport properties were predicted from AIMD simulations via the Vienna Ab Initio Simulation Package (VASP) [180, 181] in a canonical ensemble, i.e., a constant mole, volume, and temperature. Newton's equations of motion were integrated, using the Verlet algorithm [182] with a time step of 1 fs, and the atomic-configuration relaxation and temperature were controlled by a Nose thermostat [183]. Projector augmented-wave (PAW) potentials [184] and the revised Perdew-Burke-

Ernzerhof (PBE) [185] gradient approximation to the exchange-correlation functional were used. Cubic supercells of 200 atoms were built and the liquid densities were

determined by adjusting the cell volume so that the pressure was zero in equilibrium at T = 1,600 °C, 1,800 °C, 2,000 °C, and 2,200 °C to be 6.68, 6.61, 6.52 and 6.44 g/cm^3, respectively. A linear regression analysis suggests that the liquid density can be determined as: $\rho = 7.42 - 0.000395T$ (ρ in g/cm^3 and T in Kelvin). The simulations were performed at the Γ point only. The electronic-energy-convergence criterion was set to 1×10^{-4} eV/at, and the energy cutoff of 350 eV was used. Spin polarization was not considered. The total simulation time was 50 ps.

The atomic structure in the liquid state can reveal the useful information about the preferred interatomic bonding that may impact the formation of the disordered solid solution during solidification [52, 140]. The partial pair distribution function (PDF) gives the information about the probability of such bond formation by measuring the intensity of near-neighbor pairs against the total random distribution, and partial PDF ($g_{ab}(r)$) was calculated using:

$$g_{ab}(r) = \frac{V}{N_a N_b} \frac{1}{4\pi r^2} \sum_{i=1}^{N_a} \sum_{j=1}^{N_b} \left\langle \delta\left(\left|r_{ij}\right| - r\right) \right\rangle \tag{5.2}$$

where V is the volume of the supercell, N_a and N_b are the number of elements a and b, $\left|r_{ij}\right|$ is the distance between elements, a and b, and the bracket, < >, denotes the time average of different configurations.

By examining the atomic trajectory, the diffusion constants were obtained by plotting the mean square displacement (MSD) versus time using the following equation:

$$D_i = \lim_{t\to\infty} \frac{\left\langle \left| R_i(t) - R_i(0) \right|^2 \right\rangle}{6t} \tag{5.3}$$

where D_i is the self-diffusion constant of species *i*, and $R_i(t)$ and $R_i(0)$ denote the atomic positions of species *i* at time *t* and *t = 0*, respectively. The angular bracket denotes an average over all the same species. Over the total 50 ps data collection, MSD plots for the time span over 1-8 ps are linear (not shown) and hence were used to evaluate the diffusion constants.

5.2.5 Monte-Carlo (MC) simulations

A lattice gas model can describe the order-disorder phase transitions for the same and fixed lattice. In principle, sufficiently large lattices with sufficiently accurate interactions between the lattice points, can accurately describe the real phase transitions that do not involve only changes of lattice types. The serious restrictions of lattice-gas models include the effects of lattice distortion and lattice vibration. Still, such models are found to successfully predict the order-disorder phase transitions in a number of conventional and high-entropy alloys (HEAs) [2, 115, 186-189].

In this study, a lattice gas model is constructed to describe the order-disorder phase transitions in BCC lattice. We perform Metropolis Monte-Carlo (MC) simulations using the nearest-neighbor interaction model for simplicity. In the nearest-neighbor interaction model, only the atomic interactions of the nearest neighbors between atoms are considered. The interaction parameters J_{ij} is computed by

$$J_{ij} = \Delta H_{ij} / z \tag{5.4}$$

where ΔH_{ij} is the formation of energy per atom of the solute pair i, j, and z is the number of nearest-neighbor bonds *per atom*. In the BCC structure, $z = 8/2 = 4$. Although each atom has 8 nearest-neighbor bonds, two atoms share them, hence, the number has to be divided by 2. The formation energies are taken from the *Aflow* database of Curtarolo et al. [190]. The J_{ij} parameters used in this study are tabulated in Table 5.2.

Applying numbers listed in Table 5.2, we perform two Metropolis MC simulations. One is for Alloy 1 ($Al_{20}Cr_5Fe_{50}Mn_{20}Ti_5$) using 2,000 atoms with 10^7 MC steps. The other is for the $L2_1$ phase using 250 atoms with 10^6 MC steps. The results from our calculations will be elaborated in the result part.

5.3 Results

5.3.1 CALPHAD-based HTC screening results

The goal of current work is to discover and design high-performance LWHEAs for high-temperature applications. Since materials in use at elevated temperatures may reach states that are close to equilibrium, knowledge of stable phase equilibrium at fabrication and working temperatures are therefore very important. Miracle and Senkov et al. [174, 191] have explored the development of multi-principal element alloys for structural applications and have summarized a few criteria as guidelines for the design of high-temperature structural materials:

1: No first-order phase transformation in the temperature range of the application is allowed to ensure structural stability. Therefore, all phase transformations, if present, must

Table 5.2 The nearest-neighbor interaction parameters, J_{ij} , in eV.

J_{ij}	Al	Cr	Fe	Mn	Ti
Al	0	-0.0224	-0.0942	-0.0970	-0.1280
Cr	-0.0224	0	0.0210	-0.0163	-0.0043
Fe	-0.0942	0.0210	0	0.0094	-0.1181
Mn	-0.0970	-0.0163	0.0094	0	-0.0930
Ti	-0.1280	-0.0043	-0.1181	-0.0930	0

be above the operating temperature T_{use} (about $0.8T_m$, where the temperatures are in Celsius degree).

2: Good ductility and fracture toughness are required. Therefore, the microstructure must include a ductile solid-solution primary phase as the matrix and a precipitation strengthening phase that can dissolve at high temperature and then re-precipitate above T_{use} but below T_m.

Our previous research on the Al-Cr-Fe-Mn-Ti HEAs [52] reported the formation of high-density coherent $L2_1$ precipitates in a disordered BCC solid-solution matrix. Therefore, $L2_1$ phase is chosen as the target strengthening precipitate phase. The optimal molar fraction of the $L2_1$ phase is not known, so we set it to be 0.05-0.5 at the application temperature ranges. The specific criteria used for the present HTCs are:

(I) $T_m > 1{,}250$ °C and $f(BCC) = 1$ at T_m;

(II) $f(BCC) + f(L2_1) = 1$ and $0.05 < f(L2_1) < 0.5$ at $0.8T_m$;

(III) $f(BCC) + f(L2_1) = 1$ and $0.05 < f(L2_1) < 0.5$ at $0.5T_m$.

where $f(BCC)$ and $f(L2_1)$ refer to the mole fractions of the BCC phase and $L2_1$ phase, respectively. The first criterion ensures that the primary phase is disordered BCC solid

solution. The second and third criteria ensure that $L2_1$ phase is the precipitation-strengthening phase and no phase transformation in the temperature range for application ($0.5T_m < T < 0.8T_m$). The HTC results are summarized in Figure 5.1. Area 1 only meets the criterion I. Area 2 meets the criteria I and II, and Area 3 meets all three criteria. Using a step size of 5 at.% for each component at the composition range from 0 to 50 at.%, the solidification HTCs for a total of 3246 alloys are calculated using the lever-rule model. From this first-round HTC, the melting temperature (T_m) of each alloy as well as its phase stability at T_m can be obtained. Two criteria are used to screen our target alloys: T_m > 1,250 °C and single BCC phase at T_m. One third of these alloys (1,168) are found to meet the criterion (Area 1 in Fig. 1). In the second round, the 0D point HTCs are carried out for the 1,168 alloys at $0.8T_m$ and the criterion of $f(BCC) + f(L2_1) = 1$ and $0.05 < f(L2_1) < 0.5$ is as the filter. A total of 44 alloys are identified and shown as Area 2 in Fig. 1. In the third round, the 0D point HTCs are performed for these 44 alloys at $0.5T_m$ and the same criterion $(BCC) + f(L2_1) = 1$ and $0.05 < f(L2_1) < 0.5$ is used as the filter. Only eight alloys left from more than three thousand compositions after three rounds of screening. The compositions that meet all three criteria (I, II and III) are shown as Area 3 in Figure 5.1 and listed in Table 5.1.

5.3.2 Systematic experimental investigations on identified LWHEAs

Systematic experimental investigations on the identified eight LWHEAs were then carried out not only to validate the HTC predictions, but also to obtain essential data (microstructures and mechanical properties) for further alloy improvement. The synchrotron XRD patterns (Figure 5.2a) demonstrate that all the eight alloys are composed

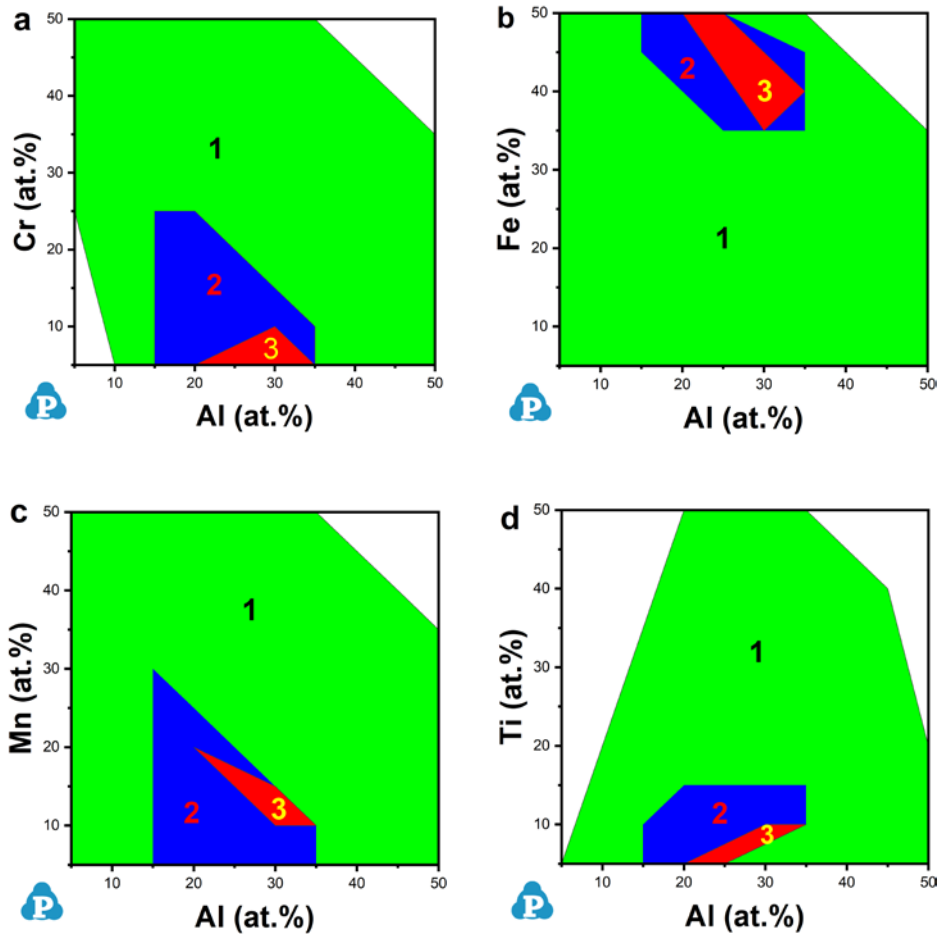


Figure 5.1 Screening optimal alloy compositions of the Al-Cr-Fe-Mn-Ti system based on the progressive criteria used in the present study. (a) Al-Cr projection, (b) Al-Fe projection, (c) Al-Mn projection, and (d) Al-Ti projection.

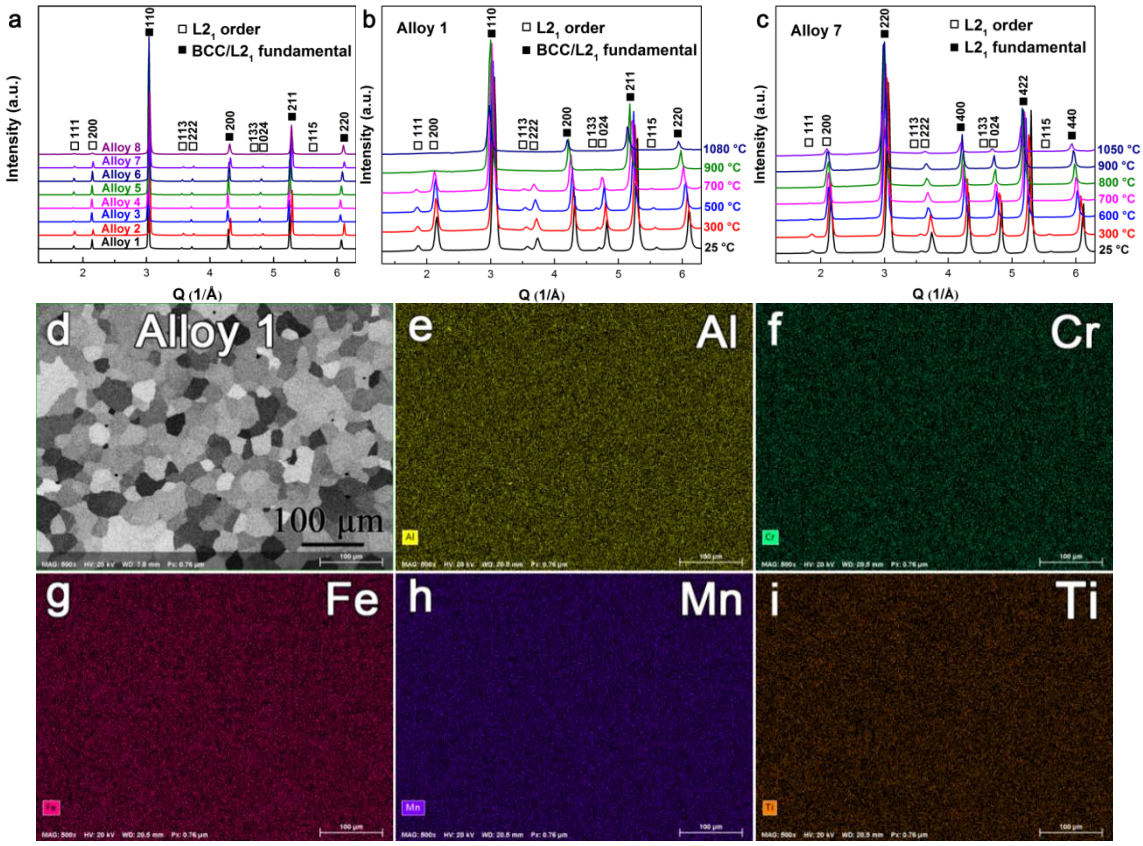


Figure 5.2 (a) Synchrotron XRD patterns of alloys 1-8, (b) and (c) In-situ neutron-scattering patterns of alloy 1 ($Al_{20}Cr_5Fe_{50}Mn_{20}Ti_5$) and alloy 7 ($Al_{30}Cr_5Fe_{50}Mn_{10}Ti_5$) (The label of order means that the reflections are exclusive to the $L2_1$ structure, while the label of fundamental means that the reflections are common to both the ordered $L2_1$ and disordered BCC structures), and (d-g) The microstructure of the as-cast alloy 1: (d) BSE image, and EDS mapping pertaining to (e-g) Al, Cr, Fe, Mn and Ti, respectively.

of $L2_1$ and possible BCC phases without other intermetallic phases, validating the reliability of our HTC predictions. Moreover, the phase stability of the $L2_1$ phase in the identified Alloy 1 ($Al_{20}Cr_5Fe_{50}Mn_{20}Ti_5$) and Alloy 7 ($Al_{30}Cr_5Fe_{50}Mn_{10}Ti_5$) is further investigated by the in-situ neutron scattering (Figures 5.2b and 5.2c). In Alloy 1, the unique $L2_1$ peaks (marked by open squares) are observed only at 900 °C and below, indicating that $L2_1$ can stabilize up to 900 °C, below which both the BCC and $L2_1$ phases coexist. The relative intensity of superstructure peaks for the $L2_1$ phase decreases with increasing the temperature, which is due to the reduced fraction of the $L2_1$ phase. In Alloy 7, the order peaks of $L2_1$ phase persist all the way to 1,050 °C, suggesting that $L2_1$ exists even up to 1,050 °C. Due to the similar crystal structure between $L2_1$ and BCC, it is difficult to distinguish BCC phase based on the diffraction results. However, the constituent phase in Alloy 7 is close to a single $L2_1$ phase, i.e., the volume fraction phase of BCC close to 0, as demonstrated by transmission-electron microscopy (TEM) and atom-probe tomography (APT) later. Figures 5.2d-5.2g show the backscattered electron (BSE) SEM microstructure image and EDS chemical mapping of Alloy 1 at the as-cast stage. The white/gray/black contrast shown in Figure 5.2d is due to the crystal-orientation difference of the grains. Figures 5.2e-5.2h indicate that all elemental components are uniformly distributed, and no distinguishable secondary phase is observed. It should be noted that the cooling rate under common conditions directly affects not the grain size but the size of a dendritic cell (dendritic parameter). Therefore, the equiaxed grains can be formed without dendritic branches (Figure 5.2d). For this case, the grain size is equal to that of the dendritic cell under identical cooling conditions and obeys the same rate dependence [192]. Such a structure is known as non-dendritic and can be formed

following a dramatic increase in the amount of nucleation centers due to dynamic action, higher undercooling, and/or the introduction of a powerful grain refiner [193]. The higher cooling rate of the drop-cast process used for alloy preparation in this work can cause higher undercooling, which may be the reason for the formation of non-dendritic equiaxed grains within the solidified alloys. For other alloys (Alloys 2-7), they all display similar BSE microstructures with Alloy 1 (Figure 5.3)

In order to reveal the morphology of $L2_1$ phase, the TEM was performed on selected representative alloys. From the dark-field (DF) image (Figure 5.4a), the high-density nano-scaled $L2_1$ precipitate (~ 20 nm) formed and uniformly distributed within the as-cast Alloy 1. The selected area diffraction patterns (SADPs) along the zone-axis of [100] and [110] further confirm the coexistence of the BCC matrix and $L2_1$ precipitate. $L2_1$ in the form of precipitates is also found in Alloy 8 (Figure 5.4f). However, unlike the precipitation morphology in Alloys 1 and 8, the $L2_1$ phase in Alloys 2, 3, 4, and 7, however, in the form of the antiphase domain (APD) separating by antiphase domain boundary (APB) (Figures 5.4b-4e).

The chemical compositions and morphologies of the constituent phase in Alloys 1, 2 and 7 are determined by APT (Figure 5.5). In Alloy 1, one can notice that the $L2_1$ phase is rich in Al and Ti, while the BCC phase is segregated in Cr, Mn, and Fe. Similar compositional distribution in the $L2_1$ and BCC phases is also observed in Alloy 8. The detailed chemical compositions of constituent phases are given in Table 5.3. Moreover, the $L2_1$ number density of 2.76×10^{22} /m^3 and volume fraction of 43.64% in Alloy 1 were also determined by APT analysis, close to the volume fraction of ~ 44%, determined by

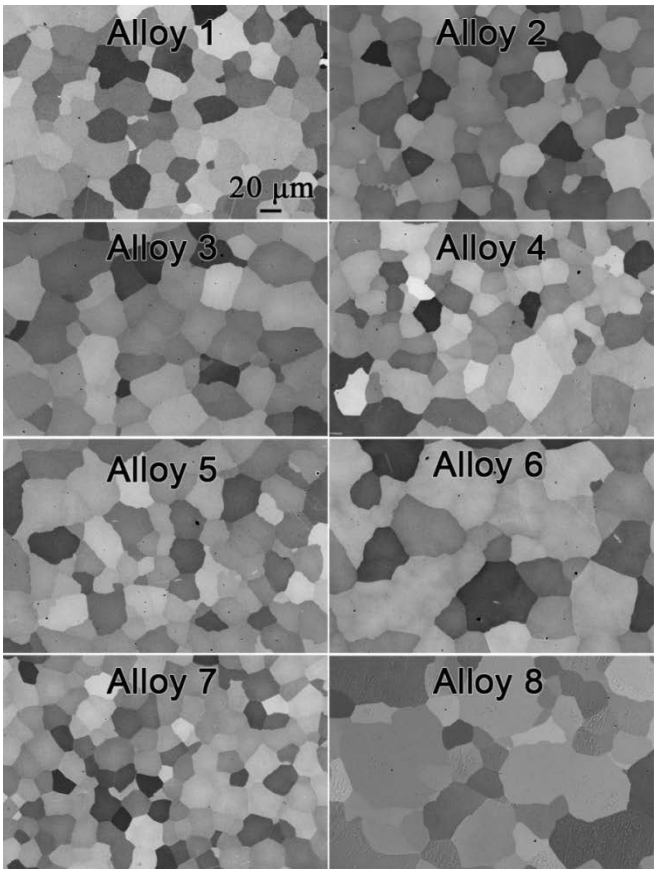


Figure 5.3 BSE images of Alloys 1-8.

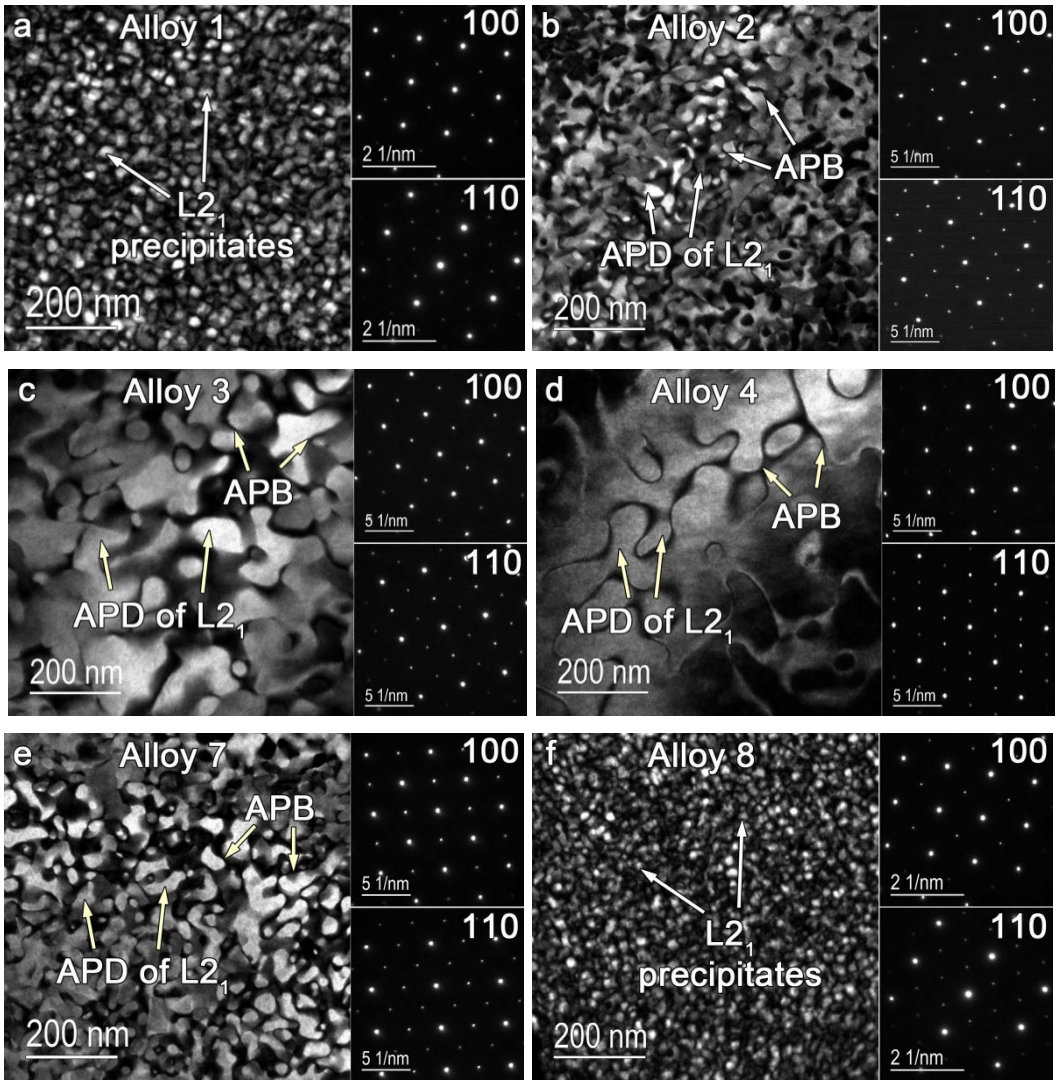


Figure 5.4 TEM characterizations of selected representative alloys. (a-f) DF images of Alloys 1 ($Al_{20}Cr_5Fe_{50}Mn_{20}Ti_5$), 2 ($Al_{25}Cr_5Fe_{50}Mn_{15}Ti_5$), 3 ($Al_{35}Cr_5Fe_{40}Mn_{10}Ti_{10}$), 4 ($Al_{30}Cr_{10}Fe_{35}Mn_{15}Ti_{10}$), 7 ($Al_{30}Cr_5Fe_{50}Mn_{10}Ti_5$), and 8 ($Al_{16}Cr_5Fe_{50}Mn_{24}Ti_5$) taken by the unique (111) reflection of $L2_1$ phase and corresponding SADPs in the [100] and [110] zone axis, respectively.

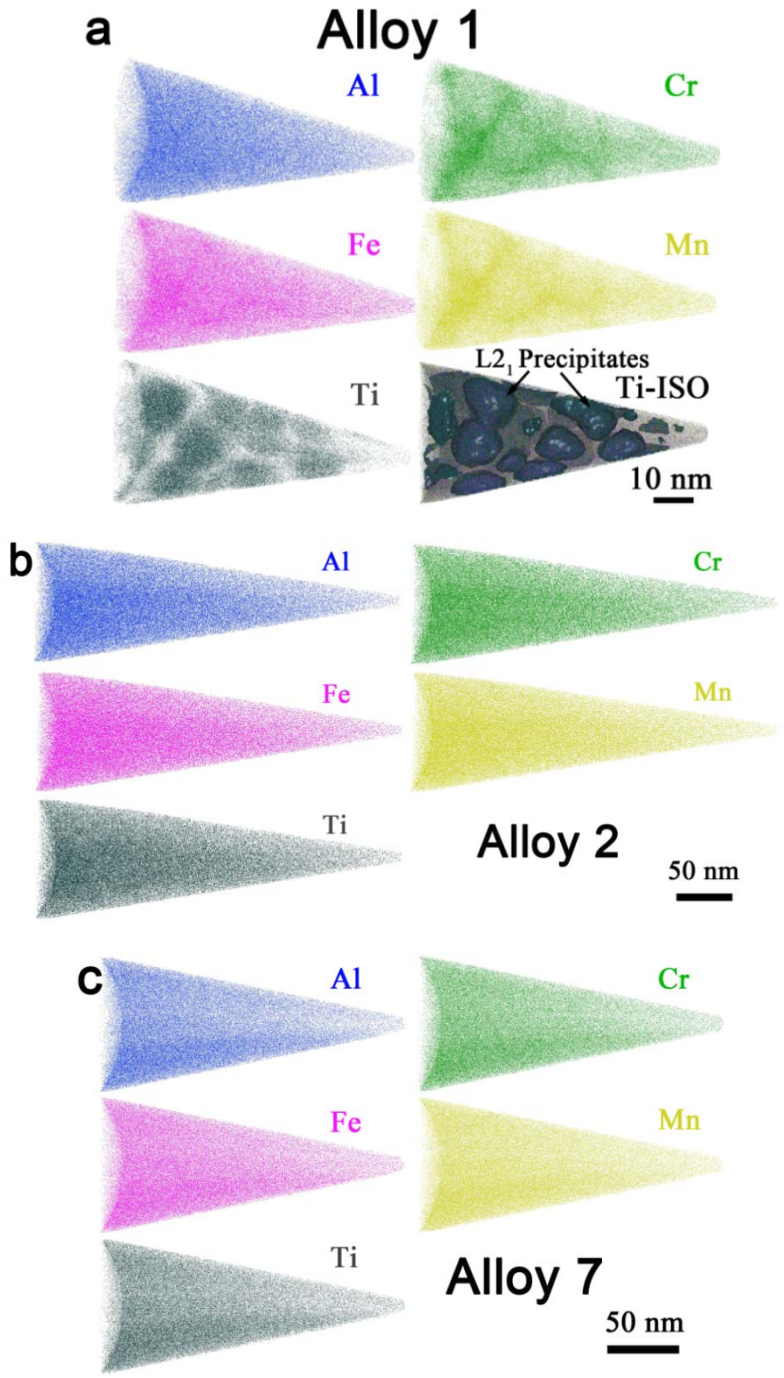


Figure 5.5 APT characterizations of selected representative alloys. (a-c) elemental distributions of Alloys 1, 2, and 7, respectively.

Table 5.3 APT measured chemical compositions of the BCC and $L2_1$ phases in the Alloys 1 and 8.

Alloy 1					
Phase	Al (at. %)	Cr (at. %)	Fe (at. %)	Mn (at. %)	Ti (at. %)
BCC	16.63 ± 0.09	6.70 ± 0.05	53.10 ± 0.10	22.79 ± 0.09	0.79 ± 0.02
$L2_1$	23.67 ± 0.14	3.21 ± 0.06	49.82 ± 0.14	11.84 ± 0.11	11.46 ± 0.10
Alloy 8					
Phase	Al (at. %)	Cr (at. %)	Fe (at. %)	Mn (at. %)	Ti (at. %)
BCC	13.31 ± 0.04	6.04 ± 0.01	53.09 ± 0.05	26.35 ± 0.04	1.21 ± 0.01
$L2_1$	22.14 ± 0.09	2.62 ± 0.02	49.49 ± 0.10	10.40 ± 0.06	15.32 ± 0.07

the Rietveld refinement (Figure 5.6). Note that the number density is underestimated since precipitates are touching or overlapping so that they cannot be delineated from each other using isosurfaces. In contrast to Alloy 1, the chemical distributions of constituent elements in Alloys 2 and 7 are uniform (Figure 5.5). Together with the TEM observations, it suggests that Alloys 2 and 7 are composed of a single $L2_1$ phase rather than BCC and $L2_1$ two phases.

In order to high-throughput evaluate the mechanical properties of the identified eight alloys, compression tests were performed on the eight alloys at room temperature (RT) (Figure 5.7a). One can see that the yield strengths of these alloys vary in a wide range from 517 to 1,627 MPa. Detailed mechanical properties of these alloys are listed in Table S3. The reason for this variation will be explained in the discussion section. The high-temperature performances of Alloys 1 and 8 are also demonstrated, which are compared with other representative materials, as shown in Figures 5.7b and 5.7c. Alloys 1 and 8 both exhibit very high yield strength below 700 °C, as evidenced by 1,484 MPa at RT and 1,073 MPa at 500 °C for Alloy 1 and 1,627 MPa at RT and 625 MPa at 500 °C for Alloy 8.As the temperature increases to 700 °C, the yield strengths of Alloys 1 and 8 are still kept at 586 MPa and 625 MPa, respectively, though an obvious softening occurs like many other precipitation-strengthened BCC alloys [116, 194-197]. More importantly, compared with other traditional precipitation-strengthened BCC alloys, including BCC + $L2_1$, BCC + $D0_3$, and BCC + B2, the newly-designed $L2_1$ precipitation-strengthened LWHEAs show outperforming yield strength and specific yield strength, suggesting the

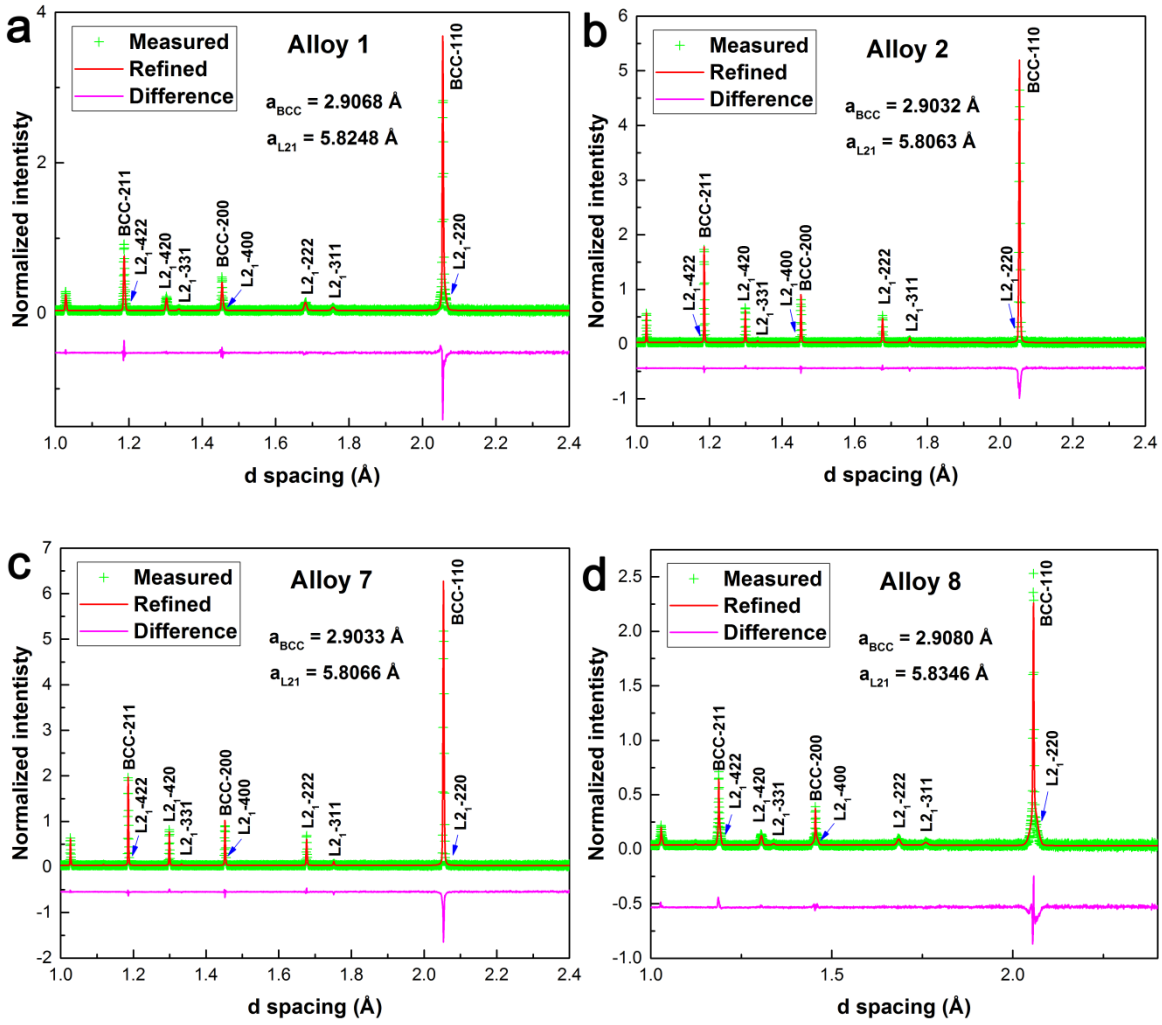


Figure 5.6 (a-d) GSAS Rietveld refinements on the neutron diffraction results of Alloys 1, 2, 7, and 8 at RT, respectively. During the refinements, Alloys 2 and 7 are also treated as BCC + $L2_1$ two-phase structure, and then we obtain the lattice misfits of Alloy 1 (0.192%), Alloy 2 (-0.002%), Alloy 7 (0.001%), and Alloy 8 (0.319%). The pretty small lattice misfits of Alloys 2 and 7 also indicate that these two alloys have a single-phase $L2_1$ structure rather than two-phase BCC and $L2_1$ structures.

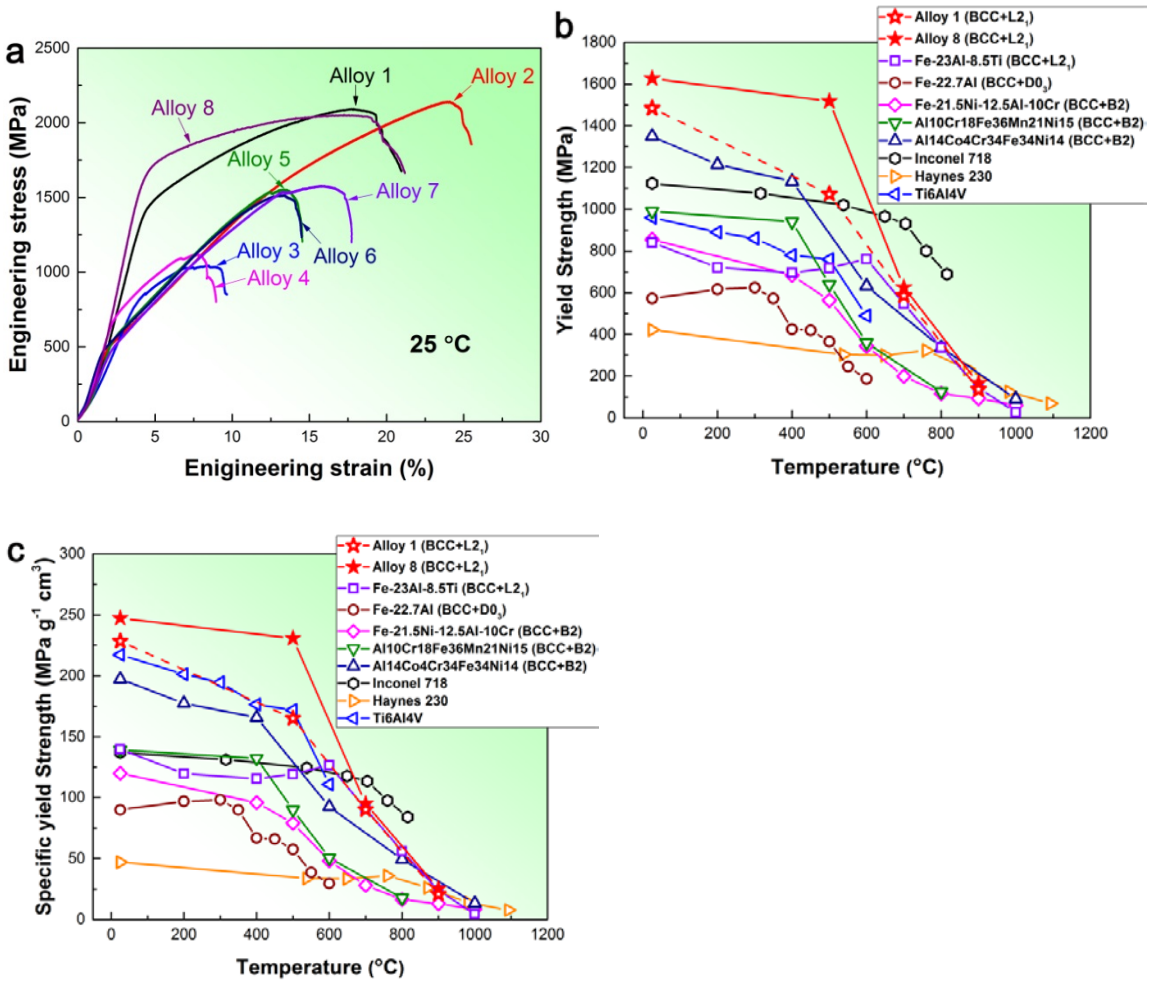


Figure 5.7 (a) Compressive stress-strain plots of Alloys 1-8 at RT, (b) and (c) Comparison of yield strength and specific yield strength as a function of temperatures between Alloys 1, 8 and other materials, respectively [116, 194-197].

rational alloy-design strategy for developing lightweight precipitation-strengthened BCC alloys by HEA concept.

5.3.3 Theoretical simulations via AIMD and MC

In order to understand the formation reason of the $L2_1$ phase, theoretical AIMD and MC simulations were performed. Figures 5.8a-e shows the select partial pair-distribution function (PDF) of Alloy 1 ($Al_{20}Cr_5Fe_{50}Mn_{20}Ti_5$) at T = 1,600 °C to the first nearest neighbor. The TiTi pair correlation, which has the largest bond length, has the lowest intensity and is significantly lower than the other pair correlation, indicating the strong tendency for Ti atoms to form bonds with other elements. On the other hand, the AlFe pair correlation has the highest intensity, and all other pair correlations seem to be very comparable in intensity. The distribution of these pair correlations is consistent for all four temperatures at which the present AIMD was carried out. Prior AIMD simulations of $Al_{1.5}$CrFeMnTi also show the strongest AlFe pair correlation [52]. The persistent presence of stronger AlFe pair correlation regardless of the Al or Fe contents in the Al-Cr-Fe-Mn-Ti alloys suggest that AlFe pair interaction may play a more important role in the mechanical properties for this HEA system. Nonetheless, the short-range order in the Al-Cr-Fe-Mn-Ti system is not strong in the liquid, if one compares it with liquid structures of CuNiPdPtP [3, 139] and $Al_{1.3}$CoCrCuFeNi HEA [115].

The diffusion constants determined from the mean square displacement plots are shown in Figure 5.8f as a function of temperature. The magnitude of the diffusion constants of the elements basically follows their atomic sizes: Large atoms diffuse slower than smaller atoms. A Ti atom has the largest radius among these five elements, followed

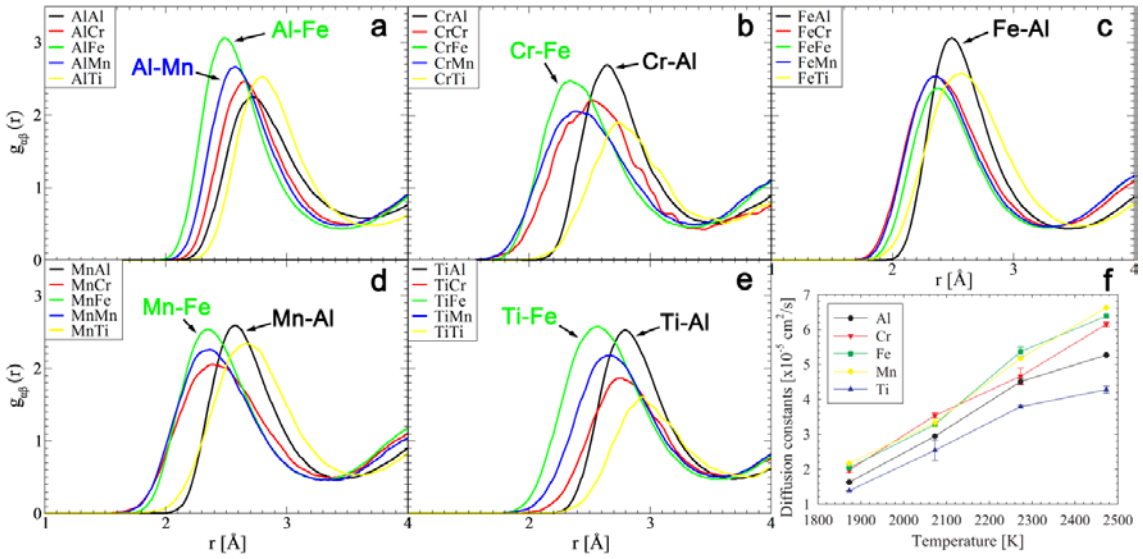


Figure 5.8 (a-e) AIMD simulated partial PDFs of Alloy 1 ($Al_{20}Cr_5Fe_{50}Mn_{20}Ti_5$) at T = 1,600 °C, and f simulated diffusion constants of the constituent elements at selected temperatures.

by Al, while Cr, Fe and Mn atoms have very similar atomic radii. At all four temperatures, Ti has the slowest diffusivity followed by Al. The diffusion constants for Cr, Fe, and Mn are largely equivalent within the uncertainty range.

The present AIMD simulation indicates that Al and Ti promote short-range order in this Al-Cr-Fe-Mn-Ti system, and therefore, their additions impact greatly (1) the formation of single-phase BCC solid solution, and (2) atomic bond strength. Indeed, the formation of BCC and $L2_1$ compounds were reported in $Al_{1.5}$CrFeMnTi, and the microstructure of extremely-fine $L2_1$ precipitates (~ 4 nm) with high density embedded in and coherent with the BCC matrix is very attractive for high-temperature applications [52].

The AIMD simulations provide us qualitative information on the ordering degree at molten state, illustrating the formation reason of $L2_1$ phase. However, in order to understand the different $L2_1$ morphology of these identified eight alloys. The order-disorder transition during solidification needs to be understood. Therefore, Metropolis MC calculations were also performed with much larger supercells of 2,000 atoms within the nearest neighbor interaction approximation. With the concentrations as only variables, this method gives a more clear and definitive picture of the influence of constitutions on the order-disorder transition. As examples, MC calculations for Alloys 1 and 7 using 10^7 MC steps were performed. The output of the MC calculations allows us to calculate the short-range ordering (SRO) and long-range ordering (LRO) parameters for Both Alloys 1 and 7 between 0-2,500K. The LRO can be expressed as [198]

$$\eta_i = \frac{y_i^{\alpha} - y_i^{\beta}}{y_i^{\alpha} + y_i^{\beta}} \tag{5.5}$$

where y_i^{α} and y_i^{β} are the fractional occupancy of element i on sublattice α and β, respectively. The value of η_i falls within the range of -1 to 1, as shown in Figures 5.9a and 5.9b. When η_i is 0, it means that element i is equally found on both α and β sublattice. When η_i equals 1 or -1, it indicates that element i can be exclusively found on the α or β sublattice.

The order-disorder-transition behavior can be directly reflected by the LRO parameters (Figure 5.9a and 5.9b). In both Alloys 1 and 7, as the temperature decreases, Al, Cr, and Ti tend to segregate to one sublattice, with Fe and Mn primarily occupying another sublattice. Moreover, as the temperature decreases, the ordering process in Alloy 1 proceeds slowly, unlike the case in Alloy 7 where the ordering process proceeds quickly, implying a possible precipitation process occurs in Alloy 1. As indicated by the red arrows, the ordering temperature, T_c, in Alloy 1 (~ 1,880K) is much lower than that in Alloy 7 (~ 2,270K, far beyond its melting temperature), suggesting that disordered BCC phase is easier retained in the solid state in Alloy 1 than in Alloy 7 [186]. This prediction is consistent with our experimental observations (Figures 5.4a and 5.4e), i.e., Alloy 1 is composed of $L2_1$ and disorder BCC phase from RT to 1,173 K, while only the ordered $L2_1$ phase still exists in Alloy 7 from RT to 1,323K. The inset subfigures give the snapshots at 100K which directly show the $L2_1$ phase formation. Besides the LRO, the SRO parameters reveal more details of the order-disorder transition behavior (Figures 5.9c and 5.9d). Since Fe is the most abundant element in this system (50 at. %), we consider its changes as the fingerprint of the ordering transition. In both alloys, the temperature-dependent SRO parameters show us that Fe atoms as the nearest neighbors of Al and Ti increase with

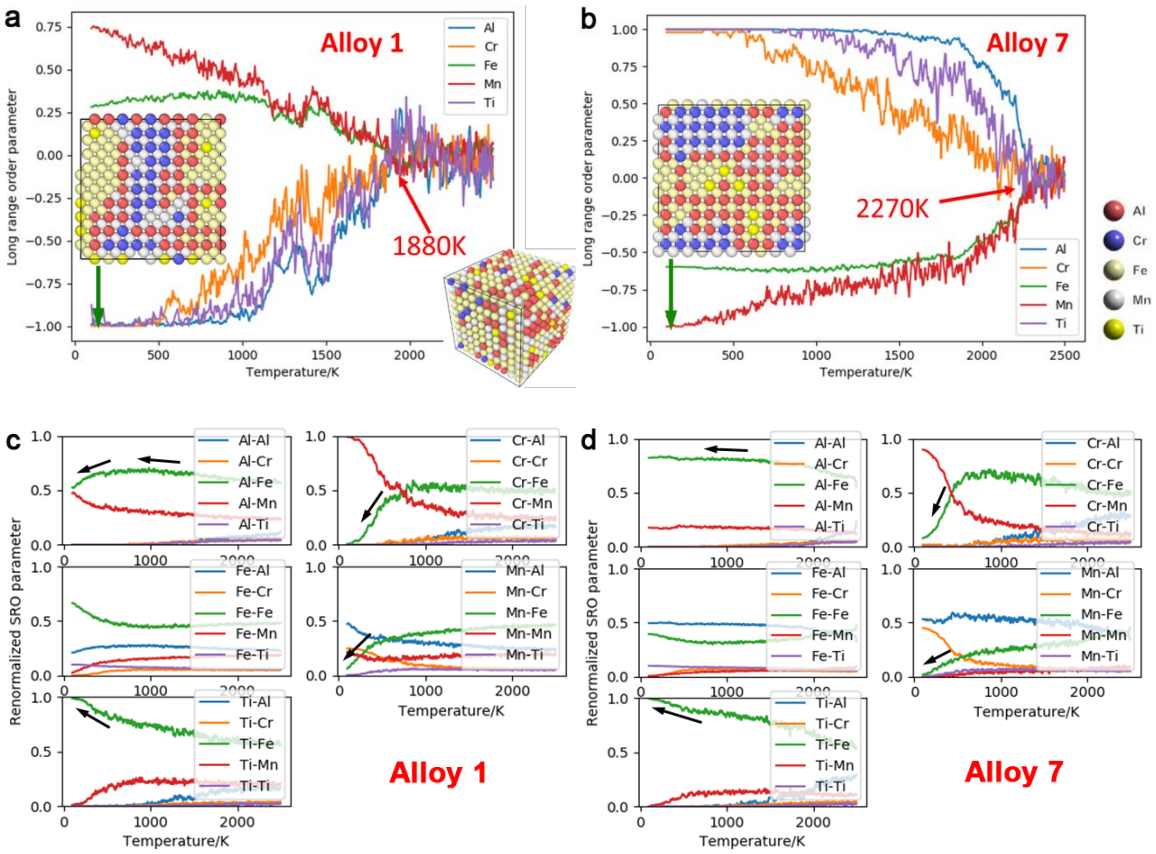


Figure 5.9 (a) and (b) The LRO parameters as a function of temperature in Alloys 1 ($Al_{20}Cr_5Fe_{50}Mn_{20}Ti_5$) and 7 ($Al_{30}Cr_5Fe_{50}Mn_{10}Ti_5$), respectively. (c) and (d) The SRO parameters as a function of temperature in Alloys 1 and 7, respectively. The black arrows indicate the change of the most abundant Fe as neighbor of all elements.

decreasing the temperature, agreeing with the AIMD simulated partial PDFs (Figure 5.8), while that of the Cr and Mn have the opposite trend (Figures 5.9c and 5.9d). This trend is particularly obvious for Ti that has only Fe as its neighbors around and below 1,000K. Moreover, the SRO results further demonstrate that the formation of $L2_1$ phase is favored by Fe-Al and Fe-Ti pairs and the formation of BCC phase formation favored by Cr-Cr and Mn-Mn pairs, in agreement with the chemical compositions of $L2_1$ and BCC phases (Figure 5.5a and Table 5.3). The MC-calculated 2,000-atom superstructures for both Alloys 1 and 7 are further verified by the neutron-scattering determined PDF results. As shown in Figures 5.12, the superstructures were used for the PDF fittings, and PDFs of Alloys 1 and 7 are fitted well using the calculated superstructure.

In order to better show the ordering transition due to the formation of the Fe_2AlTi-type $L2_1$ phase, we perform another MC simulation with 250 atoms and 10^6 MC steps especially for this system between 0-3,000 K (Figures 5.10 and 5.11). The ordered $L2_1$ structure starts to become less ordered at ~ 1,500 K. Both the LRO and SRO disappear at about 2,600 K. Through comparing the LRO and SRO between Fe_2AlTi-type $L2_1$ and Alloys 1 and 7, we can find that the ordering temperature in Alloy 7 with a higher Al content is closer to that of Fe_2AlTi-type $L2_1$ structure, suggesting that Alloy 7 is more like the Fe_2AlTi-type $L2_1$.

5.4 Discussions

The concept of HEA provides us an unprecedented degree of freedom in the design of advanced alloys with promising properties. For the rapid exploration of the vast compositional space and investigation of the composition and temperature effects on the

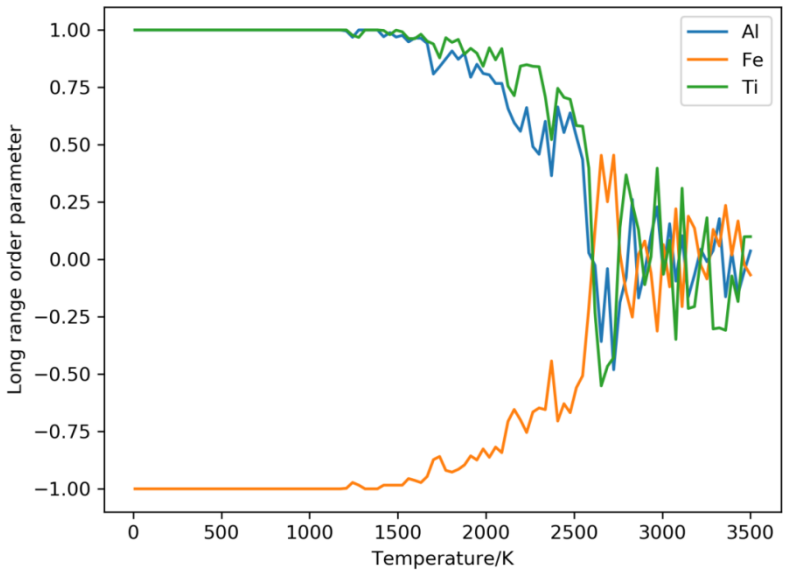


Figure 5.10 LRO parameters of the Fe_2AlTi of $L2_1$ structure.

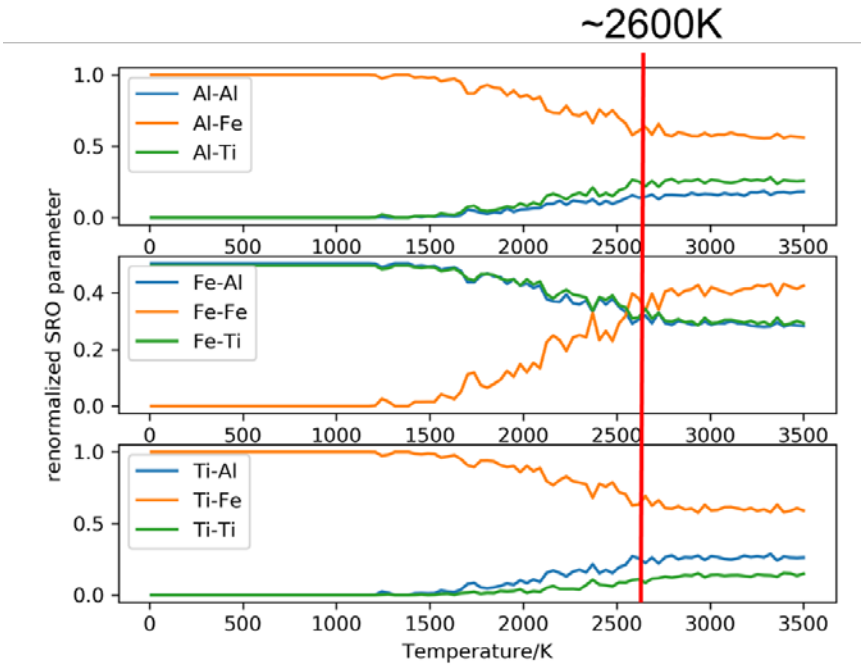


Figure 5.11 The first six SRO parameters of the Fe_2AlTi of $L2_1$ structure. Above ~2600K, all the renormalized SRO parameters approach the concentration fractions of random state.

microstructure, advanced HEA-design strategies and efficient tools are necessary. At present, a few advanced HEA-design strategies were reported by combining physicochemical criteria, CALPHAD, data mining, and multi-objective optimization algorithm [174, 199], [191, 200], [201], [202]. As is shown by these publications, the CALPHAD method has played an important role in the design of advanced HEAs. As mentioned previously, the accuracy and efficiency of the CALPHAD method depends on the reliability of the used thermodynamic database the computational software, respectively. It should point out that the slight difference in the computational efficiency could be significant for HTC since massive calculations are carried out. Using the explored composition space of this work as an example, in the studied temperature range, each element of the Al-Cr-Fe-Mn-Ti quinary system varies at 0 ~ 50 at.%. It is easy to understand that the smaller composition step size for HTC can better represent/cover the phase equilibria within this specified compositional space. Yet, a smaller step size will significantly increase the number of compositions for HTC within the same specified compositional space, which is time-consuming. Within the compositional space specified in this study (the number of components = 5), the total number of alloys for HTC with the composition step size of 5 at. % is about 3×10^3. While it increases to about 2×10^6 when using the step size of 1 at. %. Using the modern personal computer core and Pandat^{TM} software [170, 203], it takes a few hundreds of milliseconds for a single equilibrium (0D) calculation and several seconds for a 1D equilibrium calculation within this quinary system. This is roughly estimated and the actual computing time will vary with the complexity of each calculation. It takes a few hours for us to finish the HTCs (~ 3×10^3)

in the current work. If we choose the step size of 1 at.% for this quinary system, the computational time will easily increase to a few thousands of hours, which will be very challenging for the computational resource of a single personal computer. For a higher-order system (the number of components > 5), the consumption of the computational resource will be even more. Fortunately, the current HTC module can be easily converted to parallel calculations for efficiently utilizing the available computational resource, which is the target that we are working on. On the other hand, the CALPHAD-developed datasets are multi-dimensional and very large. Thus, the organization of the large volume of data will be especially critical for efficiently retrieving the requested subsets of the large datasets. At present, each calculation is stored separately in a workspace and organized by its calculation ID. The calculation ID is usually the alloy composition, and the detailed information of each calculation is represented by the predefined features, such as the composition, temperature, phase fraction etc. Note that we can generally include all kinds of thermochemical and thermophysical properties in an individual CALPHAD calculation, when there are applicable databases. The users can easily access these CALPHAD calculated results via their calculation IDs and efficiently retrieve the requested datasets through the customized features. Here, we would like to emphasize that any algorithms that are able to be ascribed to these features can be employed as the screening criteria for the CALPHAD calculated datasets. Moreover, our current HTC tool allows users to customize the outputs of different types of CALPHAD calculations for the possible combination with other datasets for machine learning and the usage of other data mining tools.

The AIMD and MC simulations provide insights into the formation of the $L2_1$ phase and the order-disorder-transition behavior. The SRO of Fe-Al and Fe-Ti can be the embryo for the formation of the Fe_2AlTi-type $L2_1$ phase during solidification, similar to our previous work [52]. Thus, the morphology of the $L2_1$ phase can play a crucial role in determining the mechanical performance of these alloys, particularly, considering the similar micro-scaled features (e.g., grain size) among the eight alloys (Figure 5.3). In the Alloy 1 ($Al_{20}Cr_5Fe_{50}Mn_{20}Ti_5$), coherent nanoscaled $L2_1$ precipitates are observed (Figures 5.4a and 5.5a). Thus, the high strength of Alloy 1 is attributed to its remarkable precipitation strengthening effect. As known, the precipitation strengthening can be divided into two categories, particle shearing or Orowan bowing. In consideration of the observed pretty small nanosized coherent $L2_1$ particles (~ 20 nm) from both TEM and APT, it is more likely that the shearing mechanism dominates the strengthening. For the coherent precipitation, coherency strengthening, $\Delta\sigma_{CS}$, modulus mismatch strengthening, $\Delta\sigma_{MS}$, and order strengthening, $\Delta\sigma_{OS}$, contribute to the increase in the yield strength, which can be expressed as follows, respectively [62]:

$$\Delta\sigma_{CS} = M \cdot \alpha_{\varepsilon} \left(G\varepsilon_c\right)^{3/2} \left(\frac{rf}{0.5Gb}\right)^{1/2} \tag{5.6}$$

$$\Delta\sigma_{MS} = M \cdot 0.0055\left(\Delta G\right)^{3/2} \left(\frac{2f}{G}\right)^{1/2} \left(\frac{r}{b}\right)^{3m/2-1} \tag{5.7}$$

$$\Delta\sigma_{OS} = M \cdot 0.81 \frac{\gamma_{apb}}{2b} \left(\frac{3\pi f}{8}\right)^{1/2} \tag{5.8}$$

where M is the Taylor factor, which equals 2.75 for the BCC structure and 3.06 for the FCC structure [204], α_ε = 2.6 (a constant) [205, 206], $\varepsilon_c = 2/3(\Delta a/a)$ [205-207] is the

constrained lattice misfit, where $\Delta a/a \approx 0.19\%$ determined from the Rietveld refinement on the high-resolution neutron diffraction results (Figure 5.6a). G and ΔG are the shear modulus of the matrix and the shear modulus mismatch between precipitates and matrix, respectively (G = 83GPa, $\Delta G \approx 0$, obtained from the Kroner model[208] elastic-fitting results on the in-situ neutron diffraction data during compression). r is the average particle size (r ≈ 20 nm). γ_{apb} is the antiphase boundary energy of the precipitates ($\gamma_{apb} \approx 27 \times 10^{-2}$ J/m^2) [209]; b is the Burgers vector (2.5174 Å); f is the volume fraction of the precipitates ($f \approx 0.44$, obtained from the Rietveld refinement on the high-resolution neutron diffraction results, Figure 5.6a).

Substituting all the parameters into Eqs. (2-4), the strengthening contributions from coherency strengthening, $\Delta\sigma_{CS}$, modulus mismatch strengthening, $\Delta\sigma_{MS}$, and order strengthening, $\Delta\sigma_{OS}$, are roughly determined to be ~ 224 MPa, ~ 0 MPa, and ~ 859 MPa. Since the larger one of $\Delta\sigma_{CS} + \Delta\sigma_{MS}$ and $\Delta\sigma_{OS}$ determines the resultant these sequential process, the precipitation strengthening is mainly attributed to the ordering strengthening (859 MPa), which is close to the experimentally-determined strength difference (960 MPa) between Alloy 1 and Alloys 2 and 7. Thus, we can conclude that the high strengths of Alloys 1 and 8 are attributed to coherent precipitation strengthening. In contrast, the absence of coherent precipitation strengthening in other Alloys 2-7 is the main reason that leads to their low yield strengths. This conclusion is further demonstrated by the neutron scattering results. Figures 5.12c and 5.12d exhibit the lattice strain versus applied compressive stress along the loading direction in both Alloys 1 and 7. One can notice that Alloy 1 displays remarkable load transfer behavior upon BCC yielding (above 1,200 MPa),

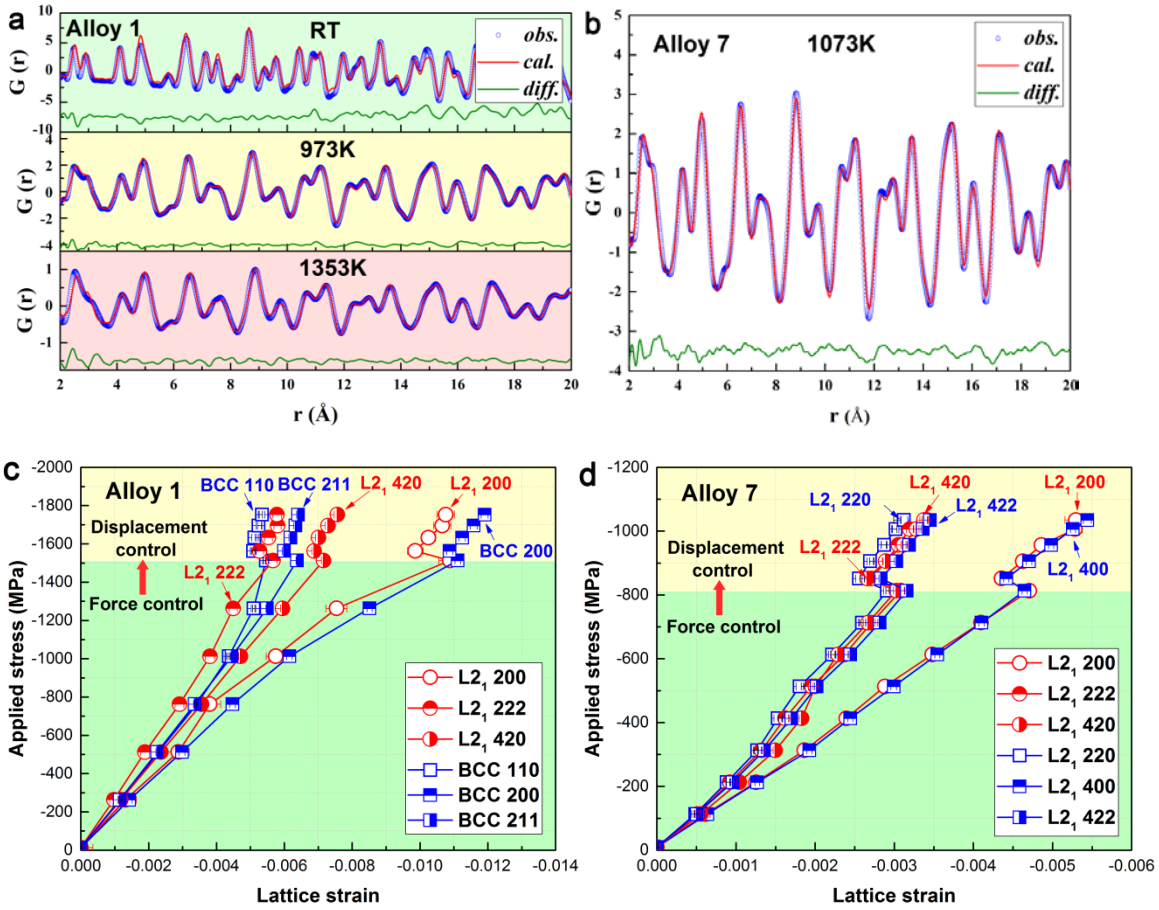


Figure 5.12 (a) and (b) Pair-distribution functions (PDFs) of the Alloys 1, 2, and 7 at RT measured by neutron total scattering method. (c) and (d) lattice strain as a function of applied stress along loading direction in Alloy 1 and Alloy 7 at RT, respectively.

i.e., the hard $L2_1$ phase bears larger load with larger lattice strains ($L2_1$ 222 and $L2_1$ 420) and the soft BCC phase undertakes lower load with lower strain lattices (BCC 110 and BCC 211), which is a reflection of the precipitation strengthening. By contrary, no load transfer is found in Alloy 7. The unchanged response of lattice strain versus applied stress in Fig. 5.12b suggests that Alloy 7 behaves as a single $L2_1$ phase, as demonstrated by TEM and APT (Figure 5.4e and Figure 5.5c). Note that a sudden lattice-strain jump occurs due to the change of loading mode from force control to displacement causing the relaxation of lattice strain.

The different morphologies exhibited between Alloys 1, 8 and Alloys 2-7 are strongly correlated to their different chemical compositions (Table 5.1), because the different chemical compositions directly affect the order-disorder transition behavior, namely, atomic occupancies of constituent elements. According to the calculated LRO/SRO (Figure 5.9) and AIMD (Figures 5.8a-e), Fe-Al, Fe-Ti, and Cr-Mn are the preferable pairs. Moreover, Mn-Al and Mn-Ti also have comparable interaction energies with Fe-Al and Fe-Ti (Table 5.2), suggesting Fe can be replaced by Mn in some sense. Thus, according to the different contents of Al, Fe, and Mn, here we categorize the eight alloys into two groups:

(I) Group 1 (Al < 25 at.%, Fe = 50 at.%, and Mn > 15 at.%): Alloys 1 ($Al_{20}Cr_5Fe_{50}Mn_{20}Ti_5$) and 8 ($Al_{16}Cr_5Fe_{50}Mn_{24}Ti_5$);

(II) Group 2 (Al $\geqslant$ 25 at.%, Fe $\leqslant$ 50 at.%, and Mn $\leqslant$ 15 at.%): Alloys 2 ($Al_{25}Cr_5Fe_{50}Mn_{15}Ti_5$), Alloys 3 ($Al_{35}Cr_5Fe_{40}Mn_{10}Ti_{10}$), 4 ($Al_{30}Cr_{10}Fe_{35}Mn_{15}Ti_{10}$), 5 ($Al_{30}Cr_5Fe_{40}Mn_{15}Ti_{10}$), 6 ($Al_{30}Cr_5Fe_{45}Mn_{10}Ti_{10}$), and 7 ($Al_{30}Cr_5Fe_{50}Mn_{10}Ti_5$).

According to the experimental observations, Group 1 (Alloys 1 and 8) forms the nanoscaled $L2_1$ precipitates within the BCC matrix, while Groups 2 (Alloys 2 - 7) have the single $L2_1$ phase in the form of APD. To probe the reason causing the different $L2_1$ morphologies, the atomic site occupancies of the formed $L2_1$ structure will be revealed as follows, based on the observed TEM, APT, and calculated LRO and SRO. As shown in Figure 5.13, $L2_1$ (X_2YZ) (Prototype, Fe_2AlTi; Pearson type, cF16) has three different sublattice sites: X @ 8c(1/4, 1/4, 1/4), Y @ 4a(0, 0, 0), Z @ 4b(1/2, 1/2, 1/2). According to the calculated LRO parameters (Figure 5.9), Fe and Mn prefer to one sublattice, while Al, Ti, and Cr tend to segregate into another sublattice. In the $L2_1$ structure, the sublattices of Y and Z can be considered equally in terms of site, but differently in terms of composition. That is why $L2_1$ can be considered an ordered 2 × 2 × 2 supercell of B2 structure. Taking account of the strong atomic pairs of Fe-Al, Fe-Ti, Fe-Cr, and Ti-Al, we can assert that Y(4a) and Z(4b) are filled with Al and (Ti, Cr), respectively. Note if the content of Al is more than 25 at.%, the extra Al atoms can also occupy the site of Z(4b). In the $L2_1$ structure of present Al-Cr-Fe-Mn-Ti system, Fe atoms are always in the site of X(8c) because the content of Fe is not beyond 50 at.%. As for Mn, its site occupancy depends on Fe's contents, that is, if Fe content is less than 50 at.%, Mn can occupy the unfilled sites of X(8c) by Fe because Mn-Al and Mn-Ti have comparable interaction energies with Fe-Al and Fe-Ti. However, once Fe's content equal to 50 at.%, the sites of

X(8c) are completely by Fe atoms, and thus, Mn can occupy the unfilled sites at Z(4b) by Ti and Cr. Similar atomic occupancy of Mn at Z(4b) can be found in a Fe_2AlMn $L2_1$ structure [210]. Note the solubility of Mn at sites of Z(4b) should not exceed 15 at.% because Mn content in $L2_1$ is always less than 15 at.% (Tables 5.1 and 5.3). Upon the content of Mn is more than 15 at.%, the extra Mn goes to the BCC matrix. Due to the strong atomic pair of Mn-Cr (Figure 5.9c), Cr tends to segregate with Mn together in the disordered BCC matrix, as evidenced by the observed Cr and Mn-rich BCC matrix in Alloys 1 and 8 (Figures 5.5a and Table 5.3). To clearly summarize the phase evolution behavior in the present alloy system, a schematic flowchart is plotted in Figure 5.13, in which the atomic site occupancies and $L2_1$ precipitations/APD formation rules are integrated. When a designed alloy meets the criterion of Al is less than 25 at.% or Mn is more than 15 at.%, the $L2_1$ phase is in the form of nanoscaled precipitates-strengthened within the BCC matrix, like Alloys 1 and 8 (Group 1). On the contrary, if a designed alloy cannot meet this criterion, the $L2_1$ phase has the APD morphology, such as Alloys 2-7 (Groups 2). Based on the known atomic site occupancies, the different $L2_1$ morphologies between Alloys 1, 8 and Alloys 2-7 can be easily understood from $L2_1$'s stoichiometric composition, $(50)^{X}_{Fe(Mn)}(25)^{Y}_{Al}(25)^{Z}_{Ti,Cr(Al,Mn)}$. For Alloys 2-7, their chemical compositions can exactly match the perfect $L2_1$ stoichiometry, resulting in the formation of single-phase $L2_1$ phase, which is in form of APD separated by APB (Figures 5.4b-e). In contrast, for Alloys 1 and 8, their chemical compositions are deviated from the perfect $L2_1$ stoichiometry, leading to the formation of nanoscaled $L2_1$ precipitates (Figure 5.4a and 5.4f).

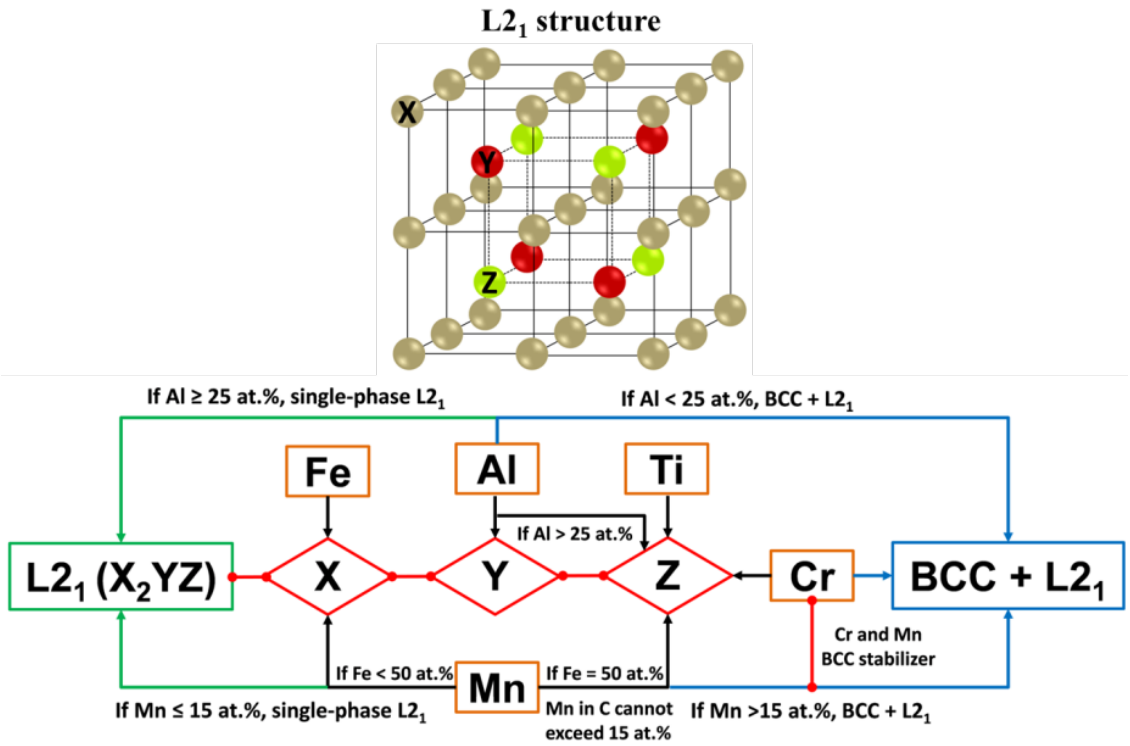


Figure 5.13 A flowchart that shows the atomic occupancies of Al, Cr, Fe, Mn, and Ti on the sublattice sites of X, Y, and Z in the $L2_1$ (X_2YZ) structure and the $L2_1$ precipitates/APD evolution rules based on the eight designed LWHEAs.

The integrated experimental and theoretical studies on the discovered LWHEAs demonstrate the sensitivity of the nanoscaled $L2_1$ precipitates-strengthened BCC microstructure to alloys' chemical compositions. Therefore, the extra scrutiny of the alloys' chemical compositions that are related to critical ordering temperature, lattice misfit, and morphology of $L2_1$ precipitates is required. Moreover, there is no escaping the fact that the present CALPHAD-based high-throughput prediction still not realizes 100% accuracy, i.e., only two alloys meet our expectation. One main reason is that the present thermodynamic database in the Al-Cr-Fe-Mn-Ti multi-component system is not perfect yet, which is caused by the limited phase-diagram studies so far. Thus, in the future, more systematical works on establishing more reliable CALPHAD database are indispensable. However, even so, the CALPHAD-based HTCM does help us efficiently screen out a series of LWHEAs from thousands of compositions, which greatly accelerates the design of precipitation-strengthened BCC LWHEAs.

5.5 Conclusions

In summary, here a series of lightweight and low-cost Al-Cr-Fe-Mn-Ti HEAs were high-throughput discovered and systematically investigated, utilizing the integrated CALPHAD-based HTC tool, theoretical calculations, and focused experiments. Two discovered $L2_1$ precipitates-strengthened BCC LWHEAs exhibit superior precipitation strengthening to other traditional precipitation-strengthened BCC alloys. The present high-throughput design and study of LWHEAs will accelerate the pace of discovery promising HEAs, especially for multicomponent systems.

CHAPTER VI

REAL-TIME INSIGHT INTO THE CYCLIC-DEFORMATION MECHANISMS OF A PRECIPITATION-STRENGTHENED HIGH-ENTROPY ALLOY

6.1 Introduction

Structural components served during engineering applications often suffer fatigue failures, which can cause huge economic losses and casualties [211]. Therefore, fatigue performance of a new structural material is a pivotal criterion to evaluate whether it can be reliably used in a practical engineering environment. Recently, an intriguing new class of metallic structural materials - High-Entropy Alloys (HEAs), shows great potential in the engineering field [1-3, 7, 8, 11, 13, 114]. So far, extensive studies have been performed on HEAs regarding their basic mechanical properties, deformation behavior, and phase transformation during monotonic deformation [7, 11, 33, 212]. However, the study of the fatigue behavior that is strongly correlated with practical applications is very scarce. Some works on high-cycle fatigue (HCF) that covers the accumulated damage caused by elastic strains [14, 15, 17, 27, 213] and fatigue-crack-growth behavior have been published [16, 30, 214], but little research has been reported on low-cycle fatigue (LCF) that characterizes the degradation subjected to plastic strains [31, 32, 215]. Even for the reported three works, the cyclic-deformation mechanisms of HEAs' LCF behavior were not well understood, let alone the real-time insights into cyclic micro-mechanisms of HEAs [31, 32, 215]. Complications of the plastic deformation due to multiple deformation

mechanisms could be triggered at different cyclic stages, which in turn make the understanding more challenging. Moreover, the diverse characteristics in HEAs [4], such as severe lattice distortion, great tendency to form twins, multicomponent precipitations, and obvious short-range ordering (SRO), can strongly affect the cyclic-plastic deformation. Thus, it becomes obviously critical regarding understanding LCF behaviors: (i) how are the LCF behaviors of HEAs, compared with conventional materials; (ii) is there any unique cyclic-deformation mechanisms in HEAs; and (iii) what are the fundamental contributing factors in governing the fatigue behavior of HEAs? To fundamentally understand the fatigue-deformation mechanism and accelerate the engineering applications of HEAs, these critical issues need to be carefully addressed. Here we use the *in-situ* neutron diffraction and detailed microstructural characterizations to provide real-time insights into the LCF deformation mechanisms of a B2 precipitation-strengthened HEA. Through revealing the cyclic-deformation mechanisms of the studied HEA, a new design idea to integrate various beneficial cyclic-deformation mechanisms for designing fatigue-resistant HEAs is provided.

6.2 Materials and Methods

6.2.1 Sample preparation

To prepare HEAs samples suitable for studying their engineering applications, a large plate of $Al_{0.5}CoCrFeNi$ (casting dimensions are ~ 203 × 305 × 76 mm) has been fabricated using the vacuum-induction melting method. The large ingot was then hot rolled with a reduction of 60% at 1,150 ºC to reduce casting defects and refine grain sizes. After hot rolling, the samples were annealed at 1,000 °C for 1 hour to obtain a

recrystallized microstructure and a certain amount of B2 precipitates according to the previously-calculated phase diagram [216]. The specimens for the LCF tests with an 8-mm diameter and 16-mm gauge length were machined along the rolling direction, according to the American Society for Testing and Materials (ASTM) Standard E606-04e1 with a dog-bone shape, as shown in Fig. 1a. After sample machining, the surfaces of the LCF samples were polished to 1,200 grits.

6.2.2 LCF experiments

The fully-reversed strain-controlled LCF tests of the multiphase $Al_{0.5}CoCrFeNi$ HEA consisting of FCC and B2 phases were performed at room temperature (RT) using an MTS Model 810 servohydraulic machine, which were conducted in a wide strain amplitude range from ± 0.1% to ± 1.75% with a triangular loading waveform under a continuous-loading condition. The LCF tests were performed at the strain rate of 1×10^{-2} s^{-1}, and the initial loading is tension.

6.2.3 Microstructural characterizations

Studied alloys were characterized before and after LCF testing, using scanning-electron microscopy (SEM), electron-backscattered diffraction (EBSD), energy-dispersive spectroscopy (EDS), and transmission-electron microscopy (TEM) techniques. The microstructure was characterized, by SEM, employing a Zeiss EVO scanning-electron microscope equipped with the backscattering electron (BSE), EDS, and EBSD detectors. The crystal structures of this multiphase alloy were identified by the synchrotron X-ray diffraction (XRD) on the 11-ID-C beam line at the Advanced Photon Source (APS), Argonne National Laboratory. The specimens for SEM and EBSD were initially polished

to mirror finish using the 1,200-grit SiC paper and, subsequently, vibratorily polished, using the 0.05 μm SiC suspension for the final surface clarification. The TEM imaging was performed on ZEISS LIBRA 200 HT FE MC. Thin foils for the TEM observations were electrical-discharge machined (EDM) from the gauge section of ruptured samples. The thin foils converted into 3-mm-diameter disks for the TEM observations were prepared by twin-jet polishing, using an electrolyte consisting of 95 % (volume percent) ethanol and 5% perchloric acid in a volume fraction at a temperature of - 40 °C and an applied voltage of 30 V. The examination of many specimens, including foils from the undeformed section, exhibited that very few artefact dislocations were produced by this TEM sample-preparation technique.

6.2.4 In-situ neutron diffraction measurements

In-situ neutron diffraction was performed during fully-reversed strain cycling of the multiphase HEA on the VULCAN Engineering Materials Diffractometer at the Spallation Neutron Source (SNS), Oak Ridge National Laboratory (ORNL) [217, 218]. Screw-threaded cylindrical dog-bone samples with the same gauge diameter of 8 mm and length of 16 mm were used for the *in-situ* neutron measurements. The LCF specimen was mounted horizontally in the VULCAN MTS loadframe with the alignment of the loading direction parallel to the rolling direction (RD) and horizontal-radial direction along the normal direction (ND). The incident neutron beam was 45° to the sample. Two stationary detector banks were located at the ± 90° direction to the incoming neutron beam, which were used to record the diffraction information in the axial and radial directions during

mechanical loading, repsectively. The incident neutron beam size was defined as 7 mm × 7 mm, with 5 mm receiving collimators.

In this study, low, intermediate, and high strain amplitudes of ± 0.50%, ± 1.00%, and ± 1.75% were chosen for the *in-situ* neutron diffraction continuous measurements, respectively. Moreover, the strain amplitude at ± 1.00% was also measured using the holding mode. The holding points marked by the green squares in Fig. 2c were chosen for the measurement (10 min. for each point) at the selected cycles. At the strain amplitude of ± 0.50%, the fatigue cycles, 1^{st}, 2^{nd}, 5^{th}, 10^{th}, 20^{th}, 50^{th}, 100^{th}, 150^{th}, 200^{th}, 250^{th}, 500^{th}, $1{,}000^{th}$, $1{,}500^{th}$, $2{,}000^{th}$, and $3{,}000^{th}$ cycles, were selected for the real-time *in-situ* neutron diffraction measurements. At the strain amplitude of ± 1.00%, the fatigue cycles, 1^{st}, 2^{nd}, 5^{th}, 10^{th}, 20^{th}, 50^{th}, 100^{th}, 150^{th}, 200^{th}, 250^{th}, 500^{th}, $1{,}000^{th}$, and $1{,}500^{th}$ cycles, were chosen for the real-time *in-situ* neutron diffraction measurements. The fatigue cycles, 1^{st}, 2^{nd}, 5^{th}, 10^{th}, 20^{th}, 50^{th}, 100^{th}, and 150^{th} cycles, at the strain amplitude of ± 1.75%, were selected for the real-time *in-situ* neutron diffraction experiments. To ensure enough time for recording neutron diffraction patterns, the strain rate of the selected cycles was at the level of $7.4 \times 10^{-6}\ s^{-1}$, while other fatigue cycles were with a strain rate of $1 \times 10^{-2}\ s^{-1}$, the same with laboratory LCF testing. During the continuous cyclic loading, neutron diffraction patterns were recorded successively. After the measurements, the data were chopped into small-time bins, using the event-based data-reduction software, the VULCAN Data Reduction and Interactive Visualization softwarE (VDRIVE) [177]. In the present study, the time intervals of 2 min., 3 min., and 3 min. were selected for the strain amplitudes of ± 0.5%, ± 1%, and ± 1.75%, respectively, based on both the quality and the statistics of neutron diffraction results.

6.3 Results

6.3.1 Microstructural characterizations

Dog-bone shape samples with a gauge length of ϕ8 × 16 mm of the $Al_{0.5}$CoCrFeNi alloy were fabricated for the LCF experiment (Figure 6.1a). This alloy is composed of FCC and B2 phases (compositions listed in Table 6.1), with a nominal grain size of about 7 μm, as presented in the electron-backscattered diffraction (EBSD) phase map (Figure 6.1b) and the inverse polar figure (IPF) (Figure 6.1c). The B2 precipitates exhibit two different hierarchical morphologies: one is the fine and dense B2 precipitates with blocky and needle shapes within the FCC grains (Figure 6.1b), and the other is the coarse band-like B2 phase located at the parent grain boundaries. The FCC and B2 phases are further verified by transmission-electron microscopy (TEM) (Figure 6.1d and 6.1e) and high-energy X-ray diffraction (HEXRD) (Figure 6.1f). After the Rietveld refinement on the HEXRD data, the lattice parameters of FCC (3.5931 Å) and B2 (2.8741 Å) phases and the phase fraction of the B2 phase (~ 12%) were determined.

6.3.2 Monotonic and cyclic stress responses

Monotonic uniaxial tension shows that this alloy has a good combination of the high yield strength (487 MPa), work hardening, and ultimate tensile fracture stress of 940 MPa with ductility up to (44%) (Figure 6.2a). Figure 6.2b presents the evolution of stress amplitudes with the number of cycles under different strain amplitudes. Obviously, the cyclic-stress-response (CSR) and fatigue life are dependent on the applied strain amplitudes. As the increase of the strain amplitude, the stress amplitude increases, but the

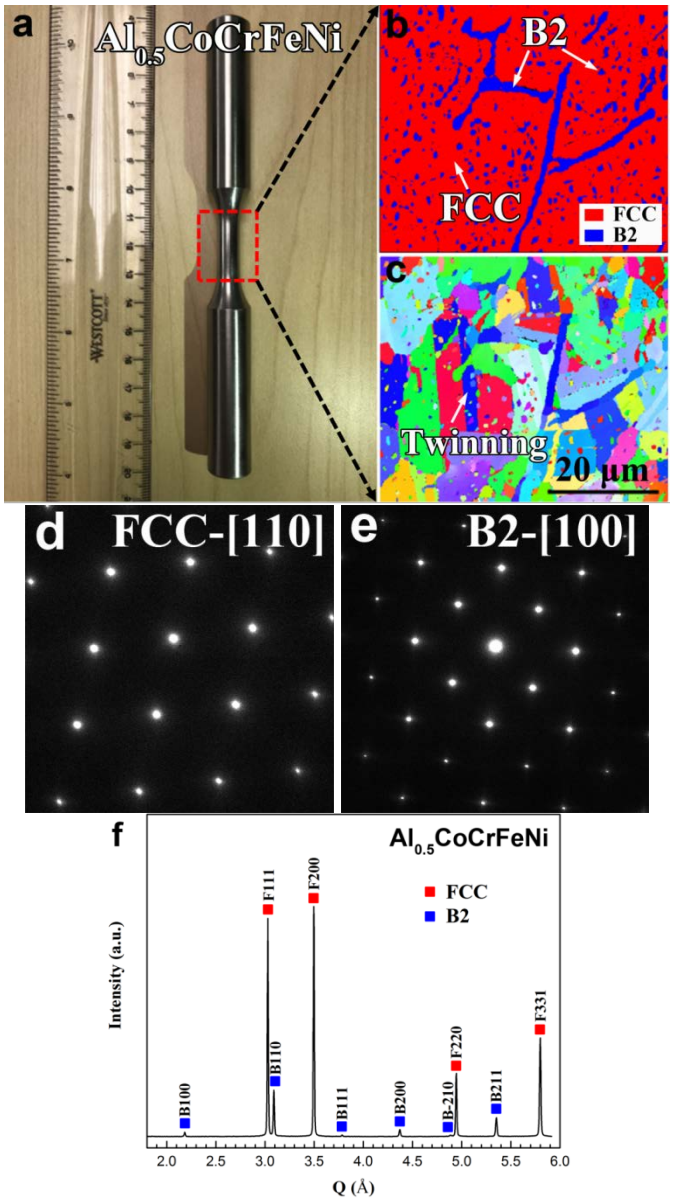


Figure 6.1 LCF sample and microstructural information. (a), Sample used for LCF testing. (b) and (c), EBSD phase map and corresponding IPF image, respectively. (d) and (e), Selected area electron diffraction (SAED) patterns of FCC and B2 phases, respectively. (f), HEXRD of the $Al_{0.5}$CoCrFeNi alloy, showing the presence of FCC and B2 phases (the diffraction peaks of FCC and B2 phases are indexed as F*hkl* and B*hkl*, respectively).

Table 6.1 Chemical compositions of the FCC matrix and B2 precipitates in the $Al_{0.5}CoCrFeNi$ HEA (in atomic percent, at.%) measured by energy-dispersive scanning (EDS).

Phases	Al	Co	Cr	Fe	Ni
FCC	8.26 ± 0.27	24.39 ± 0.74	23.83 ± 0.64	23.64 ± 0.67	19.70 ± 0.60
B2	26.51 ± 0.81	17.33 ± 0.67	8.41 ± 0.32	12.45 ± 0.46	35.30 ± 1.22

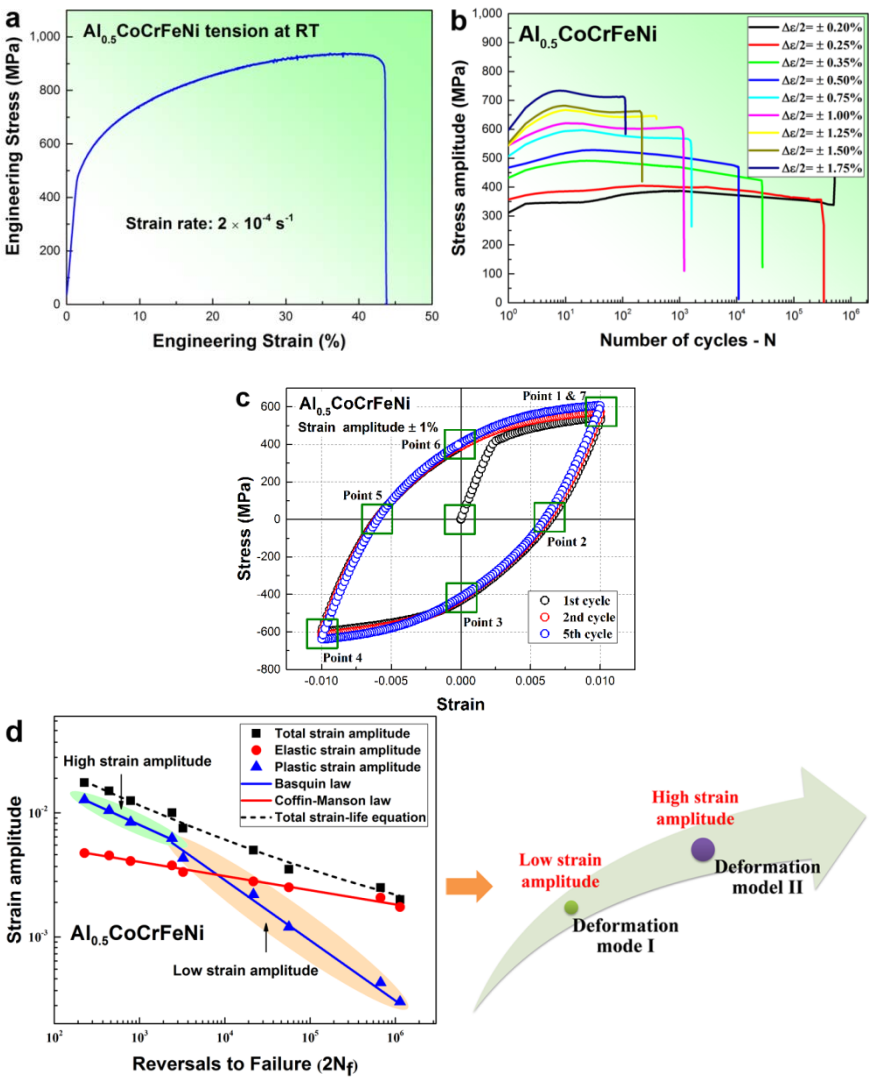


Figure 6.2 Tensile and LCF results of the $Al_{0.5}CoCrFeNi$ alloy. (a), Uniaxial tensile curve of the $Al_{0.5}CoCrFeNi$ alloy at RT. (b), Cyclic-stress response (CSR) curves of the $Al_{0.5}CoCrFeNi$ HEA at different strain amplitudes. (c), Hysteresis loops of the $Al_{0.5}CoCrFeNi$ HEA at selected typical numbers of cycles fatigued at the strain amplitude of ± 1%. (d), Total strain amplitude, elastic strain amplitude, and plastic strain amplitude versus the number of reversals to failure ($2N_f$), displaying the presence of a bilinear Coffin-Manson relationship that signifies a variation of the cyclic-deformation modes.

fatigue life decreases. Moreover, changing from cyclic hardening to softening, and/or saturation is also observed. The stress amplitude increases rapidly in the initial stage of cycling, followed by cyclic softening and/or saturation. The selected hysteresis loops of the strain amplitude of ± 1% depict the remarkable initial cyclic hardening (Figure 6.2c). At larger strain amplitudes (≥ ± 1%), a slight cyclic softening was observed after the initial hardening, and then, a cyclic saturation was kept until fracture. However, an obvious cyclic softening happens until fracture when the applied strain amplitude is smaller than ± 1%.

6.3.3 Fatigue life prediction

The fatigue life of this HEA was evaluated by the strain/stress-life equations, i.e., Basquin and Coffin-Manson laws [219-221]. For the high-cycle fatigue (HCF) regime, the stress-based Basquin law (stress-life equation) is used to determine the fatigue life [219].

$$\Delta\sigma / 2 = \sigma_f^{'}(2N_f)^b \tag{6.1}$$

In the LCF regime, the plastic strain based Coffin-Manson law (strain-life equation) is widely used for the life prediction [220, 221].

$$\Delta\varepsilon_p / 2 = \varepsilon_f^{'}(2N_f)^c \tag{6.2}$$

Since the LCF tests contain both the elastic and plastic regimes, the Basquin and Coffin-Manson laws need to be combined for predicting the fatigue life. Therefore, the total fatigue-life prediction can be expressed as follows.

$$\Delta\varepsilon_t / 2 = \Delta\varepsilon_e / 2 + \Delta\varepsilon_p / 2 = \left(\frac{\sigma_f^{'}}{E}\right)(2N_f)^b + \varepsilon_f^{'}(2N_f)^c \tag{6.3}$$

where $\Delta\varepsilon_t / 2$ is the total strain amplitude; $\Delta\varepsilon_e / 2$ is the elastic-strain amplitude; $\Delta\varepsilon_p / 2$ is

the plastic-strain amplitude; $\sigma_f^{'}$ is the fatigue-strength coefficient, MPa; E is the modulus of elasticity (~ 174 GPa); N_f is the number of cycles to failure; b is the fatigue-strength exponent; $\varepsilon_f^{'}$ is the fatigue-strain coefficient; c is the fatigue-ductility exponent.

Fitted by the above equations, the relationship of the total strain amplitude, elastic strain amplitude, and plastic strain amplitude as a function of the number of reversals to failure ($2N_f$) is plotted in the Figure 6.2d (fitting parameters are given in Table 6.2). It can be seen that the classic fatigue-life models fit the fatigue results very well. It is worth noting that a bilinear Coffin-Manson rule is observed in the relationship of the fatigue life vs. plastic strain amplitude, suggesting a change of the cyclic-deformation mode with the applied strain amplitudes, as depicted by the carton in Figure 6.2d.

6.3.4 In-situ neutron diffraction during monotonic and cyclic loadings

To dynamically unravel the deformation modes at different strain amplitudes, an *in-situ* probing tool is required. Neutrons measure the atomic and mesoscale response in bulk materials by collecting the phase-specific lattice strain, texture, slips, as well as phase transformations, which are often used for understanding mechanical plastic deformations [61, 222-224]. Here, the real-time *in-situ* neutron diffraction was performed on this alloy during the uniaxial tension and fully-reversed strain cycling. Figure 6.3a shows the lattice strain versus applied tensile stress along the longitudinal and transverse directions (LD and TD) for selected orientations of both FCC and B2 phases. The hkl plane-specific lattice strain of each respective phase is determined by $\varepsilon_{hkl} = \left(d_{hkl} - d_{hkl}^0\right) / d_{hkl}^0$, where d_{hkl}^0 and d_{hkl} are the reference lattice spacings at the stress-free state and the lattice spacing

Table 6.2 The fitting values of parameters shown in the strain-life equation

Parameters	$\sigma_f^{'}$ (MPa)	$\varepsilon_f^{'}$	b	c
Fitting values	1,315	0.10253	0.11414	0.36835

Figure 6.3 Real-time in-situ neutron diffraction results. (a), Lattice strain as a function of applied stress during the uniaxial tension. (b), Two-dimension (2D) contour maps of the B2-{110} d-spacing along the transverse direction, exhibiting the formation of the martensitic phase. (c), Lattice-strain evolutions of the FCC-{111} and B2-{110} at selected 1^{st}, 2^{nd}, and 5^{th} cycles along loading direction. (d), The evolution of $FWHM_G/d$ versus the number of cycles at the strain amplitudes of ± 0.5%, ± 1%, and ± 1.75%. e, The relationship of B2-[110] FWHM versus applied stress along longitudinal and transverse directions at 50^{th} cycle at the strain amplitude of ± 1.75%. (f) and (g), The real-time *in-situ* neutron diffraction peak-intensity evolution at different fatigue cycles along longitudinal and transverse directions at the strain amplitudes of ± 1.75% and ± 1%, respectively.

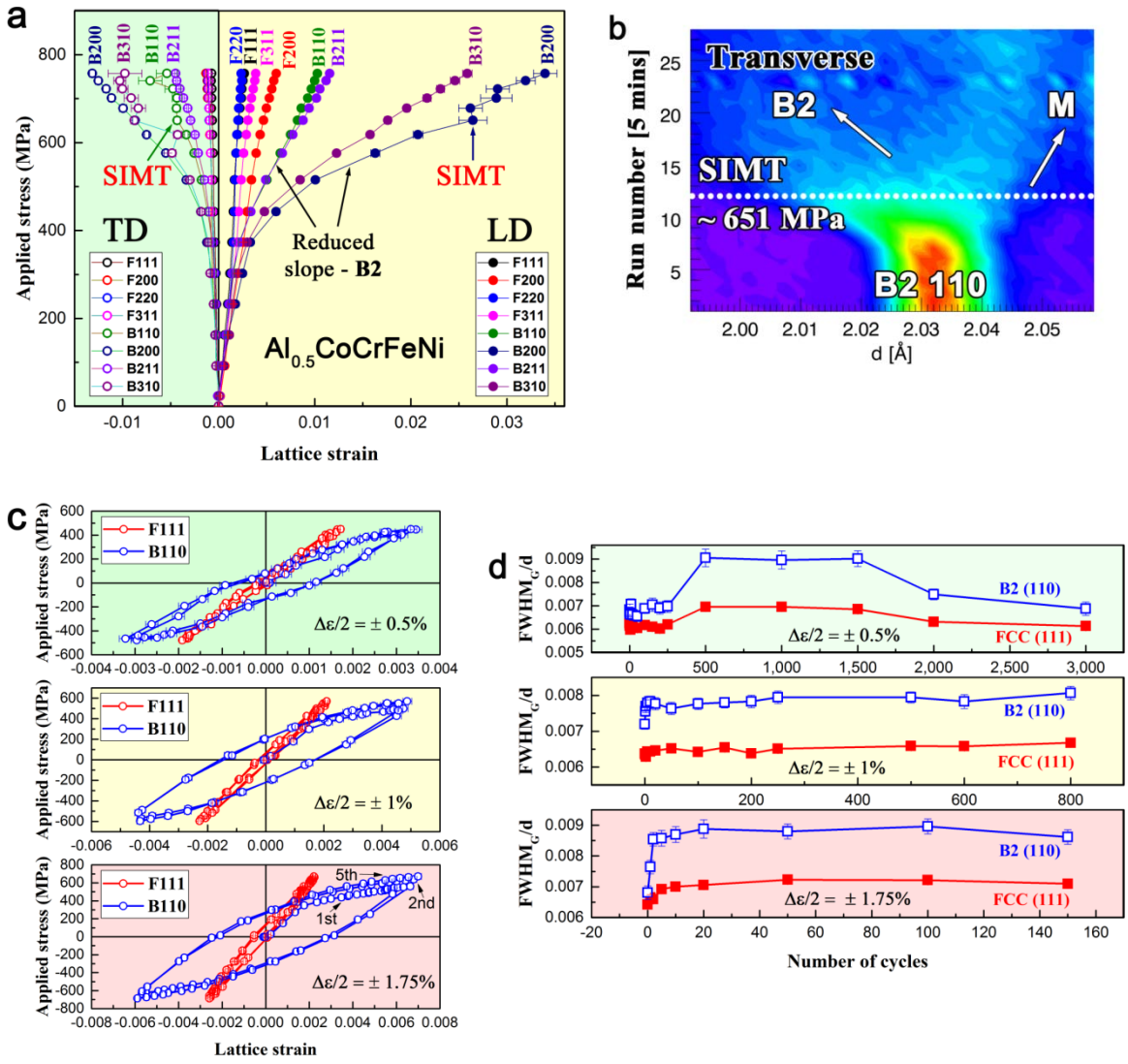


Figure 6.3 continued

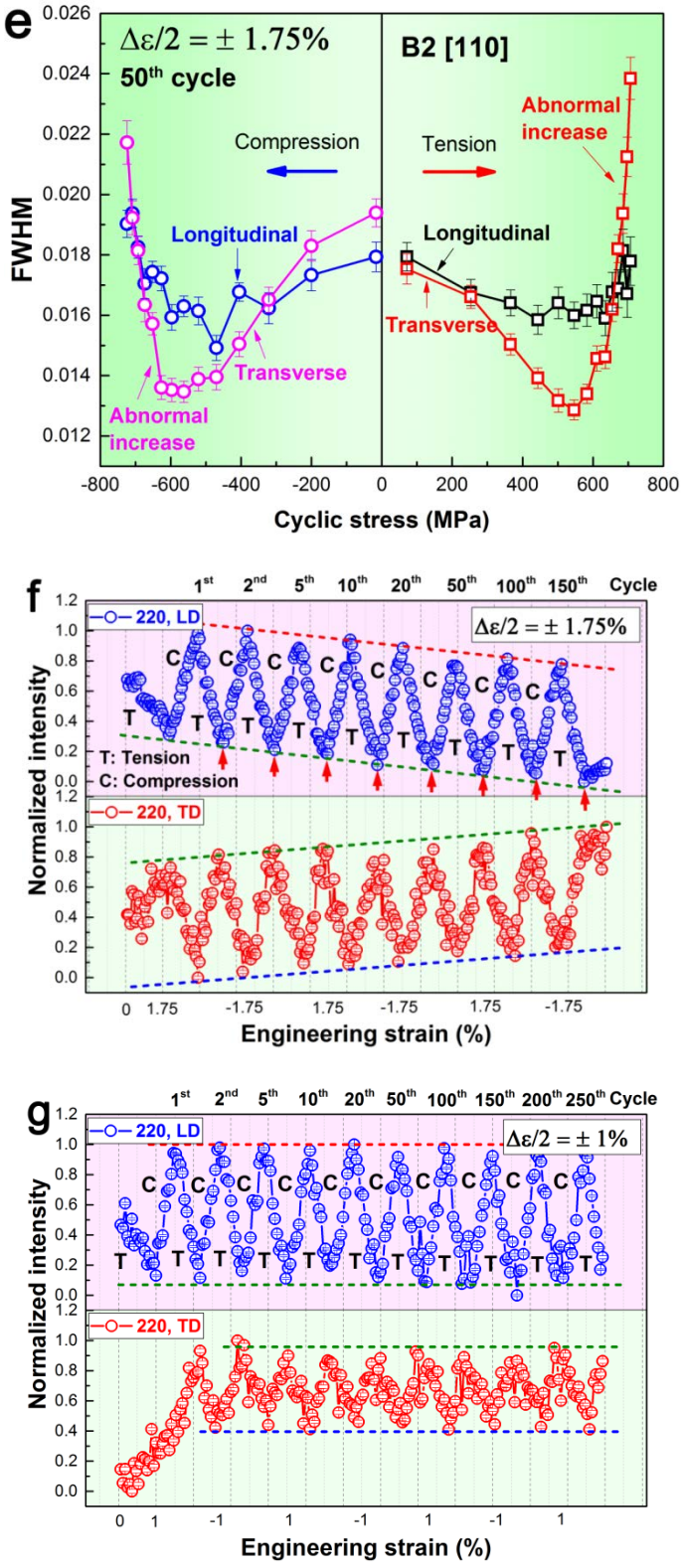


Figure 6.3 continued

during loading, respectively. A linear response of the lattice strain to applied stress is found during the elastic range. Different slopes among various grain families and phases are due to the elastic anisotropy. Right after yield, an obvious splitting of lattice strains happens between the B2 and FCC phases, especially the B2-{200} and {310} grains. This lattice-strain response manifests that the load transfers to the hard B2 phase after the soft FCC phase yields first[61]. Similarly, the load transfer is observed during the cyclic pull-push loading, as exhibited by the large lattice strain and stress borne by the hard B2 phase (Figure 6.3c). Moreover, as the strain amplitude increases, more energy is dissipated in both B2 and FCC phases, as evidenced by the increased area of the hysteresis loop (Figure 6.3c).

One of particular interests in Figure 6.3a is that there is a jump of the B2-{200} and {110} lattice strains along LD and TD, respectively, when the applied stress is larger than 651 MPa. It is considered to be a result of the stress-induced martensitic transformation (SIMT), which is further evidenced by the separation of the B2 {110} peak along TD (Figure 6.3b). This phase-transformation behavior is also demonstrated by *in-situ* HEXRD patterns, in which the peak of B2-{110} along TD separates into two peaks when the tensile stress exceeds ~ 650 MPa, consistent with the in-situ synchrotron diffraction results (Figure 6.4). Obviously, this SIMT has a preferred orientation selection, that is, B2-[110]//TD, similar to a previous report [225]. Due to the inadequate data-collecting time during the *in-situ* neutron measurement, it becomes difficult to differentiate the peak separation during cyclic loading. However, the SIMT can cause the overlap of the peaks belonging to B2 and new martensitic phases, leading to abnormal

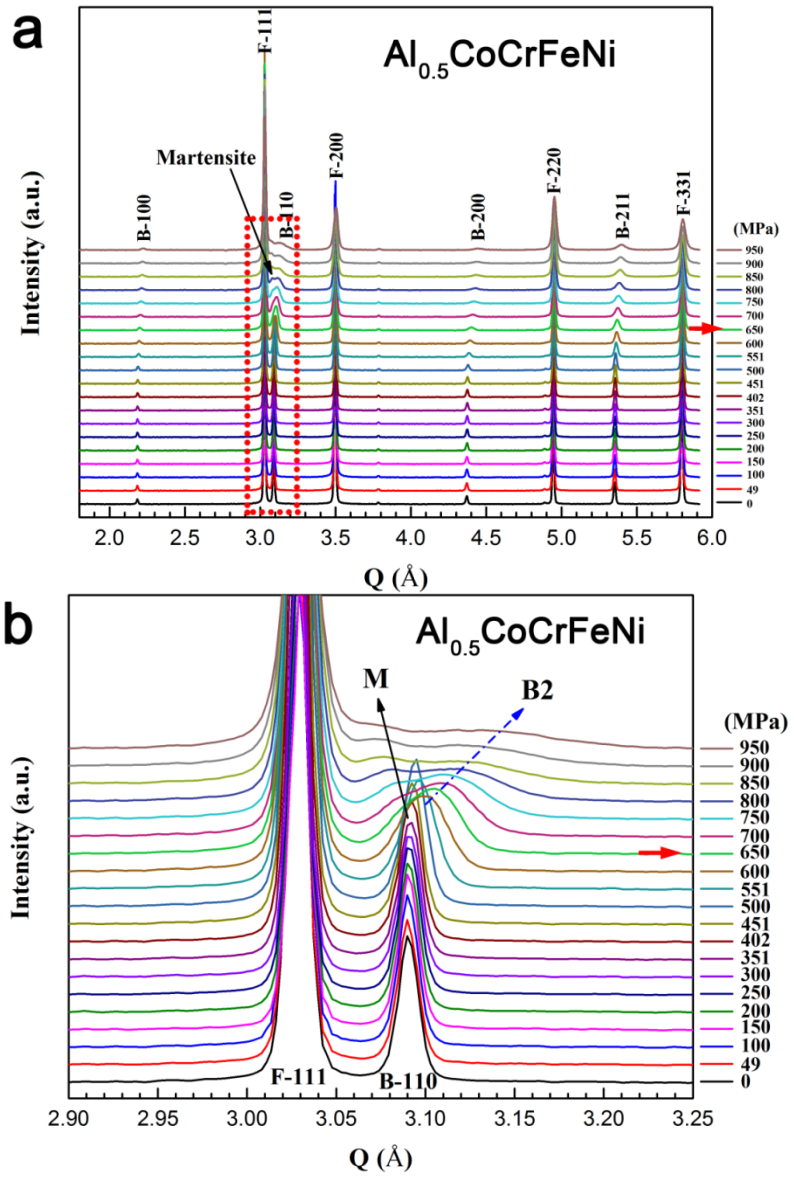


Figure 6.4 Synchrotron XRD diffraction profiles as a function of the applied tensile stress. (a), Full patterns along the transverse direction (TD), (b), B-[110] along TD during the uniaxial tension (M denotes the martensite), showing the occurrence of the martensitic transformation upon the stress beyond 650 MPa (marked by the red arrow).

peak broadening. Moreover, the present type of SIMT is strongly dependent on the loading direction and grains orientations, i.e., B2-[110]//TD. Thus, if an abnormal difference of peak broadening of B2-{110} exists between LD and TD, we can conclude the occurrence of SIMT during cyclic loading.

To prove this point, the relationships of the peak full width at half maximum (FWHM) of B2-{110} vs. cyclic stress along LD and TD at a selected cycle are plotted at the strain amplitudes of ± 0.5%, 1%, and 1.75%. Figure 6.3e exhibits this relationship at the 50^{th} cycle under the strain amplitude of ± 1.75%. It can be clearly seen that an abnormal increase of FWHM happens along TD when the stress is larger than ~ 600 MPa, rather than LD, suggesting that the abnormal broadening behavior should be attributed to the SIMT, instead of a simple dislocation evolution. This abnormal increase of FWHM also occurs at the strain amplitude of ± 1%, but not at the strain amplitude of ± 0.5% (Figure 6.5). Thus, SIMT occurs when the strain amplitude is larger than ± 1%.

To understand the cyclic hardening and softening behavior in CSR, the dynamic evolution of the dislocation density is qualitatively established through analyzing the FWHM. As mentioned above, SIMT also contributes to the broadening FWHM of B2-{110} along TD, but not the B2-{110} along LD. Therefore, here we use the FWHMs that were extracted from B2-{110} along LD. FWHM is related to the dislocation density by the proportional relation [226] of

$$\rho \propto \frac{FWHM_{G,hkl}^{2}}{d_{hkl}^{2} b C_{r}} \tag{6.4}$$

where ρ is the total density of randomly-distributed dislocations, *hkl* is the Miller index,

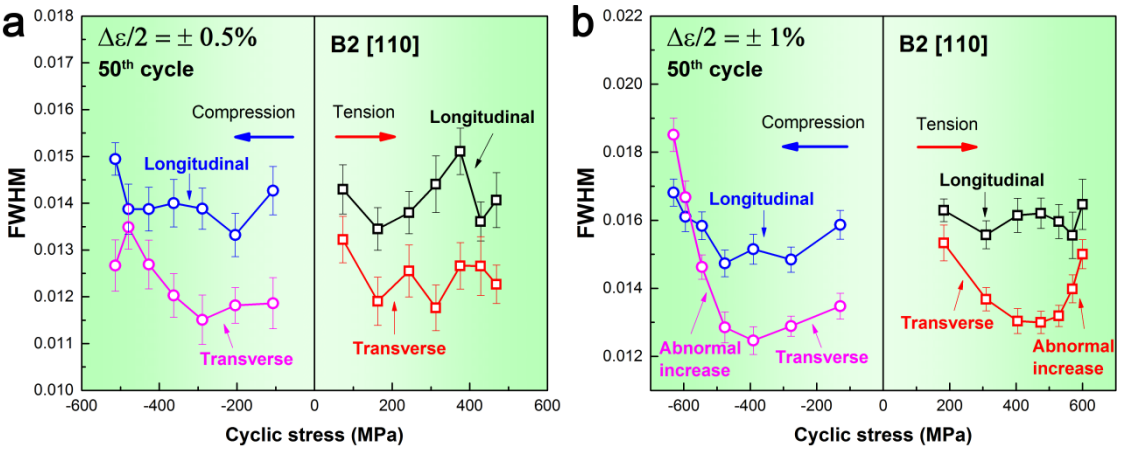


Figure 6.5 The relationship of B2-[110] FWHM versus applied stress along the longitudinal and transverse directions at the 50th cycle under the strain amplitudes of ± 0.5% (a) and ± 1% (b).

$FWHM_G$ is the Gaussian component of the FWHM of the peak obtained from single-peak fitting by the pseudo-Voigt function, *d* is the lattice-plane spacing, *b* is the magnitude of the Burgers vector, and C_r is the contrast factor related to the dislocation type (edge or screw) [227]. Note that all the FWHM are obtained at the load-free condition during cyclic loading in order to minimize the effect of the external force on the peak width. The representative diffraction peaks of {111} and {110} along LD were used to extract the FWHM of the FCC and B2 phases, respectively. Figure 6.3d shows the evolution of $FWHM_G$/d of the {111} peak in the FCC phase and the {110} peak of the B2 phase at the strain amplitudes of ± 0.5%, ± 1 %, and ± 1.75%. At the low strain amplitude of ± 0.5%, $FWHM_G$/d of the FCC-{111} and B2-{110} peaks exhibits a relatively-stable stage at the first 250 cycles, and then, quickly increases to a higher level until 500 cycles. Later, a steady stage appears from the 500^{th} cycle to $1{,}500^{th}$ cycle, and finally with a decrease until the $3{,}000^{th}$ cycle. This evolution of $FWHM_G$/d at the strain amplitude of ± 0.50% indicates that three obvious cyclic stages are present, that is, (i) the dislocation rapid multiplication - cyclic hardening, after a relatively-stable incubation period; (ii) the balance between the dislocation multiplication and annihilation - cyclic saturation; and (iii) the reduced dislocation density - cyclic softening. At higher strain amplitudes of ± 1% and ± 1.75%, a rapid increase of $FWHM_G$/d happens in the first few cycles, and then followed by a steady stage. No obvious decrease of $FWHM_G$/d is found at the later stages, indicating the absence of obvious cyclic softening that happened at low strain amplitudes (< ± 1%). It is interesting to note that the B2 phase is plastically deformable at all the three strain amplitudes, as demonstrated by the greatly increased $FWHM_G$/d, which is caused by the stored dislocations as shown by TEM observation (Figure 6.6). The plastically-deformable

behavior of the B2 phase suggests load transfer and strain partitioning occurs between the FCC matrix and B2 precipitates, which can relieve the stress concentration. The real-time monitored cyclic-response behaviors at the strain amplitudes of ± 0.5%, ± 1% and ± 1.75% are consistent with their corresponding cyclic-stress responses in Fig. 2b.

Besides the dislocation evolutions, twinning micromechanical behavior during LCF can be dynamically detected as well because of the sensitivities of *in-situ* neutron to the diffraction intensity change caused by the deformation twinning [224, 228, 229]. In a FCC structure, <111>, <220>, and <331> orientations favor the deformation twinning. Here the <220> orientation is selected to probe the twinning behavior. Figures 3f and 3g show the evolutions of the normalized intensity vs. cycles along LD and TD at the strain amplitudes of ± 1.75% and ± 1%, respectively. In <220>//LD orientation, both the dislocation slip and twinning decrease the <220> intensity in tension [229]. In Figures 6.3f and 6.3g, we observed the gradually-decreased peak intensity in tension (highlighted by the red arrows in Figure 6.3f) with the increase of cycles at the strain amplitudes of ± 1.75% instead of the strain amplitudes of ± 1%. This trend is due to the extra contribution from deformation twinning at the strain amplitudes of ± 1.75% that leads to the peak intensity in tension more negative as the cycle increases. Thus, it indicates that the deformation twinning occurs at the high strain amplitude of ± 1.75%, but not at the intermediate strain amplitudes, ± 1%. The real-time captured twinning behavior is further supported by the following TEM characterizations.

To visually link the observed cyclic response with the microstructural evolution, detailed microstructural characterizations were performed on the post-mortem samples at different strain amplitudes. Figures 6.6a-h display the varied deformation features from the low strain amplitude of ± 0.25% to the highest strain amplitude of ± 1.75% after LCF testing. At the lower strain amplitudes (below ± 1%), dislocation slips, including cross slips, double slips, and planar arrays, prevail (Figures 6.6a-d). As the strain amplitude increases to ± 1%, dislocation cells are formed, resulting from the extensive cross slips of dislocations in the FCC matrix. Note that no deformation twinning is observed at the strain amplitude of ± 1% after screening more than 20 grains, in line with the *in-situ* neutron results (Figure 6.3g). When the strain amplitudes further increase to ± 1.75%, elongated dislocation cells are found, separated by much denser and severely tangled dislocations. Moreover, deformation nanotwins are observed, as presented in the bright-field (BF) TEM image (Figures 6.6g) and high-resolution TEM (HRTEM) (Fig. 4h). It is worth noting that the deformation twins are formed in the severely-tangled dislocations region (highlighted by the dash box in Figures 6.6g). This trend is because that the formation of deformation twinning requires sufficient resolved shear stress to reach the critical stress for twinning [230, 231]. At high strain amplitudes, dislocations are more tangled and denser than those at low strain amplitudes, leading to the local shear stress beyond the critical stress for the formation of twinning. As a consequence, deformation twinning can be observed at high strain amplitudes instead of intermediate and low strain amplitudes, in agreement with the real-time neutron results (Figures 6.3f and 6.3g). At all strain amplitudes, very dense dislocations pile-up around the B2-phase boundaries, which is ascribed to the strain incompatibility of the FCC and B2 phases. Upon cyclic testing,

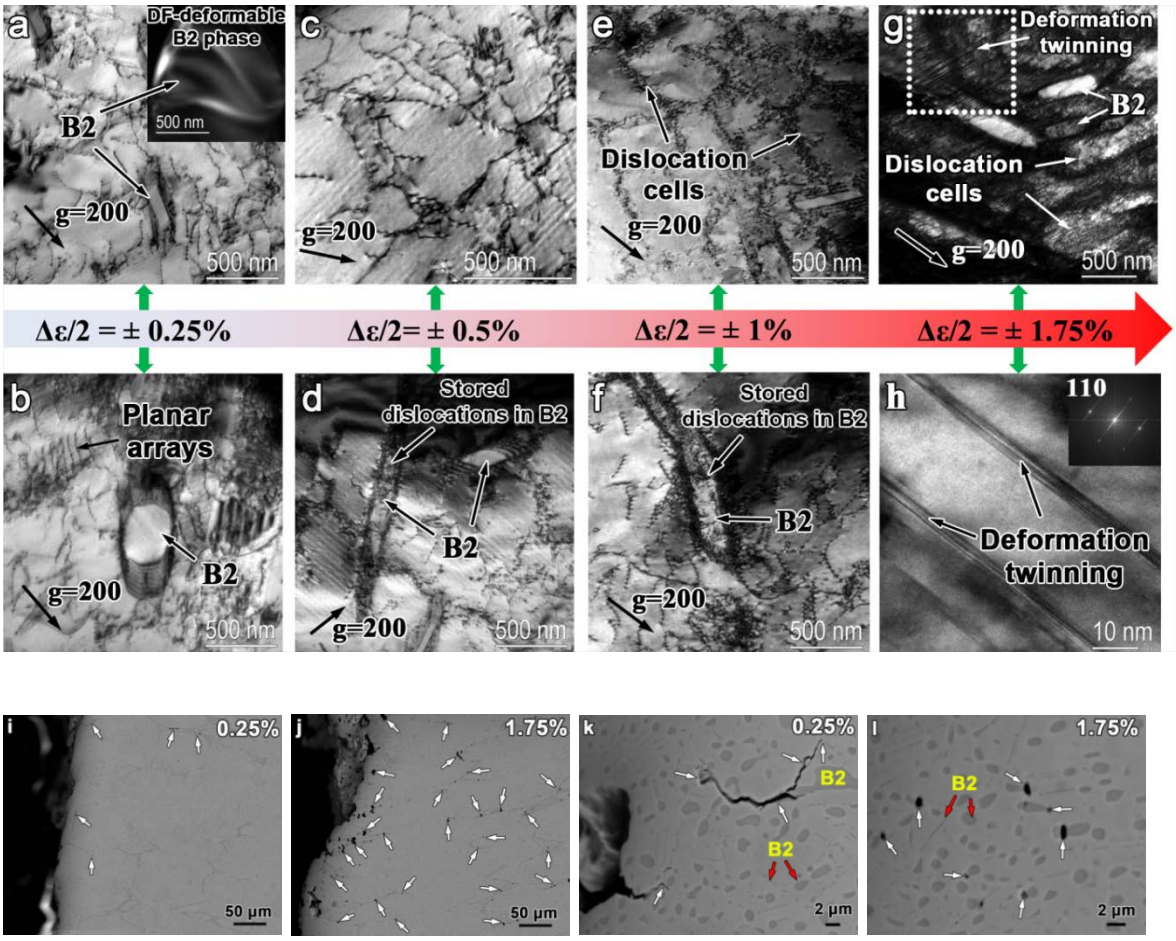


Figure 6.6 TEM and SEM characterized structural evolution at different strain amplitudes. (a) and (b), (c) and (d), (e) and (f), and (g) and (h) are the TEM bright-field (BF) images at the strain amplitudes of ± 0.25%, ± 0.5%, ± 1%, and ± 0.25%, respectively, showing the structural evolution of the cyclic response of deformation features (the inset figure in Figure 6.6a is the dark-field (DF) image, showing the plastically-deformable B2 phase). (i-l) are the SEM images of the fractured samples at the strain amplitudes of ± 0.25% and ± 1.75%, exhibiting the crack-formation features at low and high strain amplitudes.

plastic deformation occurs in the soft FCC matrix first, leading to the great increase of the dislocation density by the multiplication and rearrangement of dislocation substructures in the FCC matrix. In contrast, the precipitated hard B2 phase resists plastic deformation and acts as obstacles, which hinders the further movements of dislocations and produces the internal stress, i.e., back stress, contributing to the cyclic strain hardening. As the cycle and cyclic strain increase, plastic deformation propagates gradually into the hard B2 phase, as evidenced by the observed dislocations in the B2 phase (Figures 6.6). The heterogeneous deformation between the hard B2 and soft FCC phases can raise a localized stress concentration between their boundaries and cause microcracks (Figures 6.6i-l). However, due to the deformability of the B2 phase, B2 can deform to provide necessary accommodation between FCC and B2 phases, resulting in the relaxation of the severe stress concentration and retarding the initiation of microcracks. In fact, microcracks mainly initiate and propagate near the boundaries of the band-like B2 precipitates at both low and high strain amplitudes, because of their longer incoherent B2 interfaces that cannot effectively accommodate the stress concentration (Figures 6.6i and 6.4j,). In contrast, microcracks are difficult to initiate near the boundaries of the fine B2 precipitates. Even though microcracks are formed near the fine B2 precipitates at the high strain amplitude of ± 1.75%, they are in the circle-like shape (Figures 6.6l). Interestingly, these circle-like cracks with blunted crack-tips indicate that the fine B2 precipitates can act as efficient crack arresters to inhibit crack propagation and coalescence during cyclic deformation[33], unlike those cracks near the band-like B2 phases. The formation of microcracks leads to the cyclic softening because of the accelerated annihilation rate of dislocations. Another cyclic-softening source can be the interaction between the short-

range ordering (SRO) and dislocations [232]. In this $Al_{0.5}$CoCrFeNi HEA, Al-Ni and Cr-Fe are the possible SRO pairs [115, 186]. Due to the presence of SRO, the planar slip tends to form, as manifested by the observed planar arrays (Figures 6.6b). Once the SRO is broken down by the leading dislocation, the following dislocation faces a lower resistance to slip, contributing to the cyclic softening. Both the formation of microcracks and the presence of SRO are responsible for the observed cyclic softening at low strain amplitudes (< ± 1%).

At high strain amplitudes (> ±1 %), deformation twinning is present, which acts as barriers to hinder the further dislocation movement, notable cyclic hardening can be achieved to compensate the softening caused by the dislocation annihilation, SRO effect, and crack formation. Thus, this HEA exhibits cyclic stability after initial hardening at high strain amplitudes (≥ ± 1%), rather than cyclic softening at low strain amplitudes (≤ ± 1%) (Figures 6.2b and 6.3d). Therefore, at the high strain amplitudes (> ± 1%), the deformation mode becomes the strong interaction between dislocations and deformation nanotwins, elongated dislocation cells, and SIMT.

To vividly summarize the evolution of the deformation mode as the strain amplitude increases, a schematic is plotted in Figure 6.7a. At low strain amplitudes (< ± 1%), the cross slips together with planar arrays are the dominant cyclic-deformation mechanisms. When the strain amplitude reaches ± 1%, dislocation cells and SIMT begin to appear. As the strain amplitude further increases (> ± 1%), deformation twinning is formed, except for the dislocation cells and SIMT, and thus, dislocation cells, SIMT, and the interaction between the dislocation and twinning are the dominant cyclic-deformation mechanisms. Note that at all strain amplitudes, dislocations always pile-up at the hard B2

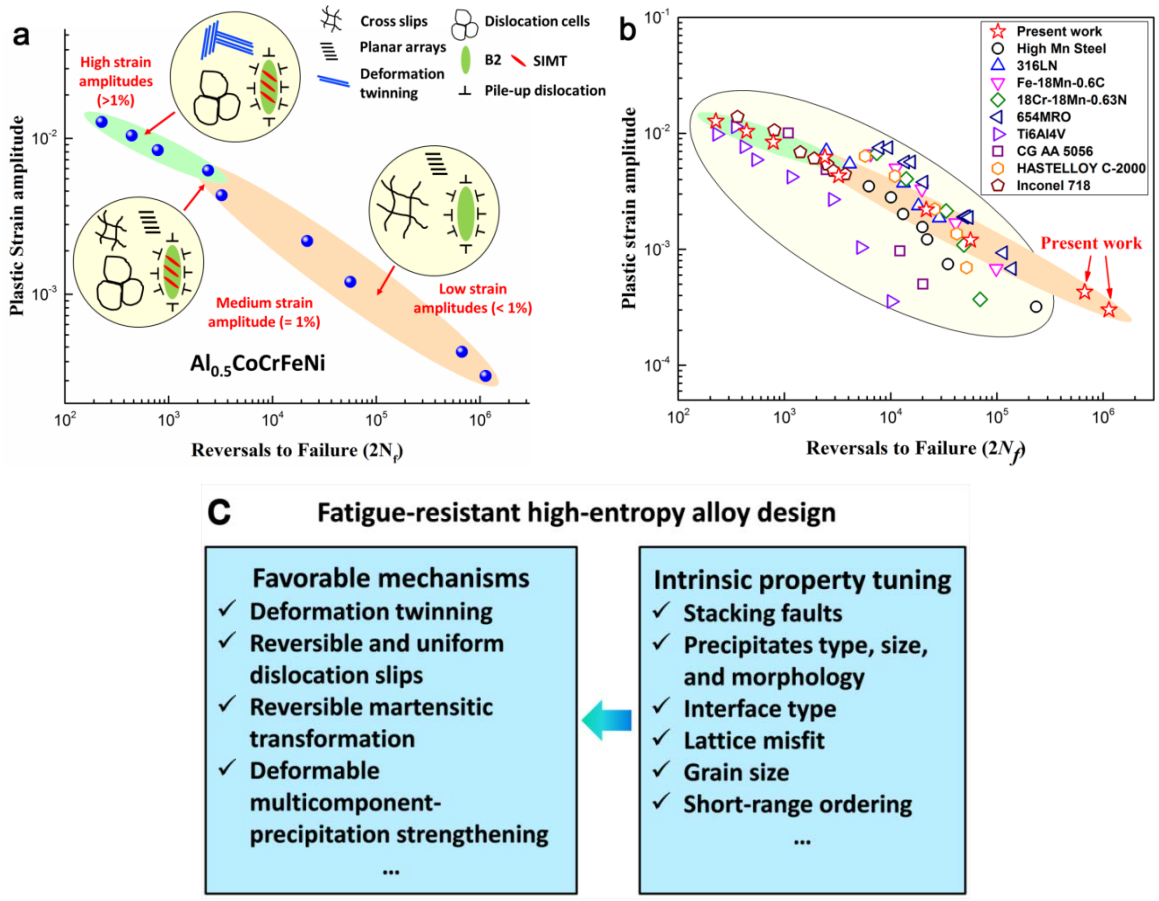


Figure 6.7 (a), Summary of dominated cyclic-deformation mechanisms of $Al_{0.5}CoCrFeNi$ at different strain amplitudes. (b), The comparison of Coffin-Manson fatigue data for the present alloy and other conventional alloys [232-238]. (c), A mechanistic approach to the design of fatigue-resistant high-entropy alloys based on the present study.

phase boundaries, leading to the localized stress concentration and triggering the formation of microcracks. However, due to the plastically-deformable B2 phase, the microcracks near the fine B2 precipitates can be retarded. Correspondingly, the initiation and coalescence of microcracks are easier to occur near the band-like B2 phase.

6.4 Discussions

A full picture of the cyclic-deformation mechanisms that evolve as the strain amplitude increases has been drawn through the real-time investigation (Figure 6.7a). Now we can answer the three critical questions raised at the beginning. *How is the LCF property of this selected HEA, compared with other traditional materials?* To answer this question, a map plotting the relationship of a reversal to failure ($2N_f$) versus plastic-strain amplitude among many different materials is given (Figure 6.7b) [232-240]. It can be seen that the studied alloy shows comparable LCF properties with traditional materials, such as various steels, nickel-base superalloys, aluminum alloy, and Ti6Al4V, at high plastic strain amplitudes ($> 10^{-3}$). In contrast, at low plastic strain amplitudes ($< 10^{-3}$), the studied HEA exhibits a much longer fatigue lifetime than other materials, as reflected by the smaller slope of plastic strain amplitude vs $2N_f$. *Are there any unique cyclic-deformation mechanisms in HEAs?* In the studied HEA, diverse deformation modes, including dislocation slips (cross slips and planar slips), dislocation cells, SIMT, and deformation twinning, are observed at different strain amplitudes. No persistent slip bands (PSBs) and persistent Lüders bands (PLBs) resulting from cyclic loading is found [241]. More importantly, the plastically-deformable B2 phase retards the initiation of microcracks because of the strain partitioning. The appeared various deformation modes in a HEA

create a new palette to synergistically integrate the deformation mechanisms that favor the fatigue properties of HEAs, which is the unique feature in HEAs. With the abundant choices from the palette, novel fatigue-resistance HEAs can be designed through rationally-integrating the favorable deformation mechanisms. To provide this insight, we will address the third question: *What are the fundamental contributing factors in governing the fatigue behavior of HEAs?* In this study, the evolution of cyclic-deformation mechanisms at different cyclic strain amplitudes is witnessed. The longer fatigue lifetime at low strain amplitudes is attributed to the retarded initiation and coalescence of microcracks because of the low-stress level and the plastic deformability of B2 precipitates Figure 6.6). On the contrary, the shorter fatigue lifetime at high strain amplitudes is ascribed to the fast formation rate of microcracks, resulting from the high-stress level and the unaccommodated strain gradient between the FCC matrix and the band-like B2 phase that has longer and more incoherent interfaces (Figure 6.7j). Thus, in order to delay the initiation and coalescence of microcracks, the size of B2 precipitates for precipitation strengthening need to be controlled into small sizes (< 1 μm), and the interface between B2 and FCC phases is good to be tailored to be coherent instead of incoherent. Moreover, the SIMT occurred in the NiAl-type B2 phase is believed to be beneficial to fracture toughness, because it can relieve the stress concentration between B2 and FCC phases [225]. For the deformation twinning, it is beneficial to the improvement of the fatigue life, because the twin-dislocation interactions can bring out additional strengthening and lead to a cyclically-stable plastic deformation response. Thus, we need to control the factors that favor the formation of deformation nanotwins, such as the stacking fault energy (SFE), critical resolved shear stress, grain size, etc. Overall, cyclic-

deformation mechanisms favorable to fatigue life can be synergistically integrated for designing fatigue-resistant HEAs through rationally-tailoring the alloy composition and thermo-mechanical processing, considering HEAs' excellent microstructural controllability, as shown in Figure 6.7c.

6.5 Conclusions

In summary, the real-time LCF study on this HEA demonstrates that the deformation mechanisms that favor the improvement of fatigue behavior can be systematically integrated into HEAs due to their vast property-controlling microstructural choices, such as the plastically-deformable multicomponent precipitates, grains, interfaces, dislocations, twins, stacking faults, and SRO. The present work paves the way to design novel fatigue-resistant materials by means of the HEA concept.

CHAPTER VII

CONCLUSIONS

In this work, two main tasks have been studied for developing advanced precipitation-strengthened alloys by the HEA concept through integrated experimental and theoretical methods.

In the first task, in order to develop significantly cheaper and lighter high-temperature alloys than Ni-base superalloys, precipitation-strengthened body-centered-cubic (BCC) HEAs are designed, which possess a microstructure analogous to that of the γ/γ′ Ni-base superalloys, using the CALPHAD-based high-throughput computational method (HTCM). The fundamental understanding of the phase stability, precipitation-strengthening, and order-disorder-transition behaviors in the newly-designed lightweight HEAs have been revealed by *in-situ* neutron scattering, advanced microcopies, *ab initio* molecular dynamics (AIMD), and Monte-Carlo (MC) simulations. The insights obtained in this study offer a paradigm to develop high-performance lightweight HEAs via the high-throughput method.

In the second task, in order to develop advanced fatigue-resistant HEAs, a B2 precipitation-strengthened $Al_{0.5}CoCrFeNi$ HEA is designed, which exhibits the outperforming fatigue life at low strain amplitudes compared with traditional materials. Its real-time cyclic-deformation mechanisms are revealed by *in-situ* neutron diffraction and advanced microscopy experiments. The excellent fatigue life at low strain amplitudes is attributed to the retarded microcrack-initiation behavior resulting from the load redistribution and strain partitioning between FCC and B2 phases. This work indicates that

various beneficial cyclic-deformation mechanisms, such as the multicomponent-precipitation strengthening, deformation twinning, and reversible stress-induced martensitic phase transformation can be synergistically integrated into HEAs together. Guided by this design idea, fatigue-resistant HEAs can be developed, which can be generalized to other alloys systems.

CHAPTER VIII

FUTURE WORK

In the present work, many efforts have been made to develop advanced precipitation-strengthened HEAs for high-temperature and fatigue-resistant applications. However, some extra work still needs to be conducted in the future for accelerating the fundamental understanding and development of high-performance precipitation-strengthened HEAs, which are listed as follows.

(1) High-temperature deformation behavior of the newly-designed nanoscaled $L2_1$ precipitation-strengthened lightweight HEAs, such as high-temperature tension/compression and creep deformation behaviors;

(2) Nucleation and coarsening behaviors of the nanoscaled $L2_1$ precipitates within the BCC matrix of the newly-designed lightweight HEAs;

(3) The effects of minor additions of W, Ta, Nb, and Mo into the newly-designed $L2_1$ precipitation-strengthened lightweight HEAs on the high-temperature performance, deformation, and coarsening behaviors;

(4) Optimizations of the thermodynamic database of Al-Cr-Fe-Mn-Ti multicomponent system and alloy-design strategies for further improving strength and ductility;

(5) Improvement of low-cycle-fatigue performance based on the $Al_{0.5}$CoCrFeNi HEAs by tailoring the B2 precipitation behavior, such as morphology, size, and coherency, through rational thermo-mechanical processing and chemical composition tuning;

(6) In-situ thermograph and acoustic emission study of the low-cycle-fatigue behavior;

(7) Develop the crystal-plasticity finite element modeling (CPFEM) to simulate the low-cycle-fatigue deformation behavior of the precipitation-strengthened high-entropy alloys.

LIST OF REFERENCES

[1] B. Cantor, I. Chang, P. Knight, A. Vincent, Microstructural development in equiatomic multicomponent alloys, Materials Science and Engineering: A 375 (2004) 213-218.
[2] J.W. Yeh, S.K. Chen, S.J. Lin, J.Y. Gan, T.S. Chin, T.T. Shun, C.H. Tsau, S.Y. Chang, Nanostructured High-Entropy Alloys with Multiple Principal Elements: Novel Alloy Design Concepts and Outcomes, Advanced Engineering Materials 6(5) (2004) 299-303.
[3] Y. Zhang, T.T. Zuo, Z. Tang, M.C. Gao, K.A. Dahmen, P.K. Liaw, Z.P. Lu, Microstructures and Properties of High-entropy Alloys, Progress in Materials Science 61 (2014) 1-93.
[4] D.B. Miracle, O.N. Senkov, A critical review of high entropy alloys and related concepts, Acta Materialia 122 (2017) 448-511.
[5] E.P. George, D. Raabe, R.O. Ritchie, High-entropy alloys, Nature Reviews Materials 4(8) (2019) 515-534.
[6] Q. Ding, Y. Zhang, X. Chen, X. Fu, D. Chen, S. Chen, L. Gu, F. Wei, H. Bei, Y. Gao, M. Wen, J. Li, Z. Zhang, T. Zhu, R.O. Ritchie, Q. Yu, Tuning element distribution, structure and properties by composition in high-entropy alloys, Nature 574(7777) (2019) 223-227.
[7] Z. Li, K.G. Pradeep, Y. Deng, D. Raabe, C.C. Tasan, Metastable high-entropy dual-phase alloys overcome the strength–ductility trade-off, Nature 534 (2016) 227–230.
[8] T. Yang, Y.L. Zhao, Y. Tong, Z.B. Jiao, J. Wei, J.X. Cai, X.D. Han, D. Chen, A. Hu, J.J. Kai, K. Lu, Y. Liu, C.T. Liu, Multicomponent intermetallic nanoparticles and superb mechanical behaviors of complex alloys, Science 362(6417) (2018) 933-937.
[9] K.Y. Tsai, M.H. Tsai, J.W. Yeh, Sluggish diffusion in Co–Cr–Fe–Mn–Ni high-entropy alloys, Acta Materialia 61(13) (2013) 4887-4897.
[10] O. Senkov, G. Wilks, J. Scott, D. Miracle, Mechanical properties of Nb25Mo25Ta25W25 and V20Nb20Mo20Ta20W20 refractory high entropy alloys, Intermetallics 19(5) (2011) 698-706.
[11] Z. Lei, X. Liu, Y. Wu, H. Wang, S. Jiang, S. Wang, X. Hui, Y. Wu, B. Gault, P. Kontis, D. Raabe, L. Gu, Q. Zhang, H. Chen, H. Wang, J. Liu, K. An, Q. Zeng, T.-G. Nieh, Z. Lu, Enhanced strength and ductility in a high-entropy alloy via ordered oxygen complexes, Nature 563(7732) (2018) 546-550.
[12] F. Otto, A. Dlouhý, C. Somsen, H. Bei, G. Eggeler, E.P. George, The influences of temperature and microstructure on the tensile properties of a CoCrFeMnNi high-entropy alloy, Acta Materialia 61(15) (2013) 5743-5755.
[13] B. Gludovatz, A. Hohenwarter, D. Catoor, E.H. Chang, E.P. George, R.O. Ritchie, A fracture-resistant high-entropy alloy for cryogenic applications, Science 345(6201) (2014) 1153-1158.
[14] M. Hemphill, T. Yuan, G. Wang, J. Yeh, C. Tsai, A. Chuang, P. Liaw, Fatigue behavior of Al0.5CoCrCuFeNi high entropy alloys, Acta Materialia 60(16) (2012) 5723-5734.

[15] Z. Tang, T. Yuan, C.-W. Tsai, J.-W. Yeh, C.D. Lundin, P.K. Liaw, Fatigue behavior of a wrought Al 0.5 CoCrCuFeNi two-phase high-entropy alloy, Acta Materialia 99 (2015) 247-258.
[16] K.V. Thurston, B. Gludovatz, Q. Yu, G. Laplanche, E.P. George, R.O. Ritchie, Temperature and load-ratio dependent fatigue-crack growth in the CrMnFeCoNi high-entropy alloy, Journal of Alloys and Compounds 794 (2019) 525-533.
[17] K. Liu, S.S. Nene, M. Frank, S. Sinha, R.S. Mishra, Metastability-assisted fatigue behavior in a friction stir processed dual-phase high entropy alloy, Materials Research Letters 6(11) (2018) 613-619.
[18] Y. Shi, B. Yang, P. Liaw, Corrosion-resistant high-entropy alloys: A review, Metals 7(2) (2017) 43.
[19] Y. Shi, L. Collins, R. Feng, C. Zhang, N. Balke, P.K. Liaw, B. Yang, Homogenization of AlxCoCrFeNi high-entropy alloys with improved corrosion resistance, Corrosion Science 133 (2018) 120-131.
[20] G.W. Meetham, High-temperature materials - a general review, Journal of Materials Science 26(4) (1991) 853-860.
[21] R.C. Reed, The superalloys: fundamentals and applications, Cambridge university press2008.
[22] R. Feng, M. Gao, C. Lee, M. Mathes, T. Zuo, S. Chen, J. Hawk, Y. Zhang, P. Liaw, Design of light-weight high-entropy alloys, Entropy 18(9) (2016) 333.
[23] Y. Qiu, Y.J. Hu, A. Taylor, M.J. Styles, R.K.W. Marceau, A.V. Ceguerra, M.A. Gibson, Z.K. Liu, H.L. Fraser, N. Birbilis, A lightweight single-phase AlTiVCr compositionally complex alloy, Acta Materialia 123 (2017) 115-124.
[24] N. Stepanov, N.Y. Yurchenko, D. Skibin, M. Tikhonovsky, G. Salishchev, Structure and mechanical properties of the AlCr x NbTiV (x= 0, 0.5, 1, 1.5) high entropy alloys, Journal of Alloys and Compounds 652 (2015) 266-280.
[25] K.M. Youssef, A.J. Zaddach, C. Niu, D.L. Irving, C.C. Koch, A Novel Low-Density, High-Hardness, High-entropy Alloy with Close-packed Single-phase Nanocrystalline Structures, Materials Research Letters 3(2) (2015) 95-99.
[26] Z. Wu, H. Bei, G.M. Pharr, E.P. George, Temperature dependence of the mechanical properties of equiatomic solid solution alloys with face-centered cubic crystal structures, Acta Materialia 81 (2014) 428-441.
[27] S. Shukla, T. Wang, S. Cotton, R.S. Mishra, Hierarchical microstructure for improved fatigue properties in a eutectic high entropy alloy, Scripta Materialia 156 (2018) 105-109.
[28] C. Lu, L. Niu, N. Chen, K. Jin, T. Yang, P. Xiu, Y. Zhang, F. Gao, H. Bei, S. Shi, M.-R. He, I.M. Robertson, W.J. Weber, L. Wang, Enhancing radiation tolerance by controlling defect mobility and migration pathways in multicomponent single-phase alloys, Nature Communications 7 (2016) 13564.
[29] F. Granberg, K. Nordlund, M.W. Ullah, K. Jin, C. Lu, H. Bei, L.M. Wang, F. Djurabekova, W.J. Weber, Y. Zhang, Mechanism of Radiation Damage Reduction in Equiatomic Multicomponent Single Phase Alloys, Physical Review Letters 116(13) (2016) 135504.

[30] M. Seifi, D. Li, Z. Yong, P.K. Liaw, J.J. Lewandowski, Fracture Toughness and Fatigue Crack Growth Behavior of As-Cast High-Entropy Alloys, JOM (2015) 1-8.
[31] T. Niendorf, T. Wegener, Z. Li, D. Raabe, Unexpected cyclic stress-strain response of dual-phase high-entropy alloys induced by partial reversibility of deformation, Scripta Materialia 143 (2018) 63-67.
[32] F. Bahadur, K. Biswas, N.P. Gurao, Micro-mechanisms of Microstructural Damage due to Low Cycle Fatigue in CoCuFeMnNi High Entropy Alloy, International Journal of Fatigue (2019) 105258.
[33] P. Shi, W. Ren, T. Zheng, Z. Ren, X. Hou, J. Peng, P. Hu, Y. Gao, Y. Zhong, P.K. Liaw, Enhanced strength–ductility synergy in ultrafine-grained eutectic high-entropy alloys by inheriting microstructural lamellae, Nature Communications 10(1) (2019) 489.
[34] M.C. Gao, J.W. Yeh, P.K. Liaw, Y. Zhang, High-Entropy Alloys: Fundamentals and Applications, Springer, Cham, Switzerland, 2016.
[35] Y. Zhang, Y.J. Zhou, J.P. Lin, G.L. Chen, P.K. Liaw, Solid-Solution Phase Formation Rules for Multi-component Alloys, Advanced Engineering Materials 10(6) (2008) 534-538.
[36] R. Feng, P.K. Liaw, M.C. Gao, M. Widom, First-principles prediction of high-entropy-alloy stability, npj Computational Materials 3(1) (2017) 50.
[37] M.-H. Chuang, M.-H. Tsai, W.-R. Wang, S.-J. Lin, J.-W. Yeh, Microstructure and wear behavior of AlxCo 1.5 CrFeNi 1.5Tiy high-entropy alloys, Acta Materialia 59(16) (2011) 6308-6317.
[38] Y. Shi, B. Yang, P.K. Liaw, Corrosion-resistant high-entropy alloys: A review, Metals 7(2) (2017) 43.
[39] Y. Zhang, G.M. Stocks, K. Jin, C. Lu, H. Bei, B.C. Sales, L. Wang, L.K. Béland, R.E. Stoller, G.D. Samolyuk, Influence of chemical disorder on energy dissipation and defect evolution in concentrated solid solution alloys, Nature Communications 6 (2015) 8736.
[40] Y. Jien-Wei, Recent progress in high entropy alloys, Ann. Chim. Sci. Mat 31(6) (2006) 633-648.
[41] H.S. Oh, S.J. Kim, K. Odbadrakh, W.H. Ryu, K.N. Yoon, S. Mu, F. Körmann, Y. Ikeda, C.C. Tasan, D. Raabe, T. Egami, E.S. Park, Engineering atomic-level complexity in high-entropy and complex concentrated alloys, Nature Communications 10(1) (2019) 2090.
[42] C. Lee, G. Song, M.C. Gao, R. Feng, P. Chen, J. Brechtl, Y. Chen, K. An, W. Guo, J.D. Poplawsky, S. Li, A.T. Samaei, W. Chen, A. Hu, H. Choo, P.K. Liaw, Lattice distortion in a strong and ductile refractory high-entropy alloy, Acta Materialia 160 (2018) 158-172.
[43] K.-Y. Tsai, M.-H. Tsai, J.-W. Yeh, Reply to comments on "Sluggish diffusion in Co-Cr-Fe-Mn-Ni high-entropy alloys" by K.Y. Tsai, M.H. Tsai and J.W. Yeh, Acta Materialia 61 (2013) 4887-4897, Scripta Materialia 135(Supplement C) (2017) 158-159.

[44] A. Paul, Comments on “Sluggish diffusion in Co–Cr–Fe–Mn–Ni high-entropy alloys” by K.Y. Tsai, M.H. Tsai and J.W. Yeh, Acta Materialia 61 (2013) 4887–4897, Scripta Materialia 135(Supplement C) (2017) 153-157.
[45] D.B. Miracle, Critical Assessment 14: High entropy alloys and their development as structural materials, Materials Science and Technology 31(10) (2015) 1142-1147.
[46] Y. Lu, X. Gao, L. Jiang, Z. Chen, T. Wang, J. Jie, H. Kang, Y. Zhang, S. Guo, H. Ruan, Y. Zhao, Z. Cao, T. Li, Directly cast bulk eutectic and near-eutectic high entropy alloys with balanced strength and ductility in a wide temperature range, Acta Materialia 124 (2017) 143-150.
[47] I. Wani, T. Bhattacharjee, S. Sheikh, Y. Lu, S. Chatterjee, P. Bhattacharjee, S. Guo, N. Tsuji, Ultrafine-grained AlCoCrFeNi2. 1 eutectic high-entropy alloy, Materials Research Letters (2016) 1-6.
[48] Y. Lu, Y. Dong, S. Guo, L. Jiang, H. Kang, T. Wang, B. Wen, Z. Wang, J. Jie, Z. Cao, A promising new class of high-temperature alloys: eutectic high-entropy alloys, Scientific reports 4 (2014).
[49] H. Gleiter, E. Hornbogen, Precipitation hardening by coherent particles, Materials Science and Engineering 2(6) (1968) 285-302.
[50] J. He, H. Wang, H. Huang, X. Xu, M. Chen, Y. Wu, X. Liu, T. Nieh, K. An, Z. Lu, A precipitation-hardened high-entropy alloy with outstanding tensile properties, Acta Materialia 102 (2016) 187-196.
[51] Q. Wang, Y. Ma, B. Jiang, X. Li, Y. Shi, C. Dong, P.K. Liaw, A cuboidal B2 nanoprecipitation-enhanced body-centered-cubic alloy Al0.7CoCrFe2Ni with prominent tensile properties, Scripta Materialia 120 (2016) 85-89.
[52] R. Feng, M.C. Gao, C. Zhang, W. Guo, J.D. Poplawsky, F. Zhang, J.A. Hawk, J.C. Neuefeind, Y. Ren, P.K. Liaw, Phase stability and transformation in a light-weight high-entropy alloy, Acta Materialia 146 (2018) 280-293.
[53] O.N. Senkov, J.K. Jensen, A.L. Pilchak, D.B. Miracle, H.L. Fraser, Compositional variation effects on the microstructure and properties of a refractory high-entropy superalloy AlMo0.5NbTa0.5TiZr, Materials & Design 139 (2018) 498-511.
[54] K. Ming, X. Bi, J. Wang, Realizing strength-ductility combination of coarse-grained Al0.2Co1.5CrFeNi1.5Ti0.3 alloy via nano-sized, coherent precipitates, International Journal of Plasticity 100 (2018) 177-191.
[55] D.A. Porter, K.E. Easterling, M. Sherif, Phase Transformations in Metals and Alloys, (Revised Reprint), CRC press2009.
[56] Y.Y. Zhao, H.W. Chen, Z.P. Lu, T.G. Nieh, Thermal stability and coarsening of coherent particles in a precipitation-hardened (NiCoFeCr)94Ti2Al4 high-entropy alloy, Acta Materialia 147 (2018) 184-194.
[57] J.S. Van Sluytman, T.M. Pollock, Optimal precipitate shapes in nickel-base γ–γ′ alloys, Acta Materialia 60(4) (2012) 1771-1783.
[58] P.W. Voorhees, G.B. McFadden, W.C. Johnson, On the morphological development of second-phase particles in elastically-stressed solids, Acta Metallurgica et Materialia 40(11) (1992) 2979-2992.
[59] Y. Ma, Q. Wang, B.B. Jiang, C.L. Li, J.M. Hao, X.N. Li, C. Dong, T.G. Nieh, Controlled formation of coherent cuboidal nanoprecipitates in body-centered cubic

high-entropy alloys based on Al2(Ni,Co,Fe,Cr)14 compositions, Acta Materialia 147 (2018) 213-225.
[60] J.K. Jensen, B.A. Welk, R.E.A. Williams, J.M. Sosa, D.E. Huber, O.N. Senkov, G.B. Viswanathan, H.L. Fraser, Characterization of the microstructure of the compositionally complex alloy Al1Mo0.5Nb1Ta0.5Ti1Zr1, Scripta Materialia 121 (2016) 1-4.
[61] H. Diao, D. Ma, R. Feng, T. Liu, C. Pu, C. Zhang, W. Guo, J.D. Poplawsky, Y. Gao, P.K. Liaw, Novel NiAl-strengthened high entropy alloys with balanced tensile strength and ductility, Materials Science and Engineering: A 742 (2019) 636-647.
[62] A. Ardell, Precipitation hardening, Metallurgical Transactions A 16(12) (1985) 2131-2165.
[63] S. Liu, M. Gao, P. Liaw, Y. Zhang, Microstructures and mechanical properties of AlxCrFeNiTi 0.25 alloys, Journal of Alloys and Compounds 619 (2015) 610-615.
[64] N. Stepanov, D. Shaysultanov, G. Salishchev, M. Tikhonovsky, Structure and mechanical properties of a light-weight AlNbTiV high entropy alloy, Materials Letters 142 (2015) 153-155.
[65] N. Stepanov, N.Y. Yurchenko, D. Shaysultanov, G. Salishchev, M. Tikhonovsky, Effect of Al on structure and mechanical properties of AlxNbTiVZr (x= 0, 0.5, 1, 1.5) high entropy alloys, Materials Science and Technology 31(10) (2015) 1184-1193.
[66] O. Senkov, S. Senkova, D. Miracle, C. Woodward, Mechanical properties of low-density, refractory multi-principal element alloys of the Cr–Nb–Ti–V–Zr system, Materials Science and Engineering: A 565 (2013) 51-62.
[67] O. Senkov, S. Senkova, C. Woodward, D. Miracle, Low-density, refractory multi-principal element alloys of the Cr–Nb–Ti–V–Zr system: Microstructure and phase analysis, Acta Materialia 61(5) (2013) 1545-1557.
[68] H. Chen, A. Kauffmann, B. Gorr, D. Schliephake, C. Seemüller, J. Wagner, H.-J. Christ, M. Heilmaier, Microstructure and mechanical properties at elevated temperatures of a new Al-containing refractory high-entropy alloy Nb-Mo-Cr-Ti-Al, Journal of Alloys and Compounds 661 (2016) 206-215.
[69] O. Senkov, C. Woodward, D. Miracle, Microstructure and properties of aluminum-containing refractory high-entropy alloys, JOM 66(10) (2014) 2030-2042.
[70] X. Yang, Y. Zhang, Prediction of high-entropy stabilized solid-solution in multi-component alloys, Materials Chemistry and Physics 132(2) (2012) 233-238.
[71] S. Guo, C. Ng, J. Lu, C. Liu, Effect of valence electron concentration on stability of fcc or bcc phase in high entropy alloys, Journal of Applied Physics 109(10) (2011) 103505.
[72] M.C. Troparevsky, J.R. Morris, P.R. Kent, A.R. Lupini, G.M. Stocks, Criteria for Predicting the Formation of Single-Phase High-Entropy Alloys, Physical Review X 5(1) (2015) 011041.
[73] Y. Ye, Q. Wang, J. Lu, C. Liu, Y. Yang, Design of high entropy alloys: A single-parameter thermodynamic rule, Scripta Materialia 104 (2015) 53-55.
[74] D. King, S. Middleburgh, A. McGregor, M. Cortie, Predicting the formation and stability of single phase high-entropy alloys, Acta Materialia 104 (2016) 172-179.

[75] M. Poletti, L. Battezzati, Electronic and thermodynamic criteria for the occurrence of high entropy alloys in metallic systems, Acta Materialia 75 (2014) 297-306.
[76] M.C. Gao, D.E. Alman, Searching for next single-phase high-entropy alloy compositions, Entropy 15(10) (2013) 4504-4519.
[77] Y. Ye, Q. Wang, J. Lu, C. Liu, Y. Yang, The generalized thermodynamic rule for phase selection in multicomponent alloys, Intermetallics 59 (2015) 75-80.
[78] Z. Wang, W. Qiu, Y. Yang, C. Liu, Atomic-size and lattice-distortion effects in newly developed high-entropy alloys with multiple principal elements, Intermetallics 64 (2015) 63-69.
[79] Z. Wang, Y. Huang, Y. Yang, J. Wang, C. Liu, Atomic-size effect and solid solubility of multicomponent alloys, Scripta Materialia 94 (2015) 28-31.
[80] M.C. Gao, Chapter 11: Design of High-Entropy Alloys, in: M.C. Gao, J.W. Yeh, P.K. Liaw, Y. Zhang (Eds.), High-Entropy Alloys: Fundamentals and Applications, Springer International Publishing, Cham, Switzerland, 2016.
[81] M.C. Gao, C.S. Carney, Ö.N. Doğan, P.D. Jablonksi, J.A. Hawk, D.E. Alman, Design of Refractory High-Entropy Alloys, Jom 67(11) (2015) 2653-2669.
[82] M.C. Gao, B. Zhang, S.M. Guo, J.W. Qiao, J.A. Hawk, High-entropy alloys in hexagonal close packed structure, Metallurgical and Materials Transactions A doi: 10.1007/s11661-015-3091-1 (2015).
[83] Y. Zhang, Z.P. Lu, S.G. Ma, P.K. Liaw, Z. Tang, Y.Q. Cheng, M.C. Gao, Guidelines in predicting phase formation of high-entropy alloys, MRS Communications 4(02) (2014) 57-62.
[84] V.H. Hammond, M.A. Atwater, K.A. Darling, H.Q. Nguyen, L.J. Kecskes, Equal-channel angular extrusion of a low-density high-entropy alloy produced by high-energy cryogenic mechanical alloying, JOM 66(10) (2014) 2021-2029.
[85] X. Yang, S. Chen, J. Cotton, Y. Zhang, Phase stability of low-density, multiprincipal component alloys containing aluminum, magnesium, and lithium, JOM 66(10) (2014) 2009-2020.
[86] R. Li, J.C. Gao, K. Fan, Microstructure and mechanical properties of MgMnAlZnCu high entropy alloy cooling in three conditions, Materials Science Forum, Trans Tech Publ, 2011, pp. 235-241.
[87] Y. Zhang, Z. Lu, S. Ma, P. Liaw, Z. Tang, Y. Cheng, M. Gao, Guidelines in predicting phase formation of high-entropy alloys, MRS Communications 4(02) (2014) 57-62.
[88] M. Widom, W.P. Huhn, S. Maiti, W. Steurer, Hybrid Monte Carlo/Molecular Dynamics Simulation of a Refractory Metal High Entropy Alloy, Metallurgical and Materials Transactions A 45A(1) (2014) 196-200.
[89] M. Widom, Chapter 8: Prediction of structure and phase transformations, in: M.C. Gao, J.W. Yeh, P.K. Liaw, Y. Zhang (Eds.), High-Entropy Alloys: Fundamentals and Applications, Springer, Cham, Switzerland, 2016.
[90] M.C. Gao, C. Niu, C. Jiang, D.L. Irving, Chapter 10: Applications of Special Quasi-Random Structures to High-Entropy Alloys, in: M.C. Gao, J.W. Yeh, P.K. Liaw, Y. Zhang (Eds.), High-Entropy Alloys: Fundamentals and Applications, Springer International Publishing, Cham, Switzerland, 2016.

[91] F.R. De Boer, W. Mattens, R. Boom, A. Miedema, A. Niessen, Cohesion in metals, (1988).
[92] D.J.M. King, Alloy Search and Predict. www.alloyASAP.com, 2016).
[93] O. Senkov, G. Wilks, D. Miracle, C. Chuang, P. Liaw, Refractory high-entropy alloys, Intermetallics 18(9) (2010) 1758-1765.
[94] A. Takeuchi, K. Amiya, T. Wada, K. Yubuta, W. Zhang, High-entropy alloys with a hexagonal close-packed structure designed by equi-atomic alloy strategy and binary phase diagrams, JOM 66(10) (2014) 1984-1992.
[95] Y.J. Zhao, J.W. Qiao, S.G. Ma, M.C. Gao, H.J. Yang, M.W. Chen, Y. Zhang, A hexagonal close-packed high-entropy alloy: the effect of entropy, Materials & Design 96 (2016) 10-15.
[96] M. Feuerbacher, M. Heidelmann, C. Thomas, Hexagonal high-entropy alloys, Materials Research Letters 3(1) (2015) 1-6.
[97] Y.-F. Kao, T.-J. Chen, S.-K. Chen, J.-W. Yeh, Microstructure and mechanical property of as-cast,-homogenized, and-deformed Al x CoCrFeNi (0≤ x≤ 2) high-entropy alloys, Journal of Alloys and Compounds 488(1) (2009) 57-64.
[98] Y.D. Wu, Y.H. Cai, T. Wang, J.J. Si, J. Zhu, Y.D. Wang, X.D. Hui, A refractory Hf25Nb25Ti25Zr25 high-entropy alloy with excellent structural stability and tensile properties, Materials Letters 130 (2014) 277-280.
[99] O. Senkov, J. Scott, S. Senkova, F. Meisenkothen, D. Miracle, C. Woodward, Microstructure and elevated temperature properties of a refractory TaNbHfZrTi alloy, Journal of Materials Science 47(9) (2012) 4062-4074.
[100] B. Sundman, B. Jansson, J.-O. Andersson, The thermo-calc databank system, Calphad 9(2) (1985) 153-190.
[101] B. Zhang, M.C. Gao, Y. Zhang, S. Yang, S.M. Guo, Senary Refractory High-Entropy Alloy MoNbTaTiVW, Materials Science Technology 31 (2015) 1207-1213.
[102] B. Zhang, M.C. Gao, Y. Zhang, S.M. Guo, Senary Refractory High-Entropy Alloy Cr_xMoNbTaVW, Calphad 51 (2015) 193-201.
[103] M.C. Gao, B. Zhang, S. Yang, S.M. Guo, Senary Refractory High-Entropy Alloy HfNbTaTiVZr, Metallurgical and Materials Transactions A doi: 10.1007/s11661-015-3105-z (2015).
[104] H.W. Yao, J.W. Qiao, M.C. Gao, J.A. Hawk, S.G. Ma, H.F. Zhou, Y. Zhang, NbTaV-(Ti,W) refractory high-entropy alloys: Experiments and modeling, Materials Science and Engineering: A 674 (2016) 203-211.
[105] C. Zhang, F. Zhang, S. Chen, W. Cao, Computational thermodynamics aided high-entropy alloy design, Jom 64(7) (2012) 839-845.
[106] F. Zhang, C. Zhang, S. Chen, J. Zhu, W. Cao, U. Kattner, An understanding of high entropy alloys from phase diagram calculations, Calphad 45 (2014) 1-10.
[107] C. Zhang, F. Zhang, H. Diao, M.C. Gao, Z. Tang, J.D. Poplawsky, P.K. Liaw, Understanding phase stability of Al-Co-Cr-Fe-Ni high entropy alloys, Materials & Design 109 (2016) 425-433.
[108] G.H. Gulliver, The quantitative effect of rapid cooling upon the constitution of binary alloys, Journal of Institue of Metals 9 (1913) 120-157.
[109] E. Scheil, Comments on the layer crystal formation, Z. Metallkd. 34 (1942) 70-72.

[110] F. Tian, Y. Wang, D.L. L. Irving, L. Vitos, Chapter 9: Applications of Coherent Potential Approximation to HEAs, in: M.C. Gao, J.W. Yeh, P.K. Liaw, Y. Zhang (Eds.), High-Entropy Alloys: Fundamentals and Applications, Springer, Cham, Switzerland, 2016.
[111] O. Senkov, D. Miracle, A new thermodynamic parameter to predict formation of solid solution or intermetallic phases in high entropy alloys, Journal of Alloys and Compounds 658 (2016) 603-607.
[112] Z. Zhang, M. Mao, J. Wang, B. Gludovatz, Z. Zhang, S.X. Mao, E.P. George, Q. Yu, R.O. Ritchie, Nanoscale origins of the damage tolerance of the high-entropy alloy CrMnFeCoNi, Nature Communications 6 (2015) 10143.
[113] Y. Zou, H. Ma, R. Spolenak, Ultrastrong ductile and stable high-entropy alloys at small scales, Nature Communications 6 (2015) 7748.
[114] H.Y. Diao, R. Feng, K.A. Dahmen, P.K. Liaw, Fundamental deformation behavior in high-entropy alloys: An overview, Current Opinion in Solid State and Materials Science 21(5) (2017) 252-266.
[115] L.J. Santodonato, Y. Zhang, M. Feygenson, C.M. Parish, M.C. Gao, R.J. Weber, J.C. Neuefeind, Z. Tang, P.K. Liaw, Deviation from high-entropy configurations in the atomic distributions of a multi-principal-element alloy, Nature Communications 6 (2015) 5964.
[116] R. Krein, M. Palm, M. Heilmaier, Characterization of microstructures, mechanical properties, and oxidation behavior of coherent A2+ L21 Fe-Al-Ti, Journal of Materials Research 24(11) (2009) 3412-3421.
[117] P.R. Alonso, P.H. Gargano, P.B. Bozzano, G.E. Ramírez-Caballero, P.B. Balbuena, G.H. Rubiolo, Combined ab initio and experimental study of A2 + L21 coherent equilibria in the Fe–Al–X (X = Ti, Nb, V) systems, Intermetallics 19(8) (2011) 1157-1167.
[118] P. Strutt, R. Polvani, J. Ingram, Creep behavior of the heusler type structure alloy Ni2AlTi, Metallurgical Transactions A 7(1) (1976) 23-31.
[119] G. Song, Z. Sun, L. Li, X. Xu, M. Rawlings, C.H. Liebscher, B. Clausen, J. Poplawsky, D.N. Leonard, S. Huang, Ferritic Alloys with Extreme Creep Resistance via Coherent Hierarchical Precipitates, Scientific reports 5 (2015).
[120] G. Song, Z. Sun, J.D. Poplawsky, Y. Gao, P.K. Liaw, Microstructural evolution of single Ni2TiAl or hierarchical NiAl/Ni2TiAl precipitates in Fe-Ni-Al-Cr-Ti ferritic alloys during thermal treatment for elevated-temperature applications, Acta Materialia 127 (2017) 1-16.
[121] J. Neuefeind, M. Feygenson, J. Carruth, R. Hoffmann, K.K. Chipley, The nanoscale ordered materials diffractometer NOMAD at the spallation neutron source SNS, Nuclear Instruments and Methods in Physics Research Section B: Beam Interactions with Materials and Atoms 287 (2012) 68-75.
[122] J.R. Weber, J.J. Felten, B. Cho, P.C. Nordine, Glass fibres of pure and erbium-or neodymium-doped yttria-alumina compositions, Nature 393(6687) (1998) 769.
[123] K. Thompson, D. Lawrence, D.J. Larson, J.D. Olson, T.F. Kelly, B. Gorman, In situ site-specific specimen preparation for atom probe tomography, Ultramicroscopy 107(2) (2007) 131-139.

[124] G. Wei, A.G. David, D.T. Julie, H. Daniel, A.Y. George, D.P. Jonathan, An atom probe perspective on phase separation and precipitation in duplex stainless steels, Nanotechnology 27(25) (2016) 254004.
[125] M. Miller, K. Russell, Performance of a local electrode atom probe, Surface and Interface Analysis 39(2-3) (2007) 262-267.
[126] T. Pandat, Thermodynamic Calculations and Kinetic Simulations, CompuTherm LLC, Madison, WI, USA–53719.
[127] G. Kresse, J. Hafner, Ab initio molecular dynamics for liquid metals, Physical Review B 47(1) (1993) 558.
[128] G. Kresse, J. Furthmüller, Efficient iterative schemes for ab initio total-energy calculations using a plane-wave basis set, Physical Review B 54(16) (1996) 11169.
[129] P.E. Blochl, Projector augmented-wave method, Physical Review B 50(24) (1994) 17953.
[130] J.P. Perdew, A. Ruzsinszky, G.I. Csonka, O.A. Vydrov, G.E. Scuseria, L.A. Constantin, X.L. Zhou, K. Burke, Restoring the density-gradient expansion for exchange in solids and surfaces, Physical Review Letters 100(13) (2008) 136406.
[131] L. Verlet, Computer experiments on classical fluids .i. Thermodynamical properties of lennard-jones molecules, Physical Review 159(1) (1967) 98.
[132] S. Nose, a unified formulation of the constant temperature molecular-dynamics methods, Journal of Chemical Physics 81(1) (1984) 511-519.
[133] J.P. Perdew, K. Burke, M. Ernzerhof, Generalized Gradient Approximation Made Simple, Physical Review Letters 77 (1996) 3865-3868.
[134] H.J. Monkhorst, J.D. Pack, Special points for brillouin-zone integrations, Physical Review B 13(12) (1976) 5188.
[135] M. Methfessel, A.T. Paxton, High-precision sampling for Brillouin-zone integration in metals, Physical Review B 40(6) (1989) 3616.
[136] A. Ardell, R. Nicholson, On the modulated structure of aged Ni-Al alloys: with an Appendix On the elastic interaction between inclusions by JD Eshelby‡‡ Cavendish Laboratory, University of Cambridge, England, Acta metallurgica 14(10) (1966) 1295-1309.
[137] J. Langer, M. Bar-On, H.D. Miller, New computational method in the theory of spinodal decomposition, Physical Review A 11(4) (1975) 1417.
[138] W.C. Johnson, J.W. Cahn, Elastically induced shape bifurcations of inclusions, Acta Metallurgica 32(11) (1984) 1925-1933.
[139] M.C. Gao, D.E. Alman, Searching for next single-phase high-entropy alloy compositions, Entropy 15 (2013) 4504-4519.
[140] P. Ganesh, M. Widom, Ab initio simulations of geometrical frustration in supercooled liquid Fe and Fe-based metallic glass, Phys. Rev. B 77(1) (2008) 014205.
[141] M.C. Gao, Design of High-Entropy Alloys, in: M.C. Gao, J.W. Yeh, P.K. Liaw, Y. Zhang (Eds.), High-Entropy Alloys: Fundamentals and Applications, Springer International Publishing, Cham, Switzerland, 2016, pp. 369-398.
[142] M.C. Gao, B. Zhang, S. Yang, S.M. Guo, Senary Refractory High-Entropy Alloy HfNbTaTiVZr, Metallurgical and Materials Transactions A 47A (2016) 3333-3345.

[143] M.C. Gao, B. Zhang, S.M. Guo, J.W. Qiao, J.A. Hawk, High-Entropy Alloys in Hexagonal Close Packed Structure, Metallurgical and Materials Transactions A 47A (2016) 3322-3332.
[144] M. Palm, G. Inden, N. Thomas, The Fe-A1-Ti system, Journal of Phase Equilibria 16(3) (1995) 209-222.
[145] M. Palm, J. Lacaze, Assessment of the Al–Fe–Ti system, Intermetallics 14(10) (2006) 1291-1303.
[146] D. De Fontaine, An analysis of clustering and ordering in multicomponent solid solutions—I. Stability criteria, Journal of Physics and Chemistry of Solids 33(2) (1972) 297-310.
[147] S. Jiang, H. Wang, Y. Wu, X. Liu, H. Chen, M. Yao, B. Gault, D. Ponge, D. Raabe, A. Hirata, M. Chen, Y. Wang, Z. Lu, Ultrastrong steel via minimal lattice misfit and high-density nanoprecipitation, Nature 544(7651) (2017) 460-464.
[148] A.G. Khachaturyan, Theory of structural transformations in solids, Courier Corporation2013.
[149] J.D. Eshelby, The determination of the elastic field of an ellipsoidal inclusion, and related problems, Proceedings of the Royal Society of London A: Mathematical, Physical and Engineering Sciences, The Royal Society, 1957, pp. 376-396.
[150] S. Yeom, D. Yoon, M. Henry, The morphological changes ofγ′ precipitates in a Ni-8Al (wt pct) alloy during their coarsening, Metallurgical Transactions A 24(9) (1993) 1975-1981.
[151] L.A. Bendersky, P.W. Voorhees, W.J. Boettinger, W.C. Johnson, The role of elastic energy in the morphological development of a NiTiAl alloy, Scripta Metallurgica 22(7) (1988) 1029-1034.
[152] J. Jung, G. Ghosh, D. Isheim, G. Olson, Precipitation of Heusler Phase (Ni2TiAl) from B2-TiNi in Ni-Ti-Al and Ni-Ti-Al-X (X= Hf, Zr) Alloys, Metallurgical and Materials Transactions A 34(6) (2003) 1221-1235.
[153] H. Aaronson, F. LeGoues, An assessment of studies on homogeneous diffusional nucleation kinetics in binary metallic alloys, Metallurgical transactions A 23(7) (1992) 1915-1945.
[154] W.C. Johnson, P. Voorhees, Elastic interaction and stability of misfitting cuboidal inhomogeneities, Journal of Applied Physics 61(4) (1987) 1610-1619.
[155] A. Khachaturyan, S. Semenovskaya, J. Morris, Theoretical analysis of strain-induced shape changes in cubic precipitates during coarsening, Acta Metallurgica 36(6) (1988) 1563-1572.
[156] C.H. Su, P.W. Voorhees, The dynamics of precipitate evolution in elastically stressed solids—II. Particle alignment, Acta Materialia 44(5) (1996) 2001-2016.
[157] http://www.specialmetals.com/assets/smc/documents/inconel_alloy_718.pdf.).
[158] Z. Sun, C.H. Liebscher, S. Huang, Z. Teng, G. Song, G. Wang, M. Asta, M. Rawlings, M.E. Fine, P.K. Liaw, New design aspects of creep-resistant NiAl-strengthened ferritic alloys, Scripta Materialia 68(6) (2013) 384-388.
[159] G. Song, Z. Sun, L. Li, B. Clausen, S.Y. Zhang, Y. Gao, P.K. Liaw, High temperature deformation mechanism in hierarchical and single precipitate strengthened ferritic alloys by in situ neutron diffraction studies, Scientific Reports 7 (2017) 45965.

[160] Y.A. Chang, S.L. Chen, F. Zhang, X.Y. Yan, F.Y. Xie, R. Schmid-Fetzer, W.A. Oates, Phase diagram calculation: past, present and future, Progress in Materials Science 49 (2004) 313-345.
[161] G.B. Olson, C.J. Kuehmann, Materials genomics: From CALPHAD to flight, Scripta Materialia 70 (2014) 25-30.
[162] J.M. Rickman, H.M. Chan, M.P. Harmer, J.A. Smeltzer, C.J. Marvel, A. Roy, G. Balasubramanian, Materials informatics for the screening of multi-principal elements and high-entropy alloys, Nature Communications 10(1) (2019) 2618.
[163] F.G. Coury, K.D. Clarke, C.S. Kiminami, M.J. Kaufman, A.J. Clarke, High throughput discovery and design of strong multicomponent metallic solid solutions, Scientific Reports 8(1) (2018) 8600.
[164] M. Hillert, Phase Transformations, ASM, Cleveland, OH, 1968.
[165] L. Kaufman, H. Bernstein, Computer Calculation of Phase Diagrams, Academic Press, New York, 1970.
[166] Y.A. Chang, Phase diagram calculations in teaching, research, and industry, Metall. Trans. B 37B (2006) 7-39.
[167] U.R. Kattner, The CALPHAD method and its role in material and process development, Tecnol Metal Mater Min. 13(1) (2016) 3-15.
[168] National Research Council, Committee on Integrated Computational Materials Engineering. Integrated Computational Materials Engineering: A Transformational Discipline for Improved Competitiveness and National Security, National Academic Press, Washington, DC, 2008.
[169] Office of Science and Technology Policy, Materials Genome Initiative for global competitiveness, Washington, DC, 2011.
[170] Pandat^{TM}, Thermodynamic Calculations and Kinetic Simulations, CompuTherm LLC, Middleton, WI - 53562.
[171] Thermo-Calc, Thermodynamic Equilibrium Calculations, Thermo-Calc Software, Stockholm, Sweden.
[172] FactSage, Thermochemical Software, Montreal, Canada.
[173] C. Zhang, M.C. Gao, CALPHAD Modeling of High-Entropy Alloys, in: M.C. Gao, J.-W. Yeh, P.K. Liaw, Y. Zhang (Eds.), High-Entropy Alloys - Fundamentals and Applications, Springer International Publishing, Switzerland, 2016, p. 536.
[174] D.B. Miracle, J.D. Miller, O.N. Senkov, C. Woodward, M.D. Uchic, J. Tiley, Exploration and Development of High Entropy Alloys for Structural Applications, Entropy 16(1) (2014) 494-525.
[175] F. Zhang, C. Zhang, S.L. Chen, J. Zhu, W.S. Cao, U.R. Kattner, An understanding of high entropy alloys from phase diagram calculations, Calphad 45 (2014) 1-10.
[176] D.C. Ma, M.J. Yao, K.G. Pradeep, C.C. Tasan, H. Springer, D. Raabe, Phase stability of non-equiatomic CoCrFeMnNi high entropy alloys, Acta Materialia 98(1) (2015) 288-296.
[177] K. An, VDRIVE- Data Reduction and Interactive Visualization Software for Event Mode Neutron Diffraction, ORNL Report, Oak Ridge National Laboratory, ORNL-TM-2012-621, (2012).

[178] T. Egami, S.J. Billinge, Underneath the Bragg peaks: structural analysis of complex materials, Elsevier2003.
[179] C.L. Farrow, P. Juhas, J.W. Liu, D. Bryndin, E.S. Božin, J. Bloch, P. Th, S.J.L. Billinge, PDFfit2 and PDFgui: computer programs for studying nanostructure in crystals, Journal of Physics: Condensed Matter 19(33) (2007) 335219.
[180] G. Kresse, J. Hafner, Ab initio molecular dynamics for liquid metals, Physical Review B 47(1) (1993) 558-561.
[181] G. Kresse, J. Furthmüller, Efficient iterative schemes for ab initio total-energy calculations using a plane-wave basis set, Physical Review B 54(16) (1996) 11169-11186.
[182] L. Verlet, Computer "Experiments" on Classical Fluids. I. Thermodynamical Properties of Lennard-Jones Molecules, Physical Review B 159(1) (1967) 98-103.
[183] S. Nosé, A unified formulation of the constant temperature molecular dynamics methods, The Journal of Chemical Physics 81(1) (1984) 511.
[184] P.E. Blöchl, Projector augmented-wave method, Physical Review B 50(24) (1994) 17953-17979.
[185] J.P. Perdew, A. Ruzsinszky, G.I. Csonka, O.A. Vydrov, G.E. Scuseria, L.A. Constantin, X. Zhou, K. Burke, Restoring the density-gradient expansion for exchange in solids and surfaces, Physical Review Letters 100(13) (2008) 136406.
[186] L.J. Santodonato, P.K. Liaw, R.R. Unocic, H. Bei, J.R. Morris, Predictive multiphase evolution in Al-containing high-entropy alloys, Nature Communications 9(1) (2018) 4520.
[187] C.-J. Tong, Y.-L. Chen, J.-W. Yeh, S.-J. Lin, S.-K. Chen, T.-T. Shun, C.-H. Tsau, S.-Y. Chang, Microstructure characterization of Al x CoCrCuFeNi high-entropy alloy system with multiprincipal elements, Metallurgical and Materials Transactions A 36(4) (2005) 881-893.
[188] Z. Pei, M. Eisenbach, S. Mu, G.M. Stocks, Error controlling of the combined Cluster-Expansion and Wang–Landau Monte-Carlo method and its application to FeCo, Computer Physics Communications 235 (2019) 95-101.
[189] M. Eisenbach, Z. Pei, X. Liu, First-principles study of order-disorder transitions in multicomponent solid-solution alloys, Journal of Physics: Condensed Matter 31(27) (2019) 273002.
[190] S. Curtarolo, W. Setyawan, S. Wang, J. Xue, K. Yang, R.H. Taylor, L.J. Nelson, G.L. Hart, S. Sanvito, M. Buongiorno-Nardelli, AFLOWLIB. ORG: A distributed materials properties repository from high-throughput ab initio calculations, Computational Materials Science 58 (2012) 227-235.
[191] O.N. Senkov, J.D. Miller, D.B. Miracle, C. Woodward, Accelerated exploration of multi-principal element alloys with solid solution phases, Nature Communications 6 (2015) 6529.
[192] V.I. Dobatkin, G.I. Eskin, Nondendritic structure in ingots of light alloys, Tsvetnve Metallv. 12 (1991) 64-67.
[193] L.S. Toropova, D.G. Eskin, M.L. Kharakterova, T.V. Dobatkina, Advanced Aluminum Alloys Containing Scandium, Taylor & Francis, 2 Park Square, Milton Park, Abingdon, Oxon, OX14 4RN, 1998.

[194] C. Stallybrass, G. Sauthoff, Ferritic Fe–Al–Ni–Cr alloys with coherent precipitates for high-temperature applications, Materials Science and Engineering: A 387-389 (2004) 985-990.
[195] Y. Zhou, X. Jin, L. Zhang, X. Du, B. Li, A hierarchical nanostructured Fe34Cr34Ni14Al14Co4 high-entropy alloy with good compressive mechanical properties, Materials Science and Engineering: A 716 (2018) 235-239.
[196] D.G. Shaysultanov, G.A. Salishchev, Y.V. Ivanisenko, S.V. Zherebtsov, M.A. Tikhonovsky, N.D. Stepanov, Novel Fe36Mn21Cr18Ni15Al10 high entropy alloy with bcc/B2 dual-phase structure, Journal of Alloys and Compounds 705(Supplement C) (2017) 756-763.
[197] D.G. Morris, S. Gunther, Room and high temperature mechanical behaviour of a Fe3Al-based alloy with α-α″ microstructure, Acta Materialia 45(2) (1997) 811-822.
[198] B.E. Warren, X-ray Diffraction, Courier Corporation1990.
[199] D.B. Miracle, High entropy alloys and their development as structural materials, Materials Science and Technology 31(10) (2015) 1142-1147.
[200] O.N. Senkov, J.D. Miller, D.B. Miracle, C. Woodward, Accelerated exploration of multi-principal element alloys for structural applications, Calphad 50 (2015) 32-48.
[201] F. Tancret, I. Toda-Caraballo, E. Menou, P.E.J. Rivera-Díaz-Del-Castillo, Designing high entropy alloys employing thermodynamics and Gaussian process statistical analysis, Materials & Design 115 (2017) 486-497.
[202] A. Abu-Odeh, E. Galvan, T. Kirk, H. Mao, Q. Chen, P. Mason, R. Malak b, R. Arroyave, Efficient exploration of the High Entropy Alloy composition-phase space, Acta Materialia 152 (2018) 41-57.
[203] W.S. Cao, S.L. Chen, F. Zhang, K.S. Wu, Y. Yang, Y.A. Chang, R. Schmid-Fetzerc, W.A. Oates, PANDAT software with PanEngine, PanOptimizer and PanPrecipitation for multi-component phase diagram calculation and materials property simulation, Calphad 33(2) (2009) 328-342.
[204] W.F. Hosford, Mechanical behavior of materials, Cambridge University Press2010.
[205] V. Gerold, H. Haberkorn, On the Critical Resolved Shear Stress of Solid Solutions Containing Coherent Precipitates, physica status solidi (b) 16(2) (1966) 675-684.
[206] B. Jansson, A. Melander, On the critical resolved shear stress from misfitting particles, Scripta Metallurgica 12(6) (1978) 497-498.
[207] A. Argon, Strengthening mechanisms in crystal plasticity, Oxford University Press on Demand2008.
[208] E. Kröner, Berechnung der elastischen Konstanten des Vielkristalls aus den Konstanten des Einkristalls, Z. Phys. 151 (1958) 504-518.
[209] P.A. Ferreirós, P.R. Alonso, G.H. Rubiolo, Coarsening process and precipitation hardening in Fe2AlV-strengthened ferritic Fe76Al12V12 alloy, Materials Science and Engineering: A 684 (2017) 394-405.
[210] M. Wittmann †, I. Baker ‡, P.R. Munroe §, The structure and mechanical properties of Fe2AlMn single crystals, Philosophical Magazine 84(29) (2004) 3169-3194.
[211] S. Suresh, Fatigue of materials, Cambridge university press1998.
[212] Z. Zhang, H. Sheng, Z. Wang, B. Gludovatz, Z. Zhang, E.P. George, Q. Yu, S.X. Mao, R.O. Ritchie, Dislocation mechanisms and 3D twin architectures generate

exceptional strength-ductility-toughness combination in CrCoNi medium-entropy alloy, Nature Communications 8 (2017) 14390.
[213] K. Liu, M. Komarasamy, B. Gwalani, S. Shukla, R.S. Mishra, Fatigue behavior of ultrafine grained triplex Al0.3CoCrFeNi high entropy alloy, Scripta Materialia 158 (2019) 116-120.
[214] K.V.S. Thurston, B. Gludovatz, A. Hohenwarter, G. Laplanche, E.P. George, R.O. Ritchie, Effect of temperature on the fatigue-crack growth behavior of the high-entropy alloy CrMnFeCoNi, Intermetallics 88 (2017) 65-72.
[215] T.-N. Lam, Y.-S. Chou, Y.-J. Chang, T.-R. Sui, A.-C. Yeh, S. Harjo, S.Y. Lee, J. Jain, B.-H. Lai, E.-W. Huang, Comparing Cyclic Tension-Compression Effects on CoCrFeMnNi High-Entropy Alloy and Ni-Based Superalloy, Crystals 9(8) (2019) 420.
[216] J.C. Rao, H.Y. Diao, V. Ocelík, D. Vainchtein, C. Zhang, C. Kuo, Z. Tang, W. Guo, J.D. Poplawsky, Y. Zhou, P.K. Liaw, J.T.M. De Hosson, Secondary phases in AlxCoCrFeNi high-entropy alloys: An in-situ TEM heating study and thermodynamic appraisal, Acta Materialia 131 (2017) 206-220.
[217] X.L. Wang, T.M. Holden, G.Q. Rennich, A.D. Stoica, P.K. Liaw, H. Choo, C.R. Hubbard, VULCAN—The engineering diffractometer at the SNS, Physica B: Condensed Matter 385-386(Part 1) (2006) 673-675.
[218] K. An, H.D. Skorpenske, A.D. Stoica, D. Ma, X.-L. Wang, E. Cakmak, First In Situ Lattice Strains Measurements Under Load at VULCAN, Metallurgical and Materials Transactions A 42(1) (2011) 95-99.
[219] O.H. Basquin, The exponential law of endurance tests, Proc. Astm 10 (1910) 625-630.
[220] L.F. Coffin Jr, A study of the effects of cyclic thermal stresses on a ductile metal, trans. ASME 76 (1954) 931-950.
[221] S.S. Manson, Behavior of materials under conditions of thermal stress, (1954).
[222] S. Fu, H. Bei, Y. Chen, T.K. Liu, D. Yu, K. An, Deformation mechanisms and work-hardening behavior of transformation-induced plasticity high entropy alloys by in -situ neutron diffraction, Materials Research Letters 6(11) (2018) 620-626.
[223] G.M. Stoica, A.D. Stoica, M.K. Miller, D. Ma, Temperature-dependent elastic anisotropy and mesoscale deformation in a nanostructured ferritic alloy, Nature Communications 5 (2014) 5178.
[224] W. Wu, P.K. Liaw, K. An, Unraveling cyclic deformation mechanisms of a rolled magnesium alloy using in situ neutron diffraction, Acta Materialia 85 (2015) 343-353.
[225] L. Ma, L. Wang, Z. Nie, F. Wang, Y. Xue, J. Zhou, T. Cao, Y. Wang, Y. Ren, Reversible deformation-induced martensitic transformation in Al 0.6 CoCrFeNi high-entropy alloy investigated by in situ synchrotron-based high-energy X-ray diffraction, Acta Materialia 128 (2017) 12-21.
[226] T. Ungar, J. Gubicza, G. Ribarik, A. Borbely, Crystallite size distribution and dislocation structure determined by diffraction profile analysis: principles and practical application to cubic and hexagonal crystals, Journal of Applied Crystallography 34(3) (2001) 298-310.

[227] T. Ungar, I. Dragomir, A. Revesz, A. Borbely, The contrast factors of dislocations in cubic crystals: the dislocation model of strain anisotropy in practice, Journal of Applied Crystallography 32(5) (1999) 992-1002.
[228] Q. Xie, J. Liang, A.D. Stoica, R. Li, P. Yang, Z. Zhao, J. Wang, H. Lan, R. Li, K. An, In-situ neutron diffraction study on the tension-compression fatigue behavior of a twinning induced plasticity steel, Scripta Materialia 137 (2017) 83-87.
[229] Q. Xie, Y. Chen, P. Yang, Z. Zhao, Y.D. Wang, K. An, In-situ neutron diffraction investigation on twinning/detwinning activities during tension-compression load reversal in a twinning induced plasticity steel, Scripta Materialia 150 (2018) 168-172.
[230] G. Laplanche, A. Kostka, O.M. Horst, G. Eggeler, E.P. George, Microstructure evolution and critical stress for twinning in the CrMnFeCoNi high-entropy alloy, Acta Materialia 118 (2016) 152-163.
[231] S. Allain, J.P. Chateau, D. Dahmoun, O. Bouaziz, Modeling of mechanical twinning in a high manganese content austenitic steel, Materials Science and Engineering: A 387-389 (2004) 272-276.
[232] C.W. Shao, P. Zhang, R. Liu, Z.J. Zhang, J.C. Pang, Q.Q. Duan, Z.F. Zhang, A remarkable improvement of low-cycle fatigue resistance of high-Mn austenitic TWIP alloys with similar tensile properties: Importance of slip mode, Acta Materialia 118 (2016) 196-212.
[233] M. Valsan, D.H. Sastry, K.B.s. Rao, S.L. Mannan, Effect of strain rate on the high-temperature low-cycle fatigue properties of a nimonic PE-16 superalloy, Metallurgical and Materials Transactions A 25(1) (1994) 159-171.
[234] G.V. Prasad Reddy, R. Sandhya, S. Sankaran, M.D. Mathew, Low Cycle Fatigue Behavior of 316LN Stainless Steel Alloyed with Varying Nitrogen Content. Part I: Cyclic Deformation Behavior, Metallurgical and Materials Transactions A 45(11) (2014) 5044-5056.
[235] A. Saeed-Akbari, J. Imlau, U. Prahl, W. Bleck, Derivation and Variation in Composition-Dependent Stacking Fault Energy Maps Based on Subregular Solution Model in High-Manganese Steels, Metallurgical and Materials Transactions A 40(13) (2009) 3076-3090.
[236] V. Patlan, A. Vinogradov, K. Higashi, K. Kitagawa, Overview of fatigue properties of fine grain 5056 Al-Mg alloy processed by equal-channel angular pressing, Materials Science and Engineering: A 300(1) (2001) 171-182.
[237] H. Xu, D. Ye, L. Mei, A study of the back stress and the friction stress behaviors of Ti-6Al-4V alloy during low cycle fatigue at room temperature, Materials Science and Engineering: A 700 (2017) 530-539.
[238] P. Guo, L. Qian, J. Meng, F. Zhang, L. Li, Low-cycle fatigue behavior of a high manganese austenitic twin-induced plasticity steel, Materials Science and Engineering: A 584 (2013) 133-142.
[239] D. Fournier, A. Pineau, Low cycle fatigue behavior of inconel 718 at 298 K and 823 K, Metallurgical Transactions A 8(7) (1977) 1095-1105.
[240] R.L. McDaniels, L. Chen, R. Steward, P.K. Liaw, R.A. Buchanan, S. White, K. Liaw, D.L. Klarstrom, The strain-controlled fatigue behavior and modeling of

Haynes® HASTELLOY® C-2000® superalloy, Materials Science and Engineering: A 528(12) (2011) 3952-3960.
[241] P. Li, S.X. Li, Z.G. Wang, Z.F. Zhang, Fundamental factors on formation mechanism of dislocation arrangements in cyclically deformed fcc single crystals, Progress in Materials Science 56(3) (2011) 328-377.

VITA

Rui Feng was born in Cangzhou, China. He obtained a Bachelor of Science degree from the Department of Materials Science and Engineering at Yanshan University in 2011. He enrolled in the master program at the Department of Materials Science and Engineering at Shanghai Jiao Tong University, and earned his Master of Science degree in 2014. In May 2014, he joined Dr. Peter K. Liaw's group at The University of Tennessee, Knoxville to pursue his Ph.D. degree in materials science and engineering. He received a Doctor of Philosophy degree in December 2019.